Estimating geocenter motion and changes in the Earth's dynamic oblateness from GRACE and geophysical models

Sun, Yu

DOI
10.4233/uuid:7fe64dde-7fb5-4392-8160-da6f7916dc6b

Publication date
2017

Document Version
Final published version

Citation (APA)
Sun, Y. (2017). *Estimating geocenter motion and changes in the Earth's dynamic oblateness from GRACE and geophysical models*. [Dissertation (TU Delft), Delft University of Technology].
https://doi.org/10.4233/uuid:7fe64dde-7fb5-4392-8160-da6f7916dc6b

Important note
To cite this publication, please use the final published version (if applicable).
Please check the document version above.

Estimating geocenter motion and changes in the Earth's dynamic oblateness from GRACE and geophysical models

Estimating geocenter motion and changes in the Earth's dynamic oblateness from GRACE and geophysical models

Proefschrift

ter verkrijging van de graad van doctor

aan de Technische Universiteit Delft,

op gezag van de Rector Magnificus prof. ir. K.C.A.M. Luyben,

voorzitter van het College voor Promoties,

in het openbaar te verdedigen op dinsdag 24 oktober 2017 om 15:00 uur

door

Yu Sun

Master of Engineering in Geodesy and Survey Engineering,
Shandong University of Science and Technology, Shandong, China
geboren te Dezhou, Shandong, China.

Dit proefschrift is goedgekeurd door de

promotor: Prof. Dr.-Ing Habil R. Klees
copromotor: Dr. R.E.M. Riva

Samenstelling promotiecommissie:

Rector Magnificus,	voorzitter
Prof. Dr.-Ing. Habil R. Klees,	Technische Universiteit Delft
Dr. R.E.M. Riva,	Technische Universiteit Delft
Onafhankelijke leden:	
Dr-Ing. R. Rietbroek	Universität Bonn
Prof. dr. T. van Dam	Université du Luxembourg
Prof. dr. P. Clarke	Newcastle University, UK
Prof. dr. L.L.A. Vermeersen	Technische Universiteit Delft
Overige leden:	
Dr. ir. P.G. Ditmar	Technische Universiteit Delft
Prof. dr. ir. R.F. Hanssen	Technische Universiteit Delft

Keywords: Geocenter motion, J_2, Temporal gravity field variations, Mass transport, Glacial isostatic adjustment, GRACE, Satellite Laser Ranging

ISBN 978-94-6361-016-2

An electronic version of this dissertation is available at
http://repository.tudelft.nl/.

To my family

Contents

Summary

Geocenter motion and changes in the Earth's dynamic oblateness (J_2) are of great importance in many applications. Among others, they are critical indicators of large-scale mass redistributions, which is invaluable to understand ongoing global climate change. The revolutionary Gravity Recovery and Climate Experiment (GRACE) satellite mission enables a constant monitoring of redistributing masses within the Earth's system. However, it still cannot provide reliable time variations in degree-1 coefficients and degree-2 zonal coefficients, which are directly related to geocenter motion and J_2 variations.

Swenson et al. (2008) proposed a methodology to estimate geocenter motion. The resultant solutions have been prevalently used among GRACE users to complement the time-variable gravity field models. Their method relies upon GRACE data as well as supporting geophysical models, including an ocean bottom pressure (OBP) model to provide the oceanic degree-1 coefficients, and a glacial isostatic adjustment (GIA) model to facilitate the removal of solid Earth signals. Swenson's approach has several advantages over other methods, based for example on observations by Satellite Laser Ranging (SLR) or GPS. For instance, it employs evenly distributed satellite-to-satellite observations, which conveniently avoids the so-called network effect, which arises due to sparsely distributed ground stations. However, the obtained annual amplitude of the Z component of the geocenter motion is noticeably smaller (by about 30%) than those from other techniques, suggesting that an investigation is needed for possible improvements. Here, we conducted a series of studies to reach the following objectives. 1) Extend Swenson's method to co-estimate J_2 variations simultaneously; 2) identify the best implementation parameters to estimate both geocenter motion and J_2 variations, by using an end-to-end simulation; 3) exploit error information of input data to estimate geocenter motion and J_2 in a statistically optimal sense.

Swenson's approach was developed to estimate geocenter motion only. In our first study, we have extended it to co-estimated J_2 variations on a monthly basis. The algorithm uses the same input data, namely GRACE gravity solutions and an OBP model. The resulting J_2 variation time series agrees remarkably well with a solution based on SLR data. Seasonal variations of the obtained time series show little sensitivity to the choice of GRACE solutions among CSR RL05, GFZ RL05a, and JPL RL05. For the first time, we find that reducing signal leakage in coastal areas when dealing with GRACE data and accounting for self-attraction and loading (SAL) effects when dealing with water redistribution in the ocean is crucial

in achieving close agreement with the SLR-based solutions in terms of de-trended time-series. The obtained trend estimates, on the other hand, are less accurate due to their dependence on the GIA models, which still carry large uncertainties. Such an approach for estimating geocenter motion and J_2 variations simultaneously is thereafter called the GRACE-OBP approach. It was published in Sun et al. (2016a).

The GRACE-OBP approach produces solutions that are largely dependent on the implementation parameters. The focus of the next study was to optimize the approach. Firstly, an end-to-end numerical simulation study was conducted. Input time-variable gravity field observations were generated by perturbing a synthetic Earth model with realistically simulated errors. We showed that it is important to mitigate high-frequency noise in GRACE solutions, while limiting signal leakage from land to ocean, as well as to account for SAL effects. Secondly, the optimized approach was applied to real GRACE data. We showed that the estimates of annual amplitude in geocenter motion are in line with estimates from other techniques, such as SLR and global GPS inversion. Remarkably, annual amplitudes of C_{10} and C_{11} increased by about 50% and 20%, respectively, compared to estimates based on Swenson et al. (2008). Estimates of J_2 variations are less noisy and by about 15% larger than SLR results in terms of annual amplitude. Linear trend estimates are still dependent on the adopted GIA model, but still comparable to some SLR results.

Although we had improved the choice of implementation parameters for the GRACE-OBP approach, the solutions were not yet statistically optimal since we treated the input data as deterministic. In Sun et al. (2017), we developed a new methodology to estimate monthly variations in geocenter motion and J_2, which was called the combination approach. Unlike the GRACE-OBP approach, the combination approach exploits noise covariance estimates of both input datasets and thus produces stochastically optimal solutions supplied with realistic error information. Numerical simulations showed that the quality of geocenter motion and J_2 variations may be increased by about 30% in terms of RMS error. We also proved that the combination approach reduces to the GRACE-OBP approach if the GRACE data are noise-free and noise in oceanic data is white. Subsequently, we applied this method to real data and evaluated the quality of the resulting geocenter motion and J_2 variations by estimating mass anomaly time-series within carefully selected validation areas, where mass transport is expected to be small. Our validation showed that, compared to selected SLR and Swenson's method the proposed combination approach results in more accurate solutions.

This validation also showed that the annual amplitude of the SLR-based Z-component of geocenter motion is probably overestimated by about 30% (1 mm). The obtained annual amplitude of J_2 variations, on the other hand, is similar to that from the SLR technique. The geocenter motion (degree-1 coefficients) and J_2 (C_{20}) variations from the combination approach are thus so far best suited to support monthly GRACE solutions to produce accurate estimates of surface mass variations.

Samenvatting

Informatie over de beweging van het massamiddelpunt van de aarde en de veranderingen in de dynamische afplatting van de aarde (J2) zijn van belang voor veel toepassingen, waaronder voor het vaststellen van grootschalige massaherverdeling over het aardoppervlak, een onmisbare indicator voor ons begrip van de hedendaagse klimaatverandering. De revolutionaire satellietmissie 'Gravity Recovery and Climate Experiment (GRACE)' maakt het mogelijk om deze grootschalige massaherverdeling continu te meten. Een van de problemen van deze missie is, is dat zij niet in staat is om betrouwbare tijdreeksen van de graad-1- en de zonale graad-2-bewegingen te leveren. Beiden zijn gekoppeld aan bewegingen van het massamiddelpunt van de aarde en veranderingen in de J2.

Swenson et al. (2008) hebben een methode voorgesteld om de bewegingen van het massamiddelpunt van de aarde te schatten. Deze methode is de meestgebruikte methode om deze bewegingen aan de GRACE-metingen toe te voegen . De methode gebruikt zowel GRACE-metingen als ondersteunende geofysische modellen, waaronder een oceaanbodemdrukmodel (OBP) om de graad-1-coefficienten veroorzaakt door oceaandynamica, te schatten en een postglaciaal-opheffingsmodel (GIA) om de vaste-aarde-signalen te verwijderen. De methode van Swenson heeft meerdere voordelen ten opzichte van andere methodes, zoals methodes gebaseerd op satelliet-laser-baanbepaling (SLR) of GPS. De methode gebruikt bijvoorbeeld gelijkmatig verdeelde satelliet-naar-satelliet-observaties, waardoor het zogenaamde netwerkeffect, veroorzaakt door het lage aantal grondstations, wordt voorkomen. De amplitude van de seizoenscyclus in de Z-component is aanmerkelijk smaller (ongeveer 30 procent) dan de amplitude verkregen met behulp van andere methodes, hetgeen suggereert dat een onderzoek naar mogelijke verbeteringen van de Swensonmethode nodig is. We hebben een reeks van studies gedaan om de volgende doelen te bereiken: 1. De methode van Swenson uitbreiden om ook J2-veranderingen tegelijk mee te schatten. 2. Het indentificeren van de beste impementatie-parameters om J2- en massamiddelpunt-veranderingen te schatten met behulp van een einde-tot-eindesimulatie. 3) Het gebruik van fouteninformatie van de invoerdata om J2- en massamiddelpunt-veranderingen in een statistisch optimale manier te schatten.

De methode van Swenson is alleen ontwikkeld om massamiddelpuntbewegingen te schatten. In onze eerste studie hebben we de methode uitgebreid om ook maandgemiddelde J2-variaties mee te schatten. Het algoritme gebruikt dezelfde invoerdata, te weten GRACE-zwaartekrachtsoplossingen en een oceaanbodemdrukmodel. De resulterende tijdreeks van J2-variaties komt goed overeen met de oplos-

sing gebaseerd op SLR-data. De keuze voor een specifieke GRACE-oplossing tussen CSR RL05, GFZ RL05a en JPL RL05 heeft nauwelijks invloed op seizoensvariaties in de verkregen tijdreeks. Voor het eerst hebben we aangetoond dat het terugdrinken van de signaallekkage in kustgebieden en het meenemen van de effecten van zelfgravitatie en aardkostvervorming wanneer de water-herverdeling in de oceaan cruciaal zijn om een goede overeenkomst te verkrijgen tussen de GRACE- en SLR-gebaseerde oplossing van de tijdreeks nadat de lineaire trend verwijderd is. De verkregen schattingen van de lineaire trends zijn echter minder nauwkeurig wegens de afhankelijkheid van GIA-oplossingen, waarin nog grote onzekerheden zitten. Vanaf nu zullen we naar deze benadering voor het gelijktijdig schatten van massamiddelpuntbetwegingen en J2-variaties refereren als de GRACE-OBP-methode. Het werk is gepubliceerd als Sun et al. (2016).

De GRACE-OBP-methode genereert oplossingen die voor een groot deel afhankelijk zijn van de implementatieparameters. Het doel van de tweede studie is om deze methode te optimaliseren. Als eerste is een numerieke eind-tot-eind-simulatie uitgevoerd. Als invoerdata werden tijdafhankelijke zwaartekrachtvelden gegenereerd door bovenop de uitvoer van een synthetisch aardmodel realistische verstoringen aan te brengen. We laten het belang zien van het verminderen van de hoogfrequente ruis in GRACE-oplossingen, het beperken van de signaal-lekkage in kustgebieden, en het meenemen van zelfgravitatie- en aardvervormingseffecten. Vervolgens is de optimale impementatie-aanpak toegepast op echte GRACE-data. We tonen aan dat schatingen van de amplitude van de seizoenscyclus in de massamiddelpuntbeweging consistent zijn schattingen met behulp van andere technieken, waaroner SLR en een globale inversie van GPS-observaties. Opmerkelijk was de toename van 50 procent in de amplitude van de seizoenscyclus in C10, en 20 procent voor de seizoensamplitude in C20, vergeleken met de oplossing van Swenson et al. (2008). Schattingen van de J2-parameter hebben een lager ruisniveau en hebben een amplitude in de seizoenscyclus die 15 procent hoger ligt dan de SLR-oplossing. Schattingen van de lineaire trend zijn nog steeds afhankelijk van het gebruikte GIA-model, maar zijn vergelijkbaar met de SLR-resultaten.

Hoewel we de keuze van implementatieparameters hebben verbeterd voor de GRACE-OBP-methode, zijn de oplossingen nog steeds niet statistisch optimaal, omdat we de invoerdata steeds als deterministisch hebben beschouwd. In Sun et al. (2017) hebben we een nieuwe methode, die we de combinatie-benadering noemen, ontwikkeld om maandelijkse variaties in J2 en het massamiddelpunt te schatten. In tegenstelling tot de GRACE-OBP-methode gebruikt de combinatiemethode de ruis-covariantieschattingen van beide invoerdatasets, waardoor de statistisch optimale oplossingen met realistische foutschattingen worden geproduceerd. Numerieke simulaties laten zien dat het kwadratisch gemiddelde van de J2-variatie-oplossing afneemt met 30 procent. We laten ook zien dat de combinatiemethode convergeert naar de GRACE-OBP-methode wanneer we GRACE-foutschattingen niet meenemen en we aannemen dat de ruis in de oceaanmodeldata een wit frequentiespectrum heeft. Vervolgens hebben we de methode op echte data toegepast en de kwaliteit van de resulterende J2-variatieschatting door massa-anomalietijdreeksen in zorg-

vuldig geselecteerde controlegebieden waar het verwachte massatransport klein is te schatten. Deze validatie laat zien dat, vergeleken met de SLR- en Swensonmethode, de combinatiemethode de meest nauwkeurige oplossingen produceert.

De validatie laat ook zien dat dat de amplitude van de seizoenscyclus van het SLR-gebaseerde z-component waarschijnlijk met circa 30 procent (1 mm) wordt overschat. De verkregen amplitude van de seizoenscyclus van J2 is wel vergelijkbaar met de SLR-waarde. De massamiddelpunts- en J2-variaties van de combinatiemethode zijn daarom voorlopig de beste manier om de GRACE-data te corrigeren met als doel nauwkeurige schattingen van oppervlaktemassatransport te schatten.

1

Introduction

1

1.1. Background and Motivations

The Earth system can be divided into two parts: 1) the solid Earth, including the fluid core, the convecting mantle, and the crustal outer layer and 2) its fluid envelope, which consists of atmosphere, oceans, and continental water/ice/snow. All components in both parts are subject to continuous motion at different time scales and interact with each other, causing mass redistributions within the Earth system. As a consequence, the Earth's gravitational field changes accordingly.

The Earth's gravitational field is often represented in the spherical harmonic domain by a set of dimensionless (Stokes) coefficients. The major focus of this thesis are the degree-1 coefficients (C_{10}, C_{11}, S_{11}) and the degree-2 zonal (C_{20}) coefficient. These coefficients are among those with a specific physical meanings. The degree-1 coefficients reflect the position of the geocenter, and C_{20} represents the so-called Earth's dynamic oblateness. We will introduce both terms in the following sections.

1.1.1. Geocenter Motion

The term geocenter is used to denote the center of the Earth's system, which may have different definitions. The three commonly used ones are the center of mass of the solid Earth (CE), the center of mass of the whole Earth system (CM) and the center of figure of the solid Earth surface (CF). In this thesis, we adopt the CM as the geocenter following the recommendation of the International Earth Rotation and Reference System Service (IERS) (e.g. Ray, 1999; Petit and Luzum, 2010). The CM represents the orbiting center of all satellites. As a result, its position can be realized by observations of the dynamics of satellites orbiting the Earth (Ray, 1999). The CE is in constant motion with respect to the CM. Among others, the rapid fluxes of the atmosphere, oceans and continental water modify the mass distributions at the solid Earth surface, and the entire Earth, hence CE, moves with respect to CM to compensate this mass redistribution. The absolute position of the CE is difficult to be realized due to the lack of an accurate density model of the solid Earth. The CF, on the other hand, can be realized on the basis of the position of geodetic stations at the solid Earth surface. Relative motions are also detectable between the CF and the CM. The motion of CM with respect to CF is defined as the geocenter motion (Ray, 1999; Blewitt et al., 2001; Wu et al., 2012).

Same as the motion of CE with respect to CM, present-day geocenter motion is also mainly driven by tides, seasonal and inter-annual surface mass redistribution and long-term mass transport processes taking place above and below the solid Earth surface. At semi-diurnal and diurnal time-scales, ocean tides are responsible for few-millimeter variations in the geocenter (Watkins and Eanes, 1997). Ocean tides with long periods contribute with less than 0.5 mm (Crétaux et al., 2002). Atmosphere tides may lead to a geocenter motion at the level of about 1 mm (Ray and Ponte, 2003). At seasonal and inter-annual time-scales, geocenter motion is

primarily due to solar-powered mass transport in the fluid surface layer. The annual amplitude of such a motion can reach a few millimeters. When considering secular time-scales, the signal is mainly driven by Glacial Isostatic Adjustment (GIA), which is related to the melting of the large ice sheets at the end of the Pleistocene (last glacial period) (e.g. Lambeck et al., 2014; Peltier et al., 2015; Milne et al., 2001; Riva et al., 2009; Klemann and Martinec, 2011; Gunter et al., 2014).

Estimating geocenter motion is of great importance in both geokinematics and Earth gravity perspectives.

Geokinematics studies motions of the Earth's surface which is usually measured in terrestrial reference frames (TRFs). An accurately estimated geocenter motion is fundamental to realize a TRF. This is due to the fact that the origin of a TRF (including the International TRF, ITRF (Altamimi et al., 2016)) is defined at the long-term mean CM. However, its realization is a quasi-instantaneous CM, which follows CF on seasonal and short timescales (Dong et al., 2003; Wu et al., 2012). Therefore, geodetic systems referenced to he ITRF would need geocenter motion time-series as a correction. Ignoring geocenter motion introduces an error, which is non-negligible according to modern geodesy requirements. For example, the accuracy and stability of the ITRF are now aiming to be at 1 mm and 0.1 mm yr^{-1} level (e.g. Altamimi et al., 2011; Gross et al., 2009). The current state of the art needs a significant improvement (factor of 5) to reach this goal (Wu et al., 2011).

Geocenter motion is also critical for Earth's gravity field determination, such as the nominal products of several satellite gravity missions, including the Gravity Recovery and Climate Experiment (GRACE) mission (Tapley et al., 2004). GRACE is a joint project of the National Aeronautics and Space Administration (NASA) in the United States and its counterpart in Germany, the Deutsche Forschungsanstalt für Luft und Raumfahrt (DLR). GRACE employs twin satellites traveling along the same polar orbit following each other with a separation of about 220 km. The GRACE satellites collect inter-satellite range-rate measurements, which are so sensitive that temporal variations in Earth's gravity field can be detected. On this basis, data analysis centers produce time-variable gravity field solutions with unprecedented accuracy (e.g. Bettadpur, 2012; Dahle et al., 2013; Liu et al., 2010). However, the degree-1 coefficients are absent there because the GRACE satellite-to-satellite measurements are inherently insensitive to geocenter motion. Therefore, independent estimates of geocenter motion have to be used to complement the GRACE-based Earth's gravity field models in order to correctly estimate surface mass changes. An improper estimate of geocenter motion severely affects mass redistribution estimates. For instance, 1-mm geocenter motion error in the X, Y and Z direction will lead to a bias in global ocean mass change of -173, -95 and -190 gigatons (i.e., cubic kilometers of water) respectively.

Despite numerous efforts in estimating degree-1 coefficients, they still carry large uncertainties. This is the motivation to improve the existing approaches and develop new methodologies to estimate geocenter motion more accurately.

1

1.1.2. Earth's Dynamic Oblateness

The Earth's dynamic oblateness, also known as J_2, is a function of the difference between the equatorial and polar radii of the ellipsoid approximating the Earth's figure. Variations in J_2 are dominated by several signatures, including a negative secular trend, seasonal, inter-annual, decadal variations and Earth body tides (at up to 18.6 year timescales). The secular decrease of the J_2 indicates that the Earth is becoming less oblate, which is mainly due to a combination of GIA effect (Yoder et al., 1983) and present-day rapid polar ice mass loss (Nerem and Wahr, 2011). The seasonal variations reflect mass redistribution between tropical and extra-tropical regions (Gutierrez and Wilson, 1987). Inter-annual variations are closely related to El Niño-Southern Oscillation (ENSO) (Cheng and Tapley, 2004). Decadal variations are now demonstrated to be mainly driven by Greenland and Antarctic ice mass variations during the last four decades (Nerem and Wahr, 2011; Seo et al., 2015). The inter-annual and decadal variations are so strong that they can temporally reverse the secular trend (Cox and Chao, 2002; Dickey et al., 2002; Cheng and Tapley, 2004). Apart from the linear trend, Cheng et al. (2013a) recently have found an deceleration in the J_2 variations, which can be attributed to the accelerated ice mass loss of glaciers and ice-sheets.

Although the GRACE mission is able to determine variations in J_2, those estimates are corrupted with unexpectedly large aliases, which are likely caused by a thermal-related systematic error in the accelerometer data (Cheng and Ries, 2017). As a result, GRACE users still rely on traditional estimates of J_2 variations based on SLR data. However, due to the high-altitude of SLR satellites, they are not sensitive to gravity changes at the middle to high-degree part of the spectrum. As a result, J_2 is not well-separated from other zonal terms (e.g. Yoder et al., 1983; Cheng et al., 1989). Thus, replacing estimates of J_2 variations in GRACE-based solutions with independent estimates is not proper unless the correlations between coefficients are considered.

Similar to the case of estimating geocenter motion, such a situation stimulates the needs for an accurate estimation of J_2 variations that takes GRACE data into account. GRACE observes other coefficients up to relatively high degree and can thus reduce the aliases into the degree-1 and J_2 terms. Also, a GRACE-based approach would allow to derive error correlations between degree-1, J_2 and other coefficients. Together with the stochastic description of errors in the produced degree-1 and J_2 (C_{20}) coefficients they can be used to improve the stochastic description of errors in GRACE gravity field models.

1.2. Research Objectives

We focus on the changes in the degree-1 and C_{20} of the Earth's gravitational field. In order to do so, we choose a method proposed by Swenson et al. (2008) as our

starting point. This methodology estimates geocenter motion from a combination of GRACE data and geophysical model output. Though the obtained solution is prevalently used and built upon a solid theory, discrepancies exist when compared with those from other techniques. In this thesis, we aim to improve and develop further this promising methodology, which is originally dedicated to geocenter estimation, and obtain more accurate solutions for both degree-1 and C_{20} coefficients. The objectives of this thesis are as follows:

(i) Extend the methodology by Swenson et al. (2008) to co-estimate changes in the Earth's dynamic oblateness on a monthly basis. Use GRACE data and modeled OBP estimates and GIA models as input data. Validate the results against Satellite Laser Ranging (SLR) solutions.

(ii) Optimize the implementation parameters of the methodology developed in (i) through an end-to-end simulation. Refine estimates of annual variations and trends in both geocenter motion and changes in Earth's dynamic oblateness time-series.

(iii) Improve further the methodology used in (i) and (ii) by exploiting error information of the input datasets. Develop a statistically optimal methodology to estimate geocenter motion and changes in the Earth's dynamic oblateness, which also produces realistic uncertainties. Test the method with synthetic data and then apply it to real data.

1.3. Outline

The rest of the dissertation is organized as follows:

Chapter 2 presents a brief overview of current methodologies for determining degree-1 and C_{20} coefficients.

Chapter 3 presents an improved methodology for the determination of the degree-1 and C_{20} coefficients simultaneously from a combination of GRACE data and modeled ocean bottom pressures. The content of this chapter has been published in (Sun et al., 2016a).

Chapter 4 is about improving the methodology described in Chapter 3, by optimizing the choice of implementation parameters through a simulation. In the second part of the chapter, degree-1 and C_{20} coefficients are estimated based on real data using the selected parameter settings and compared with solutions from other techniques. The content of this chapter has been published as (Sun et al., 2016b).

Chapter 5 develops a new method to estimate the degree-1 and C_{20} coefficients as well as their uncertainties using a statistically optimal combination of GRACE data and ocean bottom pressure model. The proposed methodology is also applied

to real data processing. The resulting solutions based on real data are then validated. This work has been published as (Sun et al., 2017).

Chapter 6, comprises conclusions and recommendations for future research.

2

Literature Overview: Existing Methodologies for the Estimation of Geocenter Motion and Variations in Dynamic Oblateness

This chapter describes the methods for estimating geocenter motion and changes in the Earth's dynamic oblateness.

2

2.1. Geocenter Motion

The Cartesian components (ΔX, ΔY, ΔZ) of geocenter motion due to surface mass redistribution correspond one-to-one to the time variations of the three degree-1 Stokes coefficients (ΔC_{11}, ΔS_{11} and ΔC_{10}) of the Earth's gravitational field through (e.g. Farrell, 1972; Blewitt, 2003)

$$\begin{Bmatrix} \Delta X \\ \Delta Y \\ \Delta Z \end{Bmatrix} = \frac{a\sqrt{3}}{1+k_1} \begin{Bmatrix} \Delta C_{11} \\ \Delta S_{11} \\ \Delta C_{10} \end{Bmatrix}, \tag{2.1}$$

where a is the average radius of the Earth; k_1 is the elastic degree-1 load Love number, which is different in different reference frames and for different parameterization of the Earth's mechanical properties. Note that we are not using primed symbols for Love numbers, but they all should be understood as load Love numbers. In view of Eq. (2.1), geocenter motion and time variations of the degree-1 coefficients are used interchangeably throughout the whole thesis.

Here, we give an introduction to the commonly used methodologies to determine geocenter motion. A reader needs to bear in mind that these methods may be named differently in the literature.

There are two main classes of methods to obtain estimates of geocenter motion. The first class directly observes the distance between satellites, which are naturally orbiting around the CM, and the ground stations anchored to the solid Earth surface. Thus, such a method is called the direct method. The second class determines the geocenter motion by the estimation of gravitational degree-1 coefficients. Such a method is often referred to as the inversion approach.

2.1.1. Direct Methods

Observing the dynamics of the satellites orbiting around the CM with a ground tracking system fixed to the CF provides a natural way of monitoring geocenter motion. Geodetic techniques, such as Satellite Laser Ranging (SLR), Global Navigation Satellite System (GNSS) and the Doppler Orbiography and Radiopositioning Integrated by Satellite (DORIS), are options to implement this method.

Before introducing individual techniques, we discuss general strengths and limitations concerning all the direct methods. The theory of the direct method is quite straightforward. An obvious advantage of this method is that it determines the

absolute position of CM with respect to the solid Earth's surface. However, when determining the motion of CM relative to CF, a common problem affects all the three aforementioned geodetic techniques. That is, the ground tracking networks are not evenly distributed over the Earth, which makes it difficult to determine an actual CF or an origin that is stationary relatively to the CF. Instead, these tracking stations merely realize the center of a particular network (CN). Relative movements between the CN and the CF are known as the network effect (Wu et al., 2002; Collilieux et al., 2009). Such an effect prevents a direct comparison of a solution from the direct method and that from the inversion approach. Furthermore, since the network effect affects the direct methods differently depending on the exploited network, a comparison between different direct methods is not straightforward either (Wu et al., 2012).

SLR is the traditionally used direct techniques to determine geocenter motion. SLR satellites are sphere-shaped passive targets with low area-to-mass ratio orbiting at high altitudes. All these features help to minimize the atmospheric drag. Therefore, the dynamic orbits of the SLR satellites can be accurately modeled, which makes SLR the most reliable and accurate geodetic technique for the purpose of realizing the position of the geocenter. This is confirmed by the fact that the origin of the ITRF is realized solely by SLR data (Altamimi et al., 2011, 2016). In spite of this, an accurate determination of the geocenter motion is severely degraded by the network effect. The SLR tracking stations represent a very sparse network concentrated at mid-latitudes with a concentration on the northern hemisphere (Fig. 2.1). Such a network is especially vulnerable to the network effect because of two reasons. First, not all stations are permanently available, which leads to a changeable (time-varying) configuration of the network. Second, displacements of individual stations due to solid Earth deformation induced by surface loading may substantially alter the position of the CN for such a small network. According to Collilieux et al. (2009), the network effect can account for about one-third of the SLR-observed motion between CM and CN. Recently, Wu et al. (2015) connected SLR stations with those used by other techniques through local tie measurements and co-motion constraints in an effort to extend the SLR network to contain 82 stations. The resultant larger SLR network helps to reduce the impact of the network effect significantly. Currently, the uncertainty of the estimated annual amplitude of the geocenter motion time-series from SLR data is about 10 % of the signal itself (personal communication with John Ries), that is 0.2 mm to 0.6 mm.

The strategy of estimating the geocenter motion using GNSS data is slightly different. At a particular epoch, the coordinates of the ground tracking stations are estimated in the CM reference frame. The resulting set of coordinates forms a so-called "fiducial-free" network because the coordinates are only loosely constrained with large apriori uncertainties (1 meter, for example). Then a Helmert seven-parameter (three translation, three rotations and one scale parameter) transformation is performed to align this "free" network to a known TRF centered at the long-term mean CM, which is assumed to be stationary with respect to the CF (e.g. Blewitt et al., 1992; Blewitt, 2003; Dong et al., 2003). The three translation parameters esti-

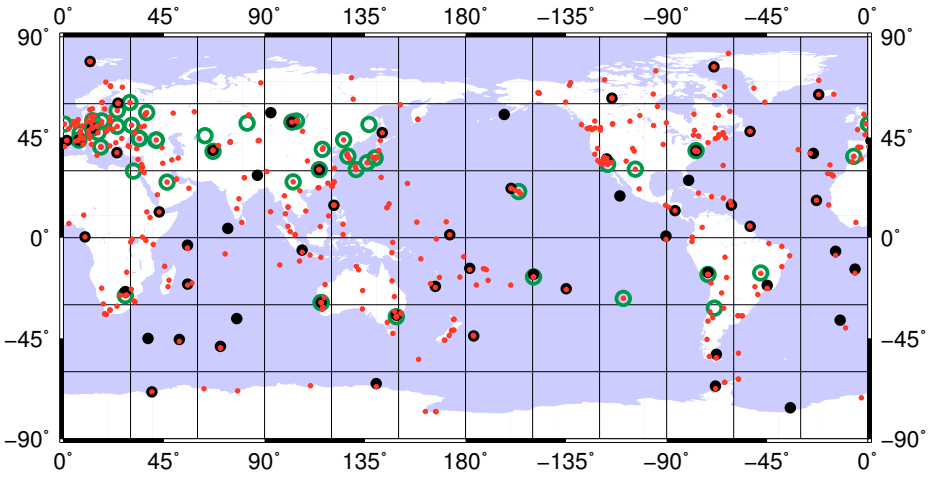

Figure 2.1: The current network for SLR (green open circles), GNSS (red dots) and DORIS (black solid circles) techniques. The location information of stations for the three techniques can be found on the following sites: https://ilrs.cddis.eosdis.nasa.gov/network/stations/index.html, http://www.igs.org/network, https://ids-doris.org/doris-system/tracking-network/site-logs.html

mated represent the motion of CM with respect to CN. Such a method is called the "network-shift" approach (Dong et al., 2003). However, the scale parameter is not recommended when estimating Helmert transformations for this case. For example, Tregoning and van Dam (2005) demonstrated with synthetic data that estimating a scale parameter degrades the accuracy of site coordinates and geocenter motion estimates when surface loads are present and unaccounted for. This is because the scale parameter could absorb some of the loading deformation. The scale parameter is included when estimating Helmert transformations to investigate systematic differences in the definition of scale between different techniques (e.g. SLR, GNSS). It is not needed when only one technique is considered (Lavallée et al., 2006).

The GNSS network is less affected by the network effect than the SLR network due to a large number of continuously operating tracking stations (Fig. 2.1). However, in spite of continuous efforts in GNSS data analysis, geocenter motion time-series as accurate as those based on SLR observations have not been produced yet. Two studies have even reported that the GNSS network shift approach is insensitive to geocenter motion. Based on the methods of perturbation theory and celestial mechanics, Meindl et al. (2013) found large correlation between the solar radiation pressure parameters and the Z-component of the geocenter motion, which is responsible for the large periodic artifacts with an amplitude of about 20 cm in their geocenter time-series. Rebischung et al. (2014), investigated the quasi-linear dependencies (collinearity) between different parameters in a least squares regression. Based on simulated observations, the authors found a very high collinearity

of two categories of parameters which are estimated simultaneously: epoch-wise clock offsets and tropospheric parameters. These parameters are therefore not reliably inferred from observations. Consequently, geocenter motion estimates are also not accurate. The derived geocenter time-series are also contaminated by spurious signals with an amplitude reaching several millimeters and with a period of the GPS draconitic year (351.2 days), which is the interval required for the satellite constellation to repeat its inertial orientation to the Sun (Ray et al., 2008; Griffiths and Ray, 2013). Consequently, the GNSS data has not yet been able to provide accurate geocenter estimates using the direct method (Rebischung et al., 2014).

DORIS can also provide geocenter motion estimates using the network shift approach (Bouillé et al., 2000). Since it has the most homogeneously distributed tracking network (Fig. 2.1), the resulting geocenter motion should be the least affected by the network effect. However, the DORIS-based geocenter motion solutions are believed to be less accurate compared to those based on SLR data (e.g. Altamimi et al., 2005; Altamimi and Collilieux, 2010; Altamimi et al., 2011; Gobinddass et al., 2009a). For example, the reported annual amplitudes in Bouillé et al. (2000) are 2.4 ± 1.4, 2.1 ± 1.3 and 2.1 ± 1.1 mm in X-, Y- and Z-component, respectively. Uncertainties of all three geocenter motion components are about 50 % of the amplitude. Later, larger annual amplitudes in X- and Y-components (4 to 7 mm) were found in typical DORIS estimates (Altamimi et al., 2005). The Z-component, is even noisier. Also, an offset of 65 cm in the geocenter position was detected and identified to be related to a particular DORIS satellite (SPOT-4) in 1998 (Willis et al., 2005, 2006). Besides this problem, the Z-component is still affected by large seasonal aliases with an amplitude of 34 mm (Meisel et al., 2005), which is one order of magnitude larger than the expected physical signal. One important part of the large systematic errors has been attributed to miss-modeling of solar radiation pressure Gobinddass et al. (2009b). By reprocessing the DORIS data and scaling the solar radiation models with an empirically determined coefficient for each of the DORIS satellites, Gobinddass et al. (2009a) managed to improve the measurement noise of the Z-component of geocenter motion from 47.5 to 30.4 mm for the RMS and from 35 to 6 mm for the amplitude of the annual signal, which is still worse compared to SLR results.

2.1.2. Inversion Methods

The inversion method involves the determination of the degree-1 gravitational coefficients or the degree-1 mass coefficients, where mass coefficients are the spherical harmonic coefficients used to describing time variations in surface mass $\sigma(\theta,\phi)$

$$\sigma(\theta,\phi) = \sum_{l=1}^{\infty} \sum_{m=0}^{l} \bar{P}_{lm}(\cos\theta)\{\Delta C_{lm} \cos m\phi + \Delta S_{lm} \sin m\phi\}, \tag{2.2}$$

where $\bar{P}_{lm}$ represent normalized associated Legendre functions; θ and ϕ are the

colatitude and longitude in spherical coordinates, respectively; ΔC_{lm} and ΔS_{lm} are time-variations in mass coefficients of degree l and order m. We will drop Δ for clarity hereafter.

According to Wahr et al. (1998), mass coefficients and gravitational coefficients can be easily transformed from one to the other assuming that the changes in the gravitational field can be solely attributed to surface mass redistribution:

$$\begin{Bmatrix} C_{lm} \\ S_{lm} \end{Bmatrix} = \frac{a\rho_{earth}(2l+1)}{3(1+k_l)} \begin{Bmatrix} C^g_{lm} \\ S^g_{lm} \end{Bmatrix}, \tag{2.3}$$

where C^g_{lm} and S^g_{lm} denote the time variations of gravitational coefficients; k_l denotes the elastic load Love numbers and ρ_{earth} represents the average Earth density.

Under the assumption that the Earth is an elastic body, global mass redistribution can be determined by analyzing the resultant solid Earth deformation using load Love number theory (Farrell, 1972; Blewitt, 2003). Since surface mass redistribution is the primary driving force of geocenter motion, a relationship between geocenter motion and solid Earth deformation can be built. For the first time, Blewitt et al. (2001) estimated geocenter motion (degree-1 coefficients) based on the accompanied solid Earth deformation detected by 66 globally distributed GPS tracking stations. The solid Earth deformation contains contributions of higher degree coefficients, which in theory can be ignored based on the orthogonality of the surface spherical harmonic functions. However, this is not true if those coefficients are derived from a set of non-homogeneously distributed data points. As a consequence, higher degree harmonics will alias into the degree-1 estimates (Wu et al., 2002). As an improvement, Wu et al. (2003) exploited more GPS tracking stations (200 sites). The derived solid Earth deformation was then inverted into spherical harmonic coefficients up to degree 6 in order to reduce the higher-degree aliasing. Such a procedure has been further developed by employing GRACE data to co-estimate higher-degree signals (Kusche and Schrama, 2005). After that, ocean bottom pressure (OBP) measurements based on the Estimating the Circulation and Climate of the Ocean (ECCO) model have been incorporated into a GPS/OBP/GRACE inversion (e.g. Wu et al., 2003, 2006). In addition, spherical harmonic coefficients up to degree 50 were co-estimated. The OBP measurements helped to close the data gap in the open ocean and dramatically improved the results (Wu et al., 2006; Jansen et al., 2009). Finally, (Rietbroek et al., 2009, 2012b) implemented a joint inversion approach, which combined the GPS, GRACE and OBP data in a statistically optimal framework by exploiting error information of each input dataset.

Inversion approaches produce smaller and more regular geocenter motion estimates than direct approaches (Wu et al., 2012), but are not necessarily superior to the direct solutions based on SLR data. Firstly, the modeled OBP estimates do not contain the total ocean mass variations (e.g., the water exchange between ocean

and land is not included). Usually, they also do not consider the time-variable self-attraction and loading effects, which represent the passive response of ocean water due to mass redistribution. Secondly, all the inversion approaches so far are based on an elastic Earth model. Therefore, deformations due to mass redistribution in the interior of the solid Earth need to be removed before the inversion procedure (Wu et al., 2003). Since the solid Earth contribution is primarily due to the GIA, which shows nearly constant surface deformation rates, it is sufficient to remove the linear trends from the GPS time-series before inverting them into spherical harmonic coefficients. Obviously, this procedure also removes the contribution of the present-day mass transport (PDMT) to the linear trend. In an attempt to estimate the trend in geocenter motion time-series, Wu et al. (2010) employed site velocities measured by geodetic techniques (SLR, GNSS, etc), trends in gravity field variations measured by GRACE and PDMT derived from ECCO OBP model in a global inversion for estimating GIA- and PDMT-induced trends simultaneously. In order to solve the problem of rank deficiency, the GIA gravitational potential coefficients (of degree higher than 8) were approximately related to the corresponding vertical displacement coefficients (Wahr et al., 2000). However, the results were not satisfactory. For instance, the resulting GIA estimates predicted a large negative trend over Greenland, which contradicts all existing GIA models (Sutterley et al., 2014).

Unlike the GNSS network-shift approach, the GNSS inversion approach first places the fiducial-free network in the CN reference frame by estimating and removing a seven-parameter Helmert transformation. Then the degree-1 and higher-degree coefficients are estimated from the residuals, which contain the deformation of the network due to the geocenter motion. Lavallée et al. (2006) proposed to model the translational and deformational signatures due to geocenter motion simultaneously through the so-called unified approach. Theoretically, it is a better way of estimating geocenter motion, but the resulting solutions did not reach a good agreement with each other (Rülke et al., 2008; Fritsche et al., 2010). This is probably due to different processing procedures applied on the GNSS data. Recently, Wu et al. (2017) updated the unified approach by using an extended SLR network of 82 sites (Wu et al., 2015). Surface mass coefficients up to degree 43 were estimated. GRACE data were included to better isolate the degree-1 contributions. However, the resultant annual amplitude of the X-component (C_{11} coefficients) was only 1.3 mm, which is about 1 mm smaller than the estimates based on other techniques (e.g. Wu et al., 2006, 2015). The results are thus considered not satisfactory.

Rietbroek et al. (2012a, 2016) developed a forward modeling approach in an attempt to solve the sea level budget, that also produces geocenter motion time-series. In this approach, the contributions of all sources (e.g., glaciers and ice-sheets) are represented by pre-defined spatial patterns (also called fingerprints) multiplied by time-varying coefficients to be estimated. The linear combination of these patterns is equated with the global mass redistribution observed from GRACE and satellite altimetry. Scaling factors are then estimated through least-squares regression. The degree-1 coefficients can then be obtained by a summation of the properly scaled degree-1 components of all the re-defined patterns. Such a method results in a

realistic degree-1 estimates but is somewhat dependent on the selection of the fingerprints. Also, the fingerprints of surface mass transport in Antarctica appears to be contaminated by the local GIA. The GIA signals are co-estimated during the inversion, but uncertainties are still introduced due to the use of a priori GIA model. The obtained seasonal variations, on the other hand, seem reasonable, as they are comparable to those based on the global GPS inversion.

Mass coefficients can also be obtained from GRACE satellite mission, which monitors the surface mass redistribution by sensing changes in the Earth's gravity field. However, the obtained mass redistribution includes no contribution from the degree-1 Stokes coefficients, as they are equal to zero in the CM reference frame by definition. Swenson et al. (2008) proposed to solve this problem by using an OBP model. This approach is at the basis of the work presented in this thesis and will be introduced in a separate section.

The degree-1 mass coefficients may also be extracted from the sum of geophysical signals in atmosphere, oceans, land hydrology, the cryosphere, etc. computed with appropriate models (e.g. Dong et al., 1997; Chen et al., 1999; Dong et al., 2014). Such estimates are useful to understand the geophysical mechanism/causes of the geocenter motion phenomenon, but less accurate than the estimates based on real data due to unknown, and often large, uncertainties in geophysical models (Wu et al., 2012). However, it is likely a promising method because of the continuously increasing quality of those models.

2.1.3. The approach by Swenson et al. (2008)

Swenson's approach is built on the fact that oceanic mass variations can be inferred from a full spectrum (including degree-1 contributions) of GRACE gravity field solutions. Once oceanic variations are known, the three unknown degree-1 coefficients can be estimated. The oceanic variations are obtained by combing an OBP model and the total ocean mass variations derived from GRACE.

In this approach, surface mass variations are separated globally into two parts: oceanic and continental ones. This can be done by using an ocean function $\vartheta(\theta,\phi)$, which equals 1 over oceans and 0 over land. Equation (2.2) can be written as

$$\begin{aligned}\sigma(\theta,\phi) &= \sigma(\theta,\phi)\vartheta(\theta,\phi) + \sigma(\theta,\phi)(1-\vartheta(\theta,\phi)) \\ &= \sigma^{ocean}(\theta,\phi) + \sigma^{land}(\theta,\phi) \\ &= \sum_{l=1}^{\infty}\sum_{l=0}^{l}\{(C_{lm}^{ocean}+C_{lm}^{land})\cos m\phi + (S_{lm}^{ocean}+S_{lm}^{land})\sin m\phi\},\end{aligned} \tag{2.4}$$

where C_{lm}^{land} and S_{lm}^{land} are the continental mass coefficients and C_{lm}^{ocean} and S_{lm}^{ocean}

are the oceanic mass coefficients. Therefore, once oceanic mass variations are known, one can derive oceanic mass coefficients using

$$C_{lm}^{ocean} = \frac{1}{4\pi}\int \bar{P}_{lm}(\cos\theta)\cos m\phi\,\vartheta(\theta,\phi)\sigma(\theta,\phi)d\Omega, \tag{2.5}$$

where $d\Omega = \sin\theta d\theta d\phi$ is an element of solid angle and the integral is defined over the entire globe. In practice, the global integral is solved using discretized integral over a 1° by 1° grid. Substituting equation (2.2) into equation (2.5), C_{10}^{ocean} can be obtained by

$$\begin{aligned} C_{10}^{ocean} = &\frac{1}{4\pi}\int \bar{P}_{10}(\cos\theta)\vartheta(\theta,\phi)\bar{P}_{10}(\cos\theta)C_{10}d\Omega + \\ &\frac{1}{4\pi}\int \bar{P}_{10}(\cos\theta)\vartheta(\theta,\phi)\sum_{l=1}^{\infty}\sum_{m=0}^{l}\bar{P}_{lm}(\cos\theta)\{C_{lm}\cos m\phi + S_{lm}\sin m\phi\}d\Omega, \end{aligned} \tag{2.6}$$

where the summations exclude the degree 1 order 0 terms. Similarly, C_{11}^{ocean} and S_{11}^{oean} can also be calculated. Following this idea, a matrix equation was then derived:

$$\begin{bmatrix} I_{10C}^{10C} & I_{11C}^{10C} & I_{11S}^{10C} \\ I_{10C}^{11C} & I_{11C}^{11C} & I_{11S}^{11C} \\ I_{10C}^{11S} & I_{11C}^{11S} & I_{11S}^{11S} \end{bmatrix} \begin{bmatrix} C_{10} \\ C_{11} \\ S_{11} \end{bmatrix} = \begin{bmatrix} C_{10}^{ocean} \\ C_{11}^{ocean} \\ S_{11}^{ocean} \end{bmatrix} - \begin{bmatrix} G_{10C} \\ G_{11C} \\ G_{11S} \end{bmatrix}, \tag{2.7}$$

where the following notations have been used:

$$\begin{aligned} I_{10C}^{11S} = &\frac{1}{4\pi}\int \bar{P}_{11}(\cos\theta)\sin(1\times\phi)\vartheta(\theta,\phi)\bar{P}_{10}(\cos\theta)\cos(0\times\phi))d\Omega \\ &\text{(similar for the other elements of matrix } I\text{)}, \end{aligned} \tag{2.8}$$

and

$$\begin{aligned} G_{10C} = &\frac{1}{4\pi}\int \bar{P}_{10}(\cos\theta)\cos(0\times\phi)\vartheta(\theta,\phi) \\ &\sum_{l=2}^{\infty}\sum_{m=0}^{l}\bar{P}_{lm}(\cos\theta)\{C_{lm}\cos m\phi + S_{lm}\sin m\phi\}d\Omega \\ &\text{(similar for the other elements of vector } G\text{)}. \end{aligned} \tag{2.9}$$

The G vector is based on GRACE data and the three oceanic degree-1 coefficients are taken from the adopted OBP model. Since an OBP model conserves the ocean mass, the mass exchange between ocean and land, which causes the eustatic sea level varies with about 10 mm annual amplitude, is not taken into account. In Swenson's approach, the total ocean mass variations are estimated by integrating GRACE-based mass anomalies over oceans and added to the OBP-predicted oceanic mass anomalies in the form of a uniform water layer.

Swenson's approach is based on solid theory. However, the annual signals in C_{10} coefficients were not comparable with most of the solutions based on other techniques (Wu et al., 2012). For example, the annual amplitude of the C_{10} was about 30 % (1 mm) smaller and the annual phase was offset by more than a month.

2.2. Changes in the Earth dynamic oblateness

The second-degree zonal coefficient, C_{20}, is related to the Earth's dynamic oblateness, which is better known as J_2 ($J_2 = -\sqrt{5}C_{20}$). Therefore, C_{20} and J_2 will be used interchangeably. J_2 is a function of the Earth's mean principal moments of inertia, which in turn are related to the equatorial and polar radii of a best-fitting ellipsoid of revolution via Clairaut's theorem. According to (Chao, 2006)

$$J_2 = \frac{(C - (A+B)/2)}{Ma^2}, \tag{2.10}$$

where A, B and C ($C > B >= A$) are the Earth's mean principal moments of inertia along he x, y and z axis, respectively; and M is the mass of the Earth.

Just like the geocenter motion, variations in J_2 can be obtained with two classes of methods, direct and indirect methods, which are briefly reviewed in the following sections.

2.2.1. Direct Methods

Observations of J_2 variations are traditionally obtained from an analysis of SLR data. Since the launch of the LAGEOS-1 satellite in 1976, high-quality J_2 variations have been provided to the science community for over four decades. J_2 variations were firstly reported by Yoder et al. (1983), who demonstrated that LAGEOS-1 data are sensitive to both seasonal and secular changes in the Earth's gravity field. The linear trend in J_2 ($\dot{J}_2$) was determined to be $-3 \times 10^{-11} yr^{-1}$, which can be reconciled with predictions of GIA models. However, J_2 observations based on only one SLR satellite are correlated with higher degree zonal terms, such as J_4 and J_6, which were taken from a particular GIA model. An analysis of another SLR satellite, Starlette, was conducted by Cheng et al. (1989). $\dot{J}_2$ was determined to be $(-2.5 \pm 0.3) \times 10^{-11} yr^{-1}$,

which is in good agreement with the previous value. Also, J_3 and J_4 were determined together with J_2, which reduced mutual aliasing. Subsequently, data from multiple SLR satellites including LAGEOS 1 and 2, Starlette, Ajisai, Etalon 1 and 2, Stella and BE-C, were combined to determine the temporal Earth gravity field changes (Cheng et al., 1997; Cheng and Tapley, 1999). J_2 as well as other zonal harmonics were well separated and determined. These studies further confirmed the presence of the linear trend and seasonal variability in the J_2 time-series. As longer J_2 time-series became available, a possible reversal of the trend in J_2 around 1998 (referred to as the 1998 anomaly) attracted significant attention (Cox and Chao, 2002). The anomaly was studied extensively (e.g. Dickey et al., 2002; Cazenave and Nerem, 2002; Chao et al., 2003) and has been interpreted as the result of a mass redistribution between polar glaciers and tropical oceans (Dickey et al., 2002). Later, Cheng and Tapley (2004) pointed out that the 1998 anomaly was not a unique event, but rather a superposition of the inter-annual variations and the decadal variations, which lead to the abnormal fluctuations of J_2. The inter-annual variations of 4 to 6 years were associated with the strong ENSO events. The causes of decadal variations, on the other hand, were not clear at that time but are now shown to be dominated by ice mass loss in Greenland and Antarctica (Nerem and Wahr, 2011; Seo et al., 2015). Benjamin et al. (2006) found that a series of anomalies like the 1998 anomaly can be found in the J_2 residuals if the Earth body tide were better modeled. Recently, Cheng et al. (2013a) showed that the long-term J_2 variations are more quadratic than linear in nature, which suggests an acceleration of glaciers and ice-sheets melting during the last decade.

The GRACE mission aims to monitor changes in the Earth's gravity field. Temporal variations in J_2 are therefore naturally provided, which is another source of directly observed J_2 variations. Unfortunately, the quality is rather poor as the J_2 variation time-series is corrupted by large periodic aliases of 161 days (e.g. Chen et al., 2004, 2005). The causes of such aliases are partially attributed to thermal-dependent systematic errors in the satellite accelerometer data (Cheng and Ries, 2017). Consequently, the GRACE-observed J_2 variations are recommended to be replaced with those based on SLR data (Cheng and Ries, 2012).

2.2.2. Indirect Methods

Variations in J_2 can also be obtained indirectly. Earth rotation theory indicates that excitation of length-of-day (LOD) changes due to surface mass load variations is proportional to J_2 changes (Lambeck, 2005). Therefore, provided that it is possible to effectively estimate and remove the excitations not related to mass loading, J_2 variations can be directly determined from LOD changes. The underlying assumption here is that after the effects of tides, winds, and currents have been removed, the residual signal is dominated by the effects of surface and interior mass loads. Usually, the GIA effects are removed by eliminating the linear trend from the LOD time-series. Thus, the LOD method cannot estimate the trend in J_2. The earthquake-related signals, on the other hand, are ignored. Using this method, Chen (2000)

derived J_2 changes from the daily LOD time-series prepared by Gross (1996), which is obtained from a Kalman combination of various space geodetic observations including GPS, SLR, very long baseline interferometry (VLBI), and lunar laser ranging (LLR). However, the obtained J_2 time-series is less accurate than those based on SLR data. This is probably owing to the imperfect removal of wind and ocean current effects (Chen, 2000). Gross et al. (2004) estimated two J_2 time-series. One based on global GPS inversion and the other based on a newer LOD time-series from Gross (2003). However, the agreement of these two solutions is also quite poor. This could be expected since the excitations in Earth's rotation are primarily caused by changes in atmospheric winds and the meteorological models used at that time could not estimate large-scale wind variations with a sufficient accuracy. After using more advanced meteorological models, the agreement between the J_2 variations based on LOD time-series and SLR data or GPS global inversion have been significantly improved (Chen and Wilson, 2003; Chen et al., 2005; Chen and Wilson, 2008; Bourda, 2008; Meyrath et al., 2013; Chen et al., 2016).

The inversion approach for geocenter motion determination discussed in section 2.1.2 is able to estimate changes in higher degree coefficients as well. Using the global GPS inversion approach, Wu et al. (2003) obtained a J_2 time-series in line with those determined from SLR data in terms of seasonal variations (e.g. Cheng and Tapley, 1999; Cox and Chao, 2002). Following studies using the inversion approach also confirmed that the GPS-derived J_2 seasonal variations are remarkably close to the SLR solutions (e.g. Wu et al., 2006; Lavallée et al., 2010; Rietbroek et al., 2012b). As we will show in the following chapters (Chapter 3 and 4), the GRACE-OBP approach (Swenson et al., 2008) is also able to co-estimate J_2 (C_{20}) with geocenter motion (C_{10}, C_{11}, S_{11}) estimates.

Finally, C_{20} variations can also be obtained from numerical climate models (Chao and Eanes, 1995; Chen and Wilson, 2003, 2008; Meyrath et al., 2013, 2017). Just like geocenter motion estimates obtained this way, such solutions are currently not reliable due to poorly modeled hydrology, continental glaciers, and other contributors.

2.3. Summary

The existing methodologies used to estimate geocenter motion and variations in J_2 can be divided into two categories, i.e., direct and indirect (inversion) methods.

Geocenter motion can be estimated directly from three geodetic techniques, SLR, GNSS and DORIS. Due to the network effect, all direct methods deliver the motion of CM with respect to CN rather than CF. Even the most accurate technique among the three, SLR, is still not able to produce a satisfactory geocenter motion time-series. On the other hand, solutions based on the inversion methods are less noisy, and agree better between different variants. These methods are first developed to

utilize GPS data only. GRACE data and OBP model predictions are then incorporated to facilitate a simultaneous estimation of other higher-degree coefficients mainly in order to reduce aliases into the interested low-degree component. A variant of inversion approach recently developed by Swenson et al. (2008) relies primarily on GRACE data and an OBP model to estimate geocenter motion. The discrepancy in the Z-component of geocenter motion time-series of this method and other methods indicates a room for improvement.

Changes in the Earth's dynamic oblateness are currently best derived from SLR data, a traditionally adopted direct method. Estimates based on the LOD data are still unsatisfactory due to an insufficient accuracy of meteorological models which are needed to remove signals related to winds and ocean currents from the LOD time-series. Inversion methods using GNSS data supported by GRACE data and OBP models, on the other hand, are now providing comparable J_2 solutions from SLR data.

Thus, inversion methods are promising for estimating both geocenter motion and variations in J_2. In the following chapters, we will further develop those methods. Among others, we will extend the method of Swenson et al. (2008) to estimate variations in J_2 and explore the implementation details for improvements.

3

Observed changes in the Earth's dynamic oblatness from GRACE data and geophysical models

This chapter has been published in Journal of Geodesy **1**, 90 (2016) (Sun et al., 2016a)

3.1. Introduction

Monthly Earth gravity field models based on data from the Gravity Recovery and Climate Experiment (GRACE) satellite mission (Tapley et al., 2004), which was launched in 2002, are being released by several data analysis centers (e.g., Center for Space Research (CSR) model RL05 (Bettadpur, 2012), GeoForschungsZentrum (GFZ) model RL05a (Dahle et al., 2013), Jet propulsion Laboratory model (JPL) RL05 (Watkins, 2012), (Delft Mass Transport model) DMT (Liu et al., 2010)). In spite of continuous improvements in data processing techniques, very low-degree spherical harmonic coefficients still cannot be determined with high accuracy. This is largely due to the mission design (low orbits, limited separation of the satellites, etc.) (Chen et al., 2005). In particular, this concerns variations of the C_{20}^g coefficient (ΔC_{20}^g, denoted as C_{20}^g hereafter for simplicity), which describes changes of the Earth's dynamic oblateness J_2 ($J_2 = -\sqrt{5}C_{20}^g$, where the factor $\sqrt{5}$ implicitly means that the C_{20}^g is normalised). Estimations of this coefficient are corrupted by 161-day-period ocean tide aliases due to unknown reasons (Cheng et al., 2013a). Therefore, the C_{20}^g coefficient in GRACE gravity field models is recommended to be replaced with estimates from other techniques such as Satellite Laser Ranging (SLR), which is likely to provide the most accurate C_{20}^g information so far (Cheng and Tapley, 2004).

An alternative source of information about variations of low-degree coefficients is surface mass loading inferred from the GPS-sensed solid Earth deformation, an approach known as the inversion method (Blewitt et al., 2001; Gross et al., 2004; Wu et al., 2012).

Swenson et al. (2008) developed a new method method to determine the degree-1 coefficients by combining GRACE information with Ocean Bottom Pressure (OBP) data, so that the usage of GPS data is not needed.

Here we extend the methodology by Swenson et al. (2008) further to estimate the monthly C_{20}^g coefficients from other GRACE gravity field model coefficients supported by the C_{20}^g coefficients from an Ocean Bottom Pressure (OBP) model and a Glacial Isostatic Adjustment (GIA) model. We validate our solutions against SLR-derived estimates. This study is motivated by the following considerations: (i) The estimated C_{20}^g coefficients are predominantly based on GRACE data, this may reduce the latency time, which can be rather long if other geodetic techniques are involved (e.g. SLR). (ii) Dense and evenly distributed measurements are used as the input. (iii) The proposed procedure has better prospects regarding an increasing accuracy of future satellite gravity mission and related geophysical models. In addition, one will be able to use the proposed procedure for a mutual validation of the estimates based on GRACE data and on other techniques.

3.2. Methodology

Following Eq. (11) in Swenson et al. (2008), one can derive a similar equation for the determination of the C_{20} coefficient:

$$C_{20} = \frac{4\pi C_{20}^{\text{ocean}}}{\int \bar{P}_{20}(\cos\theta)\vartheta(\theta,\phi)\bar{P}_{20}(\cos\theta)d\Omega} - \frac{\int \bar{P}_{20}(\cos\theta)\vartheta(\theta,\phi)\sum_{l=1}^{\infty}\sum_{m=0}^{l}\bar{P}_{lm}(\cos\theta)\{C_{lm}\cos m\phi + S_{lm}\sin m\phi\}d\Omega}{\int \bar{P}_{20}(\cos\theta)\vartheta(\theta,\phi)\bar{P}_{20}(\cos\theta)d\Omega} \tag{3.1}$$

where C_{20}^{ocean} represents the oceanic component of C_{20}. Integrals are defined over the entire globe, $d\Omega = \sin\theta d\theta d\phi$ is an element of solid angle. The summations exclude the estimated term C_{20}. Indices l and m stand for spherical harmonic degree and order, respectively. $\bar{P}_{lm}$ are normalised associated Legendre functions. θ is colatitude in spherical coordinates, ϕ is longitude, $\vartheta(\theta,\phi)$ denotes the ocean function, which equals 1 over ocean and 0 over land. C_{20}, C_{lm} and S_{lm} denote the "mass coefficients" describing the surface mass change and are related to the dimensionless Stokes coefficients C_{20}^g, C_{lm}^g and S_{lm}^g by

$$\begin{Bmatrix} C_{lm} \\ S_{lm} \end{Bmatrix} = \frac{a\rho_{\text{earth}}(2l+1)}{3(1+k_l)} \begin{Bmatrix} C_{lm}^g \\ S_{lm}^g \end{Bmatrix}, \tag{3.2}$$

in which a is the semi-major axis of the reference ellipsoid, ρ_{earth} is the Earth's average density and k_l denotes the degree-l load Love number (Wahr et al., 1998).

Following Swenson et al. (2008), one can easily extend Eq. (3.1) to the case when four coefficients — C_{10}, C_{11}, S_{11}, and C_{20} — have to be simultaneously estimated, for which purpose a system of linear equations has to be solved:

$$\begin{bmatrix} I_{10C}^{10C} & I_{11C}^{10C} & I_{11S}^{10C} & I_{20C}^{10C} \\ I_{10C}^{11C} & I_{11C}^{11C} & I_{11S}^{11C} & I_{20C}^{11C} \\ I_{10C}^{11S} & I_{11C}^{11S} & I_{11S}^{11S} & I_{20C}^{11S} \\ I_{10C}^{20C} & I_{11C}^{20C} & I_{11S}^{20C} & I_{20C}^{20C} \end{bmatrix} \begin{bmatrix} C_{10} \\ C_{11} \\ S_{11} \\ C_{20} \end{bmatrix} = \begin{bmatrix} C_{10}^{\text{ocean}} \\ C_{11}^{\text{ocean}} \\ S_{11}^{\text{ocean}} \\ C_{20}^{\text{ocean}} \end{bmatrix} - \begin{bmatrix} G_{10C} \\ G_{11C} \\ G_{11S} \\ G_{20C} \end{bmatrix}, \tag{3.3}$$

where the following notations have been used:

$$I_{20C}^{11S} = \frac{1}{4\pi}\int d\Omega \\ \bar{P}_{11}(\cos\theta)\sin(1\times\phi)\vartheta(\theta,\phi)\bar{P}_{20}(\cos\theta)\cos(0\times\phi)) \\ \text{(similar for the other elements of matrix } I\text{)}, \tag{3.4}$$

and

$$G_{20C} = \frac{1}{4\pi}\int d\Omega\bar{P}_{20}(\cos\theta)\cos(0\times\phi)\vartheta(\theta,\phi) \\ \sum_{l=2}^{\infty}\sum_{m=0}^{l}\bar{P}_{lm}(\cos\theta)\{C_{lm}\cos m\phi + S_{lm}\sin m\phi\} \\ \text{(similar for the other elements of vector } G\text{)}, \tag{3.5}$$

in which the summations exclude the terms that are estimated.

To solve the system of linear equations and obtain degree-1 and C_{20}^{g} dimensionless Stokes coefficients, one needs (i) the oceanic component of degree-1 and C_{20}^{g}, (ii) higher-order Stokes coefficients and (iii) GIA model coefficients. The input and output shown in the equation are mass coefficients, but they are directly related to the Stokes coefficients mentioned here through Eq. (3.2). The Stokes coefficients used in this study come directly from the GRACE level-2 products (also known as GSM coefficients), for which the oceanic and atmospheric mass variations are not included. These variations are provided by the Atmosphere and Ocean De-aliasing level-1B (AOD1B) products (Flechtner and Dobslaw, 2013) and distributed along with the GSM coefficients in two forms: GAC, which include the global oceanic and atmospheric effects, and GAD, which have the atmospheric contribution over the continents set to zero. Both GAC and GAD files contain dimensionless Stokes coefficients up to degree 100. The GAC coefficients contain the contribution that has been removed from the full GRACE Stokes coefficients to receive GSM coefficients, while GAD coefficients represent the ocean bottom pressure variations. To make sure the input coefficients are compatible, the same oceanic and atmospheric effects need to be removed from GRACE coefficients and the coefficients associated with the ocean component, e.g. C_{20}^{ocean}. Since the ocean component lacks the contribution from atmosphere over the land, it is therefore the GAD (rather than GAC) coefficients that should be subtracted from the ocean component. With this procedure, the output will also be GSM-like coefficients. If the full degree-1 and C_{20}^{g} coefficients are needed, the contribution of GAC product should be restored afterwards.

An alternative procedure requires that the AOD1B product is first added back to GSM coefficients and then full degree-1 and C_{20}^{g} coefficients are estimated directly. Although the latter procedure is stated to be equivalent to the first one in Swenson et al. (2008), it is not favoured in this study for the reason outlined in section 3.3.2.

3.3. Input Data

3.3.1. Oceanic C_{20}

As has been mentioned above, the GAD contribution, denoted as C_{20}^{GAD}, needs to be removed from C_{20}^{ocean} coefficients. The GAD coefficients represent the OBP model that describes the pressure on the sea floor from both air and water column above. The water columns are output from the ocean model from circulation and tides (OMCT) (Thomas, 2002). This ocean model applies the Boussinesq approximation and thus essentially conserves the ocean volume. A thin uniform layer of water is then added or removed to conserve the total ocean mass, As a result, C_{20}^{GAD} should include the contribution of internal oceanic mass redistribution as well as the atmospheric mass variations over the ocean regions. After removing C_{20}^{GAD}, the remaining of C_{20}^{ocean} reflects only he water exchange between ocean and continents ($C_{20}^{\mathrm{exchange}}$). Therefore, the input C_{20}^{ocean} coefficients are equal to $C_{20}^{\mathrm{exchange}}$ in our study in view of the fact that OMCT is exploited as the OBP model.

The aforementioned ocean model does not include the water exchange with the continents, which, however, can be provided by GRACE (except for the contribution of the degree-1 components) (Chambers and Schröter, 2011). Therefore, $C_{20}^{\mathrm{exchange}}$ is computed by using GRACE data integrated over the continental areas to infer total mass variations (which are opposite to mass variations in the oceans, assuming mass conservation in the Earth system). Once the monthly mass variation is known, the value of $C_{20}^{\mathrm{exchange}}$ is obtained by assuming a certain spatial distribution of the exchanged water over the oceans. We implement two different approaches: (i) water redistributes as a uniform layer (eustatic approach, as in Swenson et al. (2008)); (ii) water redistributes accounting for Self-Attraction and Loading effects (SAL approach). SAL effects (or fingerprints, Mitrovica et al. (2001)) are computed by solving the sea-level Eq. (Farrell and Clark, 1976), including the feedback from Earth rotation (Milne and Mitrovica, 1998). It is worth noting that using GRACE to constrain total mass change over the continents requires the availability of a complete GRACE solution, which includes the coefficients being estimated through Eq. (3.3). Therefore, $C_{20}^{\mathrm{exchange}}$ needs to be determined through an iterative approach (starting from a GRACE solution where the four estimated coefficients are set equal to zero, later updated with preliminary estimates of the same coefficients). Convergence is very quick, with the difference between subsequent solutions being smaller than 0.1% in 3 or 4 iterations.

The degree-1 coefficients are estimated similarly, simultaneously with C_{20}

3.3.2. GRACE Gravity Field Models

In this paper, we present results based on CSR RL05, GFZ RL05a and JPL RL05 model series in the period from January 2003 to May 2013, all complete to or

truncated at degree 60.

All the GRACE-based monthly gravity fields contain spatially-correlated noise that reveals itself in the form of meridionally-oriented stripes in the spatial domain. In order to solve the sea level equation and account for self-attraction and loading effects, we need to know the spatial distribution of the land load. For this purpose, we use publicly available solutions that have been post-processed by means of the DDK4 filter (Kusche et al., 2009) (http://icgem.gfz-potsdam.de/ICGEM/). The DDK4 filter is decorrelation filter making use of error covariance matrices, and an a priori signal covariance matrix in the spherical harmonic domain. In this way, the filtering ensures that a higher noise or/and lower signal level means harder damping and vice versa. Ultimately, the effect of this filter is somewhat similar to that of a combination of empirical destriping algorithm (Swenson and Wahr, 2006) and Gaussian filter (Wahr et al., 1998).

When using Eq. (3.3) we need to deal with the limited spatial resolution of the GRACE gravity field models, which causes signals to spread over (or leak into) wider areas. The signal leakage is further increased by applying a filter, such as DDK4. As a result, the available observations cannot distinguish whether mass variations occurring in coastal areas are originating from the land or from the ocean. An attempt to define an ocean function without taking this fact into account may lead to a miscalculation of the total mass exchange between land and oceans as well as of the G vector. We correct for signal leakage by introducing a buffer zone around all land areas, similarly to what is done by Swenson et al. (2008) when computing the total ocean mass change. Differently from that study, we also consider the buffer zone to be part of the land areas when we define the ocean function $\vartheta(\theta,\phi)$, which means that we include the buffer zone in the definition of the G vector. We will show that such a buffer is crucial to obtain solutions close to SLR estimates. The use of a buffer introduces the risk that mass redistribution due to ocean dynamical processes in coastal areas is erroneously attributed to land processes. However, the problem is largely reduced by using GSM coefficients in Eq. (3.3), under the assumption that the AOD products capture most of the ocean signal.

3.3.3. GIA Models

The method discussed above and Eq. (3.2) imply that gravity field variations are solely due to a redistribution of mass at the Earth's surface. Solid Earth contributions such as those of tectonics and GIA should therefore be removed. Here, only GIA is accounted for as proposed by Swenson et al. (2008). The removed GIA signal is restored at the final data processing stage. Since GIA is characterised by a linear trend, the choice of a specific GIA model has no impact on seasonal and other short-term signals.

Considering that available GIA models are highly uncertain, we only show the resulting C_{20}^{g} trends for a few GIA realisations, based on different Earth rheologies

and on two Antarctic ice histories. A full-scale sensitivity study is beyond the scope of this paper.

Four GIA models have been used. All models are based on the ICE-5G ice history (Peltier, 2004). Model-A, -B and -C are based on a simplified version of viscosity model VM2 (Peltier, 2004), while Model-D assumes a lower mantle with a higher viscosity (10^{22} Pa s) than VM2 (Mitrovica and Forte, 1997). Model-A is taken from A et al. (2012), who computed it for a compressible earth model, while Model-B is our own realization and makes the commonly used assumption of incompressibility within the Solid Earth (Spada et al., 2011). In Model-C the Antarctic component is computed separately, based on ice history IJ05 (Ivins and James, 2005) and on a different viscosity profile than VM2 (consisting of a 60-km-thick elastic lithosphere and of a lower mantle with a viscosity of 10^{22} Pa s). This Antarctic setup provides uplift rates very close to independent results based on satellite data (Riva et al., 2009)).

3.4. Results

The following factors can affect the estimation of C_{20}^g coefficients: (i) the choice of the input models (GRACE solutions, OBP and GIA models) and (ii) implementation details (buffer zone width, the filter applied to GRACE solutions and whether or not accounting for self-attraction and loading effects). By trying different combinations of data processing parameters, we produced many variants of C_{20}^g time-series. Each of them was compared with the state-of-the-art C_{20}^g time-series based on SLR data from five geodetic satellites (LAGEOS-1 and 2, Starlette, Stella and Ajisai) (Cheng et al., 2013a). Since all the results discussed are presented in the form of GSM-like coefficients, the AOD1B product (GAC coefficients) have also been removed from the reference SLR time-series. We estimate bias, linear trend, acceleration, as well as annual and semi-annual periodic terms for each time-series and make a comparison with corresponding parameters derived from the SLR-based time-series.

We first compare de-trended (linear-trend removed) time-series both visually and in terms of variance, where the percentage of the SLR-variance explained is defined as $R^2 = 1 - < SLR - MODEL > / < SLR >$, where MODEL represents our estimation in this study and <> denotes the variance operator. We also compare annual amplitudes and phases against those of the SLR solution. Comparison of de-trended time-series will lead to results invariant to the GIA model used. Later, we use one selected solution to compare the linear trend estimates resulting from different GIA models.

3.4.1. Seasonal Variations

In Figure 3.1, we show a few time-series meant to illustrate the sensitivity of our GRACE-based solutions to implementation details and input models. The reference SLR solution is represented by a black solid line and by a grey band, indicating mean value and one standard deviation, respectively. In Table 4.4 we show statistics for the same models, as well as for a few additional experiments (different buffer widths, use of the DDK4 filter).

In Figure 3.1a, we show the role of implementation details, namely of the use of a buffer zone and of the computation of SAL effects, based on GRACE CSR RL05 solutions. Not using any buffer and ignoring SAL effects (green line) largely underestimates the amplitude of the seasonal cycle. Nonetheless, most features of the SLR time-series are already recognisable, such as the relative size of maxima and minima, as well as their phase. This solution explains about 59% of the SLR variance, where the annual cycle is rather close in phase, but clearly smaller in amplitude (65% of SLR). The addition of a 200 km buffer zone (blue line) largely improves the overall fit as well as the size of the peak amplitudes. The amplitude of the annual signal becomes statistically equivalent (within 2σ) to the SLR solution. However, the improvement on the overall fit is moderate, where the new solution explains about 68% of the SLR variance. Further increasing the width of the buffer zone to 250 km and 300 km will begin to lower the explained variance slightly. When using a 300 km buffer width, the estimated annual amplitude becomes smaller. More detailed analysis of the buffer zone width will be discussed in Chapter 4. A more advanced way of handling signal leakage may also be useful and will be a subject of future studies.

Finally, accounting for SAL effects (red line) has a rather small effect on the variance, but significantly affects the amplitude of the estimated annual signal, which becomes equivalent to the SLR estimate. Note that the solution closest to SLR when including SAL effects makes use of a smaller buffer (150 km) than in the eustatic case. The effects of feedback from the Earth rotation are accounted for during the computation of SAL. These effects on the estimated C_{20}^{g} coefficients are negligible.

It is worth mentioning that the elimination of the buffer zone from the ocean functions prevents the accounting for SAL effects in the coastal regions. We have verified, however, that this has a little impact on the solution. We have considered the following two scenarios: (i) solving the sea level equation for the whole ocean; (ii) solving the sea level equation for a slightly smaller ocean by reducing the ocean function 150 km along all boundaries while keeping the continental load unchanged (i.e. ignoring the mass variation inside the 150-km-wide buffer zone seen by GRACE). The resulting amplitude of the annual signal in the second scenario increases, compared to the first one, by only about 2%, which is less than the uncertainty.

In Figure 3.1b, we fix the implementation parameters to their optimal values

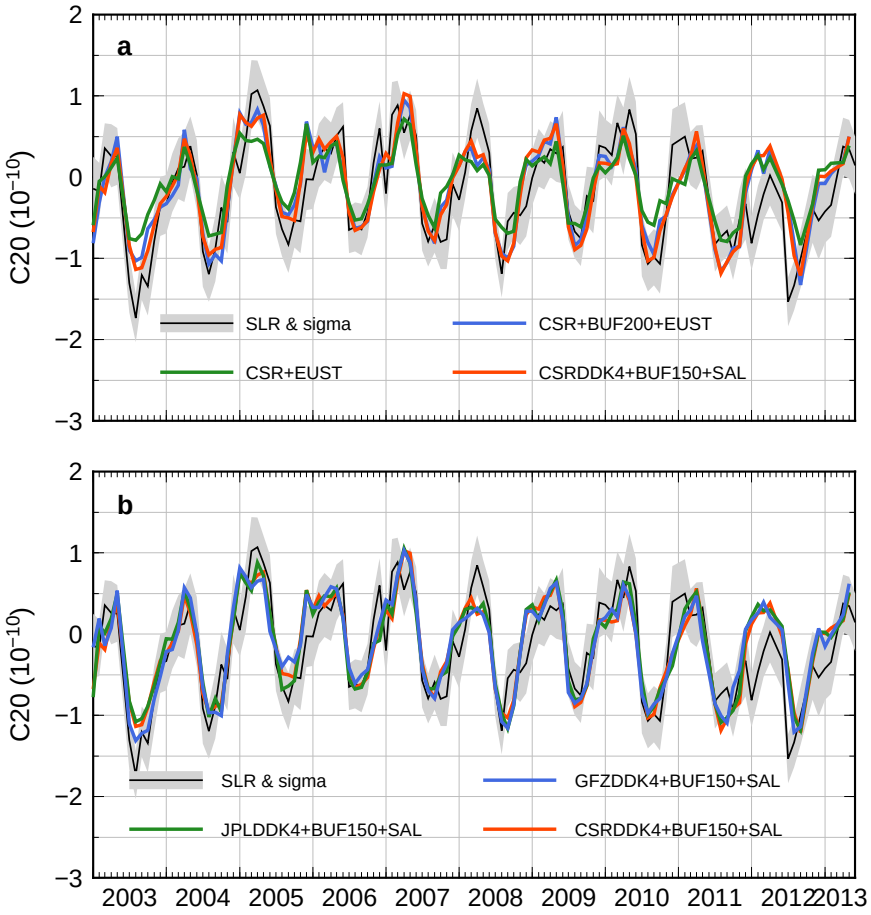

Figure 3.1: Selected GRACE-based C_{20}^{g} solutions obtained using different implementation details and input models, together with a SLR-derived solution and its standard deviation. A linear trend has been removed. (a) Shows the role of implementation details. (b) Illustrates the effect of using different GRACE solutions after fixing the implementation parameters. The reference SLR solution and its one standard deviation is shown in both panels (black solid line and grey band). GRACE solution used, buffer zone width (not shown if no buffer zone used) and whether the SAL effects are accounted for are shown in the name of each solution.

Table 3.1: Statistics for GSM-like C_{20}^{g} time-series estimated with different strategies and for different GRACE solutions. The trend is based on GIA realisation Model-C, where the GIA contribution to the trend has been restored. The solution SLR FULL, where the AOD1B fields have not been removed, is provided as a reference. The highlighted solution is available at on line at http://www.citg.tudelft.nl/c20.

	Var. Expl.	Trend	Annual signal	
			Amplitude	Phase
		$(10^{-11} yr^{-1})$	(10^{-11})	(day)
SLR	100.0 %	-1.0 ± 0.1	6.9 ± 0.4	82.0 ± 3.3
CSR+EUST	58.6 %	$+0.1 \pm 0.1$	4.5 ± 0.2	71.3 ± 2.8
CSR+BUF150+EUST	68.0 %	-1.2 ± 0.1	6.1 ± 0.3	76.9 ± 2.7
CSR+BUF200+EUST	68.2 %	-1.4 ± 0.1	6.3 ± 0.3	77.5 ± 2.8
CSRDDK4+EUST	57.4 %	$+0.3 \pm 0.0$	4.1 ± 0.2	70.1 ± 2.7
CSRDDK4+BUF150+EUST	68.2 %	-0.8 ± 0.1	5.4 ± 0.2	75.5 ± 2.6
CSRDDK4+BUF200+EUST	69.2 %	-1.1 ± 0.1	5.6 ± 0.3	76.3 ± 2.6
CSRDDK4+BUF250+EUST	68.9 %	-1.4 ± 0.1	5.6 ± 0.3	77.4 ± 2.9
CSRDDK4+BUF300+EUST	67.3 %	-1.6 ± 0.1	5.4 ± 0.3	77.2 ± 3.1
CSRDDK4+SAL	61.5 %	-0.0 ± 0.1	4.8 ± 0.2	70.5 ± 2.6
CSRDDK4+BUF150+SAL	**70.8 %**	$\mathbf{-1.3 \pm 0.1}$	$\mathbf{6.8 \pm 0.3}$	$\mathbf{77.4 \pm 2.3}$
CSRDDK4+BUF200+SAL	70.8 %	-1.6 ± 0.1	7.1 ± 0.3	78.3 ± 2.3
GFZDDK4+BUF150+SAL	71.6 %	-1.4 ± 0.1	6.9 ± 0.3	75.2 ± 2.5
JPLDDK4+BUF150+SAL	70.0 %	-1.4 ± 0.1	7.0 ± 0.3	78.8 ± 2.2
SLR FULL		-1.0 ± 0.2	14.2 ± 0.7	52.4 ± 2.8

(using a buffer width of 150 km and taking into account SAL effects) and show the effect of using different GRACE solutions. The GFZ solution provides the best overall fit (71.6% of the SLR variance explained and same amplitude of the annual signal). Nonetheless, all three time-series are very close to each other and the amplitude of the annual signal is statistically equivalent (within 1σ).

The phase estimates are not significantly affected by any of the above mentioned factors. The differences of phase estimates compared to those based on SLR data are all within ten days.

3.4.2. Trend Estimates and GIA

Table 4.4 also lists linear trend estimates when using GIA Model-C. Note that those trends are still based on the GSM-like solutions, but we have verified that long-term trends in atmospheric pressure over land and in OBP are negligible. The table shows that both buffer and SAL effects have a large impact on the trend due to present-day mass transport (PDMT). The estimated trend is zero without buffer and SAL, but becomes 40% larger than the SLR trend for the model that provides the best fit of the seasonal signal. The largest effect originates from the buffer, but also SAL effects are sizeable (causing a further increase of up to 14% when the buffer width is 200 km).

In Table 3.2, we list the effect of using different GIA models for the results based on DDK4 filtered CSR solutions in combination with a 150-km buffer and taking SAL effects into account (i.e. CSRDDK4+BUF150+SAL). Similar conclusions hold for other setups. In order to allow an easier comparison with previous studies, we show the obtained trends in terms of $\dot{J}_2$.

Table 3.2: J_2 trends estimated using different GIA models (unit $10^{-11}\,yr^{-1}$). Results are based on solution CSRDDK4+BUF150+SAL.

	GIA	PDMT	total
SLR	/	/	2.2 ± 0.2
Model-A	-3.3	7.4	4.1 ± 0.2
Model-B	-3.6	7.1	3.6 ± 0.2
Model-C	-3.6	6.6	3.0 ± 0.2
Model-D	-5.7	9.1	3.4 ± 0.2

The use of GIA models allows us to separate the contribution of GIA from that of PDMT. The GIA contribution is uniquely defined for each model, while the PDMT value depends on the full GIA spectrum and is therefore affected by implementation details.

The smallest (in absolute value) $\dot{J}_2$ of GIA comes from the model by A et al. (2012) (Model-A) which at the same time produces a relatively large estimate for

Table 3.3: Estimated annual amplitude and phase of global ocean mass variations.

Measurement Source	Method	Time Span	Amplitude (mm)	Phase(day)
CSR+EUST	GRACE	2003 - 2013	8.8 ± 0.2	285 ± 2
CSR+BUF150+EUST	GRACE	2003 - 2013	9.5 ± 0.2	280 ± 1
CSR+BUF200+EUST	GRACE	2003 - 2013	9.4 ± 0.2	279 ± 1
CSRDDK4+EUST	GRACE	2003 - 2013	8.5 ± 0.2	285 ± 1
CSRDDK4+BUF150+EUST	**GRACE**	**2003 - 2013**	$\mathbf{9.0 \pm 0.2}$	$\mathbf{279 \pm 1}$
CSRDDK4+BUF200+EUST	GRACE	2003 - 2013	9.0 ± 0.2	279 ± 1
Chambers et al. (2004)	GRACE	2002 - 2004	8.4 ± 1.1	270 ± 8
	Steric-corrected altimetry	2002 - 2004	8.5 ± 0.7	282 ± 5
Wu et al. (2006)	GPS+GRACE+OBP	1993 - 2004	9.0	238
Rietbroek et al. (2009)	GPS+GRACE+OBP	2003 - 2007	8.7	247
Wouters et al. (2011)	GRACE	2003 - 2010	9.4 ± 0.6	280 ± 6
Siegismund et al. (2011)	GRACE	2002 - 2007	8.4	250
	Steric-corrected altimetry	2002 - 2007	9.7, 9.6, 9.7	229, 232, 223
Hughes et al. (2012)	OBP models	19 years	8.5, 9.3	266, 271
Bergmann-Wolf et al. (2014)	GRACE	2003 - 2012	9.8 ± 0.5	278

Table 3.4: Statistics for the three cartesian components of different geocenter motion solutions. SWENSON_TELLUS has been downloaded from the Tellus website; SWENSON_SETUP uses the same setup as SWENSON_TELLUS, but it results from the simultaneous estimation of C_{20}^{g}; CSRDDK4+BUF150+SAL is the setup that provides the best agreement to SLR-derived C_{20}^{g}, for the same GRACE solutions and GIA model (Model-A). The GIA contribution to the trend is not restored, as in the SWENSON_TELLUS case.

	Trend	Annual signal	
		Amplitude	Phase
	(mm/yr)	(mm)	(day)
X			
SWENSON_TELLUS	-0.07 ± 0.01	1.26 ± 0.05	97 ± 3
SWENSON_SETUP	-0.08 ± 0.01	1.30 ± 0.06	97 ± 3
CSRDDK4+BUF150+SAL	-0.05 ± 0.02	1.50 ± 0.06	96 ± 3
Y			
SWENSON_TELLUS	-0.02 ± 0.02	1.50 ± 0.07	-76 ± 3
SWENSON_SETUP	-0.03 ± 0.02	1.42 ± 0.07	-79 ± 3
CSRDDK4+BUF150+SAL	$+0.02 \pm 0.02$	1.67 ± 0.07	-72 ± 2
Z			
SWENSON_TELLUS	-0.19 ± 0.02	1.77 ± 0.07	92 ± 2
SWENSON_SETUP	-0.20 ± 0.01	1.73 ± 0.06	92 ± 2
CSRDDK4+BUF150+SAL	-0.35 ± 0.02	2.48 ± 0.08	88 ± 2

the contribution of PDMT, leading to a larger $\dot{J}_2$ value than Model-B based on an incompressible earth. Substituting the Antarctic contribution of ICE-5G with results based on IJ05 (Model-C) has no impact on $\dot{J}_2$ caused by GIA, likely due to trade-offs between the different ice history and the different viscosity structure used for the Antarctic model. However, the use of IJ05 does reduce the mass loss estimate from Antarctica, leading to a smaller PDMT contribution and to the smallest total $\dot{J}_2$. A higher viscosity in the lower mantle (Model-D) leads to larger contributions from both GIA and PDMT, which compensate each other and result in the second smallest total $\dot{J}_2$.

None of the GIA models tested here provides a very good fit to the $\dot{J}_2$ value determined from SLR. However, our results show a positive sign of $\dot{J}_2$, confirming the findings from earlier studies on the inversion of $\dot{J}_2$ observed since 1998 (Cox and Chao, 2002), which has been attributed to an increased contribution from PDMT (Dickey et al., 2002; Cheng and Tapley, 2004; Nerem and Wahr, 2011; Cheng et al., 2013a).

3.4.3. Eustatic Sea-level Variability and Geocenter Motion

Finally, it is worth having a brief look at two byproducts of our study: the solutions for eustatic sea-level variability (see Table 3.3) and for geocenter motion simultaneously obtained with C_{20}^{g} (see Table 3.4).

The eustatic sea-level variability estimated using the approach described in section 3.3.1 has been compared with recent results based on alternative methods and measurement technologies (Chambers et al., 2004; Rietbroek et al., 2009; Wouters et al., 2011; Siegismund et al., 2011; Hughes et al., 2012; Bergmann-Wolf et al., 2014). Our results are in line with those estimates in terms of annual amplitude and phase (Table 3.3).

The co-estimated geocenter motion is significantly different from the one derived from the degree-1 coefficients published on the Tellus website (ftp://podaac.jpl.nasa.gov/allData/tellus/L2/degree_1), both in terms of a trend and annual amplitudes, especially for the Z-component. However, the obtained results are statistically equivalent to those published in the Tellus website when we use the same setup as Swenson et al. (2008), where a 300 km buffer zone is used to reduce the signal leakage when estimating the total ocean mass variation, but no buffer zone is considered when defining ocean function. This leaves the question of the optimal estimation of geocenter motion somewhat open. A more thorough analysis of this issue will be the subject of Chapter 4.

3.5. Discussion and Conclusions

Our results (available at http://www.citg.tudelft.nl/c20) show that GRACE data at higher spherical harmonic degrees are capable of estimating seasonal changes in C_{20} to a level comparable with SLR solutions. In fact, the uncertainty (computed as formal error from an analysis of time-series) in the amplitude of the annual cycle is smaller for the GRACE-based solutions. This is an indication that our solutions may be less noisy than the SLR one, though it may also imply an underestimation of the signal not described by the fitted curve.

The main factor controlling the amplitude of the seasonal signal is the way how the problem of signal leakage in coastal areas is dealt with. Our simple approach of extending the land mask to include the first few hundreds of kilometres of coastal waters is already capable of producing a solution in close agreement with SLR, though more advanced techniques (e.g., based on mascons) could provide a better way to improve the spatial resolution of GRACE monthly fields and avoid the use of a buffer zone.

Accounting for self-attraction and loading effects driven by the redistribution of continental water masses has the effect of significantly increasing the amplitude of both annual signal and trend.

So far, we have discussed only estimates without the contribution of atmospheric and oceanic processes, assuming that the AOD1B products are correct. In the bottom line of Table 4.4 we list the full values determined from the SLR time-series prior to the subtraction of the AOD1B signal. Compared to the GSM-like solution in the top line, the amplitude of the annual signal is twice as large and its phase is shifted

by a month. This suggests that only about half of the seasonal total C_{20} signal is determined by land hydrological processes, including the cryosphere. Therefore, if the proposed methodology is used in estimating the total C_{20} signal, the accuracy of the obtained estimates strongly depend on the accuracy of the atmosphere-ocean model.

The determination of a long-term trend requires the use of a model of GIA are still very uncertain. Further investigations are warranted in the future to mitigate the uncertainties introduced by a GIA model.

One needs to bear in mind that the SLR solution is not free of systematic errors and noise (Riddell et al., 2017). The processing parameters tuned to achieve a time-series that best fits the SLR solution may therefore be biased. Further study for validation using accurate geophysical models may enable us to claim an even better solution than that from SLR.

4

Optimizing Estimates of Annual Variations and Trends in Geocenter Motion and J_2 from a Combination of GRACE data and Geophysical Models

4.1. Introduction

The Gravity Recovery and Climate Experiment (GRACE) satellite mission (Tapley et al., 2004) has been monitoring the Earth system for more than a decade since launched in 2002. Monthly gravity field solutions produced on its basis in the form of Stokes coefficients are being released by a number of data analysis centers (Bettadpur, 2012; Dahle et al., 2013; Watkins, 2012; Liu et al., 2010). Such solutions lack the three degree-1 Stokes coefficients, which are needed for a complete representation of the mass re-distribution in the Earth system. The three degree-1 coefficients are proportional to geocenter motion, here defined as the motion of Center-of-Mass (CM) of the Earth system with respect to Center-of-Figure (CF) of the solid Earth surface (Ray, 1999).

In principle, the degree-1 coefficients can be observed directly by tracking satellites, which are orbiting the CM, with ground stations, whose positions are fixed to the solid Earth's surface. Accurate satellite tracking can be achieved by making use of geodetic techniques, such as Doppler Orbitography and Radiopositioning Integrated by Satellite (DORIS), Global Positioning System (GPS), and Satellite Laser Ranging (SLR). However, DORIS- and GPS-based results are still contaminated by technique-specific errors and degraded by parameter collinearity (Altamimi et al., 2011; Meindl et al., 2013; Rebischung et al., 2014). SLR solutions (e.g Cheng et al., 2013b; Sośnica et al., 2013) are among the most accurate estimates available, but still have large uncertainties, as the sparse SLR tracking network is sensitive to the solid Earth deformation caused by surface mass loading, which makes it difficult to realize an accurate CF reference frame (Wu et al., 2012; Collilieux et al., 2009).

As shown by Blewitt et al. (2001), the translation of an elastic Earth surface caused by the degree-1 mass loading is accompanied by a specific deformation, which is detectable from globally distributed GPS measurements and can then be used to estimate degree-1 coefficients. This method has been further developed later by combining GPS data with GRACE data and an Ocean Bottom Pressure (OBP) model in a joint inversion scheme, which helps to reduce the aliases caused by uneven distribution of GPS sites as well as higher-degree loading (e.g. Kusche and Schrama, 2005; Wu et al., 2006; Rietbroek et al., 2009). Nevertheless, the GPS measurements are still biased by draconitic errors (Griffiths and Ray, 2013) and solid Earth deformation unrelated to loading, such as thermal expansion of the bedrock (Dong et al., 2002) and tectonic movements.

Swenson et al. (2008) proposed a new methodology to estimate the degree-1 coefficients, which is based on GRACE data and an OBP model (from here on called the GRACE-OBP method). With this method, regional mass variations predicted from an OBP model are used as an additional constraint to transform the GRACE-based global mass anomalies from the CM to the CF frame. The estimates by Swenson et al. (2008), however, yielded a much smaller annual amplitude of C_{10}

This chapter has been published in Journal of Geophysical Research **11**, 121 (2016) (Sun et al., 2016b)

variations than other approaches. Since the C_{10} coefficient variations correspond to the Z-component of geocenter motion, inaccuracies in their determination can lead to large errors in estimated mass variations at high latitudes. For example, a 1-mm change in the Z-component of geocenter position is equivalent to a 70-Gt mass change over Antarctica and 11-Gt mass change over Greenland (Wu et al., 2012). In previous studies, simple validations of the GRACE-OBP method were performed by using simulated time-variable gravity fields based on geophysical models (Swenson et al., 2008; Bergmann-Wolf et al., 2014). However, the purpose of those tests was limited to verifying the correctness of the theory. No effort has been made to evaluate the method performance in the context of real GRACE data.

Next to geocenter motion, the GRACE-OBP method is able to determine variations in the Earth's dynamic oblateness (J_2) (Sun et al., 2016a). Those variations are directly related to variations of the C_{20} Stokes coefficient ($J_2 = -\sqrt{5}C_{20}$). The GRACE-based C_{20} coefficient, is subject to large uncertainties (Chen et al., 2016), presumably due to tide-like aliases, and it is a common practice to replace it with estimates from other techniques, such as SLR. The GRACE-OBP method solves the problem by replacing the GRACE-based C_{20} estimate with an alternative one that does not require an explicit observation of that coefficient. Unlike the estimates based on GRACE data alone, the annual variations of J_2 obtained with the GRACE-OBP method are comparable to independent results based on SLR observations.

In this study, for the first time, we evaluate the performance of the GRACE-OBP method with respect to the determination of both geocenter and J_2 variations by means of end-to-end simulations. Apart from simulating the time-variable gravity fields using synthetic models, we also take into account the errors that are present in the real GRACE data and OBP data. As a result, we determine optimal implementation parameters of the GRACE-OBP method. The primary aim of the study is two-fold: (i) to optimize the methodology of Swenson et al. (2008) in order to improve estimates of annual variations and long-term trend in degree-1 and C_{20} coefficients, and (ii) to demonstrate the impact of this optimization on estimates based on real GRACE data.

In the following, we first introduce the GRACE-OBP method and its input data (Sect. 4.2). Realistic input data are then simulated with a synthetic Earth model plus realistically defined errors (Sect. 4.3). Subsequently, we discuss the key implementation details that may significantly affect the results (Sect. 5.3). Afterwards, degree-1 and C_{20} solutions based on both synthetic data (Sect. 4.5) and real GRACE data (Sect. 4.6) are computed and presented. Finally, we discuss our results in Sect. 4.7.

4.2. Methodology and Input Data

4.2.1. Methodology

In this section, we intended not to reproduce the derivation of all the equations used in the GRACE-OBP method (for that, a reader is referred to Swenson et al. (2008)), but rather to bring attention to several important aspects.

Time variations of Stokes coefficients of spherical harmonic degree l, order m from GRACE data, ΔC^g_{lm} and ΔS^g_{lm}, are related to the time variations of mass coefficients, ΔC_{lm} and ΔS_{lm}, depicting the surface mass re-distribution at the Earth's surface. Let us drop, for simplicity, the symbol Δ, even though all coefficients used in this study should be understood as time variations. Then, this relation is (Wahr et al., 1998):

$$\left\{ \begin{array}{c} C_{lm} \\ S_{lm} \end{array} \right\} = \frac{a\rho_{\text{earth}}(2l+1)}{3(1+k_l)} \left\{ \begin{array}{c} C^g_{lm} \\ S^g_{lm} \end{array} \right\}, \tag{4.1}$$

where a is the average Earth radius; ρ_{earth} is the average density of the Earth; and k_l is the gravitational elastic load Love number of degree l (Farrell, 1972). As a result, Stokes coefficients can be obtained from known mass coefficients. Geocenter motion (CM w.r.t. CF) in Cartesian coordinates (X, Y, Z) is then related to the three Stokes coefficients through (Blewitt, 2003):

$$\left\{ \begin{array}{c} X \\ Y \\ Z \end{array} \right\} = \frac{\sqrt{3}a}{1+k_1} \left\{ \begin{array}{c} C^g_{11} \\ S^g_{11} \\ C^g_{10} \end{array} \right\}, \tag{4.2}$$

where $k_1 = 0.021$ when the degree-1 Stokes coefficients are defined in the CF frame. Degree-1 coefficients in other reference frames except for the CM frame can also be obtained, but k_1 needs to be changed accordingly (Blewitt, 2003).

To estimate the three degree-1 mass coefficients, C_{10}, C_{11} and S_{11}, Swenson et al. (2008) proposed a matrix equation that was shown in their Eq. (12). Here, as in Sun et al. (2016a), we use its extended version which represents a system of linear equations that allows one to simultaneously co-estimate C_{20}:

$$\left[\begin{array}{cccc} I^{10C}_{10C} & I^{10C}_{11C} & I^{10C}_{11S} & I^{10C}_{20C} \\ I^{11C}_{10C} & I^{11C}_{11C} & I^{11C}_{11S} & I^{11C}_{20C} \\ I^{11S}_{10C} & I^{11S}_{11C} & I^{11S}_{11S} & I^{11S}_{20C} \\ I^{20C}_{10C} & I^{20C}_{11C} & I^{20C}_{11S} & I^{20C}_{20C} \end{array} \right] \left[\begin{array}{c} C_{10} \\ C_{11} \\ S_{11} \\ C_{20} \end{array} \right] = \left[\begin{array}{c} C^{\text{ocean}}_{10} \\ C^{\text{ocean}}_{11} \\ S^{\text{ocean}}_{11} \\ C^{\text{ocean}}_{20} \end{array} \right] - \left[\begin{array}{c} G_{10C} \\ G_{11C} \\ G_{11S} \\ G_{20C} \end{array} \right], \tag{4.3}$$

where C_{10}^{ocean}, C_{11}^{ocean}, S_{11}^{ocean} and C_{20}^{ocean} represent the degree-1 and C_{20} coefficients of oceanic mass changes, respectively. The I matrix and G vector are defined as:

$$I_{20C}^{11S} = \frac{1}{4\pi}\int d\Omega \bar{P}_{11}(\cos\theta)\sin(1\times\phi)\vartheta(\theta,\phi)\bar{P}_{20}(\cos\theta)\cos(0\times\phi), \tag{4.4}$$

$$\begin{aligned} G_{11C} = &\frac{1}{4\pi}\int d\Omega \bar{P}_{11}(\cos\theta)\cos(1\times\phi)\vartheta(\theta,\phi) \\ &\sum_{l=2}^{\infty}\sum_{m=m_0}^{l}\bar{P}_{lm}(\cos\theta)\{C_{lm}\cos m\phi + S_{lm}\sin m\phi\} \\ &\text{(other elements of the } I \text{ matrix and } G \text{ vector are similarly defined),} \end{aligned} \tag{4.5}$$

where integrals are defined globally with $d\Omega = \sin\theta d\theta d\phi$; $\bar{P}_{lm}$ are normalized associated Legendre functions; θ is colatitude in spherical coordinates; ϕ is longitude; $\vartheta(\theta,\phi)$ is the ocean function, which equals 1 over ocean and 0 over land; m_0 equals 1 if $l = 2$ and 0 if $l > 2$. The elements in the G vector are essentially estimates of the oceanic degree-1 and C_{20} coefficients based on remaining GRACE-based mass coefficients (note that the "oceanic coefficients" are defined as mass coefficients describing only the mass re-distribution in the ocean area). Surface spherical harmonics are not orthogonal to each other when the study area is limited to a part of the sphere, and this allows some coefficients to be estimated on the basis of the mass re-distribution in the study area synthesized from the remaining coefficients. C_{10}^{ocean}, C_{11}^{ocean}, S_{11}^{ocean} and C_{20}^{ocean} are calculated from an independent (ocean) model. Hence, the difference between the two should only be attributed to the lack of degree-1 and C_{20} coefficients in the GRACE data, which results in an imperfect synthesis of the mass re-distribution over the ocean area.

The procedure is somewhat similar to the restoration of the integration constant when the value of the primitive function at a certain point is known. Since the number of unknown coefficients is four, knowing the ocean mass variations at just four properly chosen data points is sufficient to find the unknown coefficients. In practice, more data points are required to make the estimation accurate and stable. Nevertheless, the ocean function $\vartheta(\theta,\phi)$ does not have to include the whole ocean: particularly noisy regions can be excluded.

4.2.2. Input Data

Here, we discuss the input for the GRACE-OBP method in general terms. Specific input data sets will be described later.

According to Eqs. (4.3-4.5), two data sets are needed to estimate the four unknown coefficients: (i) a set of mass coefficients representing the global mass re-distribution at the Earth's surface and (ii) the oceanic component of the four un-

known coefficients predicted in the CF frame. The mass coefficients are obtained from the GRACE level-2 data (labeled as GSM). The GSM coefficients are reduced for signals due to mass redistribution in the atmosphere and ocean for which purpose the Atmosphere and Ocean De-aliasing level-1B (AOD1B) product (Flechtner and Dobslaw, 2013) is used to clean raw GRACE data from the corresponding signals. In order to use these coefficients in the GRACE-OBP method, one should also clean the GSM coefficients from signals due to the solid Earth (e.g., Glacial Isostatic Adjustment (GIA), mega-thrust earthquakes) by applying Eq. (4.1). The signals from the atmosphere and ocean (described by GAD product) should also be removed from the oceanic degree-1 coefficients used in Eq. (4.3) to keep them compatible with vector G (Swenson et al., 2008; Sun et al., 2016a).

Ideally, the residual oceanic degree-1 coefficients ($C_{1m}^{ocean} - G_{1mC}$, $S_{11}^{ocean} - G_{11S}$) should only reflect the signals not modeled by the OBP models, e.g., the mass exchange between ocean and land. The accurate estimation of ocean-land mass exchange is a delicate issue due to the fact that most ocean models, including the Ocean Model for Circulation and Tides (OMCT) (Thomas, 2002), which is used to produce the AOD1B, conserve the total volume of the ocean (Boussinesq approximation). This assumption results in artificial changes in the total mass of the ocean. The mean ocean mass is then removed (by adding or removing a uniform layer of water to the ocean) to conserve the total ocean mass. As a result, the ocean model can only predict internal mass re-distribution.

Variations in the total ocean mass can be taken into account by integrating the GSM-based (i.e., GRACE-observed) mass anomalies over the oceans. Then, the corresponding oceanic coefficients are estimated by assuming a certain spatial distribution (eustatic or fingerprints) of this mass. Note that variations derived from the GSM product are in the CM frame and, in our case, lack the C_{20} coefficient. To restore the missing four coefficients, it is possible to make use of an iterative approach. The four coefficients computed by means of the GRACE-OBP method are used to complement the GSM product at the next iteration. Starting from an initial guess where those coefficients are null, the estimation of the total ocean mass variation usually converges within a few iterations.

4.3. Simulation of GRACE Solutions

4.3.1. Error-free GSM Coefficients

The error-free GSM coefficients are constructed using the updated ESA Earth System Model (ESM) (Dobslaw et al., 2015). The updated ESM employs state-of-the-art geophysical models to simulate gravity field variations related to five components of the Earth system: atmosphere (A), ocean (O), terrestrial water (H), continental ice sheets (I) and the solid Earth (S). In our simulation, we only deal with the first four components, which are related to atmosphere and water mass redistribution

at the Earth surface. In other words, we assume that the solid Earth signal can be completely removed from GRACE data by means of independent models, though it is not exactly the case when dealing with real data.

The atmosphere component is based on the latest re-analysis from ECMWF, ERA-Interim (Dee et al., 2011). Terrestrial water storage variations are based on Land Surface Discharge Model (LSDM) (Dill, 2008). The cryospheric component is constructed using the surface mass balance predictions from RACMO (Ettema et al., 2009) and a simple linear ice discharge model developed by Gruber et al. (2011) when modeling the original ESM. The oceanic part is generated by summing up contributions from OMCT, meso-scale variability from MPIOM ocean model (Storch et al., 2012) and a uniform layer of water used to conserve the mass in the Earth system.

The ESM model covers a 12-year period from 1995 to 2006 with a temporal resolution of 6 hours and a spatial resolution of about 100 km in terms of half-wavelengths (complete to spherical harmonic degree 180). In addition, the unperturbed de-aliasing model named DEAL is provided (Dobslaw et al., 2016). DEAL is different from the sum of A and O, as it ignores the sea-level variability due to land-ocean water exchange and the small-scale ocean variability, which are also omitted in current AOD1B product. Along with the DEAL product, AOerr files are also delivered. These files contain a realization of errors in A and O components. These errors need to be added to DEAL to arrive at a perturbed model equivalent to the AOD1B (Dobslaw et al., 2016).

The above mentioned synthetic Earth is our study object. The “error-free” GSM coefficients are then simulated by subtracting the DEAL product from the synthetic Earth model. (Notice that these coefficients are strictly speaking not error-free because the DEAL product lacks some signals that are present in the A and O components.) To match the temporal resolution of the real GRACE data, monthly averages of the simulated GSM coefficients are calculated.

It is worth noting that mass conservation is enforced in ESM by adding or removing a uniform layer of water over the oceans to balance variations in the total mass of all the components. In reality, the water that represents mass exchange between ocean and land does not spread uniformly over oceans because the distribution of the ocean water is subjected to self-attraction and loading (SAL) effects (Gordeev et al., 1977). In order to make our synthetic model closer to the real Earth, we modify the updated ESM model such that the water distributes over the oceans according to the sea level equation (Farrell and Clark, 1976; Tamisiea et al., 2010). We expect SAL effects to have a large impact on water re-distribution (Clarke et al., 2005).

4.3.2. Simulation of GSM Errors

To generate realistic GSM coefficients, one needs to simulate the errors that are present in real GRACE data. In this study, we consider two error sources: (i) errors in the GAC product, and (ii) errors in the level-2 GRACE data (random errors). The GAC errors are the errors in monthly averages of the AOD1B product. They are mimicked by the errors provided in the AOerr file after we compute their monthly averages. The GRACE random errors, however, have multiple sources, such as uncertainties of onboard sensors, deficiencies in orbit determination, as well as errors in background geophysical models (including the AOD1B product) at short time scales. An extended discussion of sources of noise in GRACE data can be found in, e.g., (Ditmar et al., 2011). Random errors in GRACE level-2 data are different from month to month, which can be explained among others by variations in the orbit groundtrack pattern (Wagner et al., 2006). We simulate those errors $\mathbf{r}$ on the basis of the error variance-covariance matrices $\mathbf{C}$ of GRACE Stokes coefficients as follows.

$$\mathbf{r} = \mathbf{L}\mathbf{x}, \tag{4.6}$$

where the vector $\mathbf{x}$ contains normally distributed uncorrelated random numbers with zero mean and unit variance. $\mathbf{L}$ is the lower triangle matrix obtained by the Cholesky decomposition of the error variance-covariance matrix $\mathbf{C}$ ($\mathbf{C} = \mathbf{L}\mathbf{L}^{\mathbf{T}}$). In our study, we use the matrices $\mathbf{C}$ of the CSR RL05 GRACE solutions, which have been released since recently (ftp://ftp.csr.utexas.edu/outgoing/grace/). The simulated random errors for a particular month form a set of Stokes coefficients complete to the maximum degree of the error variance-covariance matrix, which is 96. For the sake of consistency, we simulate error-free GSM coefficients also to degree 96. We simulate GRACE errors for a period of approximately 12 years using the error covariance matrices from 2003 to 2014. Note that missing months in the time-series of real GRACE data are not included. Then the time-tags of error realizations are shifted by 8 years backward to match the updated ESM time interval (1995 - 2006). In Fig. 4.1 we show the simulated random errors in level-2 GRACE data for June 2006 in terms of equivalent water heights. The dominant error patterns are north-south-oriented stripes in the spatial domain, which are similar to those in real level-2 GRACE data. They can be largely suppressed by appropriate filtering (e.g. Klees et al., 2008; Kusche et al., 2009). However, in our simulation, we use these errors as they are because they largely cancel out as we integrate mass anomalies over a sufficiently large area. Using a filtered solution as input carries the risk of introducing non-negligible biases into low-frequency gravity signals.

Finally, we add the simulated GAC and random errors to the error-free GSM coefficients from the ESM to obtain the realistically perturbed coefficients, which are used as input in the further simulations. We generated 100 realisations of random errors and thus have 100 sets of simulated noisy GSM coefficients.

According to Eq. (4.3), the degree-1 and C_{20} estimates are affected by errors in

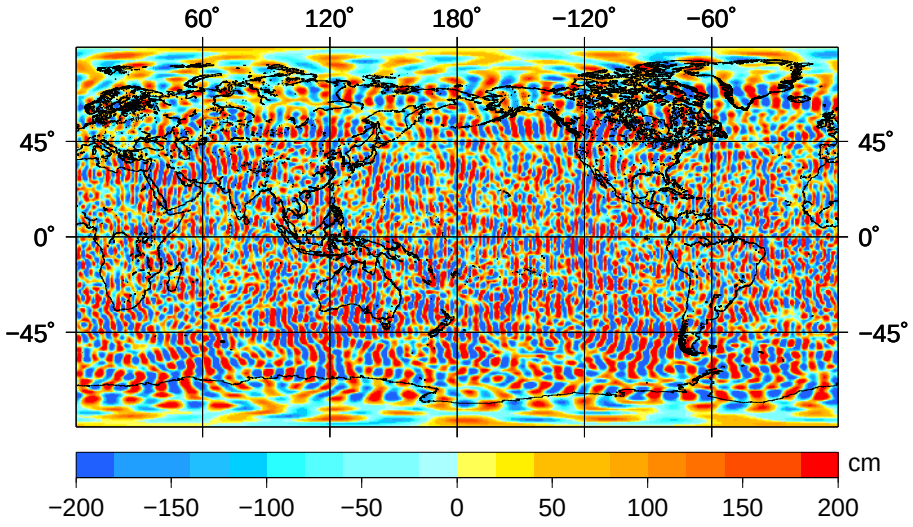

Figure 4.1: Synthesized GRACE random errors of June 2006 in terms of equivalent water heights.

both GSM coefficients and oceanic degree-1 and C_{20} coefficients. Here, we assume that the four oceanic coefficients are error-free and try to quantify only the impact of errors in GSM coefficients. We will address the impact of errors in the four input oceanic coefficients in Sect. 4.6.3.

4.4. Implementation Details

Apart from the input GSM coefficients and geophysical models, the solution of Eq. (4.3) is largely dependent on three implementation details: (i) the truncation degree of the GSM coefficients, (ii) the ocean function that partitions the Earth's surface into ocean and land and (iii) whether or not considering SAL effects when distributing ocean water.

We will have to find the truncation degree that is low enough to exclude the strong noise present at higher degrees, but still high enough to depict the large-scale mass re-distribution, which contributes significantly to the solutions.

The ocean function is responsible for selecting ocean grid points that are used to constrain the solution. Due to the limited resolution of GRACE monthly gravity field models, strong continental signals leak into ocean areas, so that an ocean function using the exact ocean-land boundaries will erroneously capture them as ocean signals. In order to reduce leakage from land into the oceans, we establish

a buffer zone by excluding points within a few hundred kilometers (up to 400 km) from the coast. A reasonable buffer width choice will allow us to use an ocean area not polluted by leakage from land and still large enough to ensure a stable solution.

In order to use the GRACE-OBP method, we need to define the four input oceanic coefficients (C_{10}^{ocean},...,C_{20}^{ocean}, see Eq. 4.3). As explained in section 4.2.2, these coefficients should only reflect the mass variations over ocean areas resulting from the water exchange between the continents and the oceans. After fixing the truncation degree of the GSM coefficients and the width of the buffer zone, the estimated total water exchange is also fixed. However, the solution is still affected by how water distributes over the oceans. Here, we consider two scenarios: (i) ignoring the SAL effects, so that water redistributes uniformly over oceans as in Swenson et al. (2008); the resulting ocean height change is known as barystatic (also called eustatic) sea level variation; (ii) taking into account SAL effects by computing the resulting fingerprints (Mitrovica et al., 2001) using the sea level equation.

In the following section, we analyze the effect of different choices of the implementation details. We discuss degree-1 and C_{20} coefficients separately.

4.5. Results of Numerical Experiments

In the numerical experiments, we estimate degree-1 and C_{20} time-series based on different combinations of the implementation parameters. The truncation degrees tested for the input "GRACE" solutions vary from 10 to 96 with a one-degree step. We show results for degrees 10 to 70 because solutions based on higher truncation degrees are in all cases too noisy due to large errors in high-degree coefficients. For each truncation degree, we test buffer widths from 0 to 400 km with a 100-km increment. For a particular combination of truncation degree and buffer zone width, we consider water distributions with and without taking SAL effects into account. Different degree-1 and C_{20} time-series ($T_{C_{10}}$, $T_{C_{11}}$, $T_{S_{11}}$ and $T_{C_{20}}$) corresponding to specific parameter combinations are obtained. Amplitude (T^{amp}), phase (T^{pha}) and linear trend (T^{trnd}) of the annual signal are estimated. Note that T^{amp} and T^{pha} are defined by approximating the annual cycle with the expression $T^{\text{amp}}\cos(\omega(t-t_0)-T^{\text{pha}})$, where ω is equal to 2π rad/yr and t_0 refers to January 1 of a particular year.

The resulting degree-1 and C_{20} time-series vary significantly for different synthetic GSM solutions reflecting different error realisations, which means that results based on just one set of GSM coefficients are not representative. Therefore, we show results based on all 100 sets of simulated GSM solutions. That is, for each combination of implementation parameters, we obtain 100 estimates of annual amplitude, phase and linear trend. Then, we show the mean value of the 100 estimates and use the corresponding standard deviation as a measure of uncertainties.

4.5.1. Annual Variations of Geocenter Motion

In Fig. 4.2, we show mean annual amplitude estimates of degree-1 time-series and their standard deviations. The annual amplitude estimates are sensitive to all three implementation parameters. With a truncation at around degree 45, we notice that applying a 200-km buffer zone increases the amplitude estimates of C_{10} and C_{11} by about 40 % and 10 %, respectively, compared to the solutions using no buffer zone (panels a and b). A further 25 % increase is found for both coefficients after using the realistic exchanging water distribution (panels d and e). In contrast, accounting for SAL effects and using a buffer zone have contradicting effects on the estimated amplitude of S_{11} time-series. Increasing the buffer tends to reduce further the already underestimated annual amplitude (panel c). Considering SAL effects, on the other hand, increases the estimates, so that the resulting amplitude is close to the synthetic truth (panel f).

Generally speaking, the figure shows that without taking into account the SAL effects in the data processing procedure, one cannot retrieve the true amplitude, no matter how the truncation degree and buffer width are chosen (panels a, b, c). However, by considering only the SAL effects without properly choosing the buffer zone width (e.g., using zero buffer width), one still cannot match the true amplitude (panels d, e, f). Note that the results based on the error-free GSM solutions are not shown because they are very close to the mean amplitudes. This is because the monthly averages of the AOD1B errors are negligible compared to GRACE random errors, as will be shown below. Therefore, taking the mean of 100 noisy realizations reduces the noise level by approximately a factor of 10 ($\sqrt{100}$). Best amplitude estimates are obtained after accounting for SAL effects and applying a buffer zone wider than 100 km (200 - 400 km). With these two implementation parameters chosen, the truncation degree becomes a less decisive factor, and a broad range of values (from 30 to 60) allows for estimating the amplitude accurately. Truncation degree higher than 60 clearly results in an increased uncertainty because of large errors in the high-degree coefficients.

Similar conclusions can be drawn for the C_{20} coefficient, as well as for the phases of annual variations and for the linear trends. In the following figures, we limit ourselves to presenting solutions using 0-km buffer width and ignoring SAL effects to show how the results look like if the original methodology of Swenson et al. (2008) is reproduced. In addition, we show solutions based on a 200-km buffer zone with and without considering SAL effects to illustrate the impact of a properly chosen buffer zone and considering SAL effects.

In Fig. 4.3, we show the annual phase estimates for degree-1 coefficients. For all three coefficients, a good estimation of the phase can be obtained by accounting for the SAL effects and using the buffer width of 200 km. The buffer zone width does not play a critical role here as the use of a 200-km buffer zone barely alters the phase estimates. Considering SAL effects has a much larger effect (up to 10 days), especially on C_{11} and S_{11}.

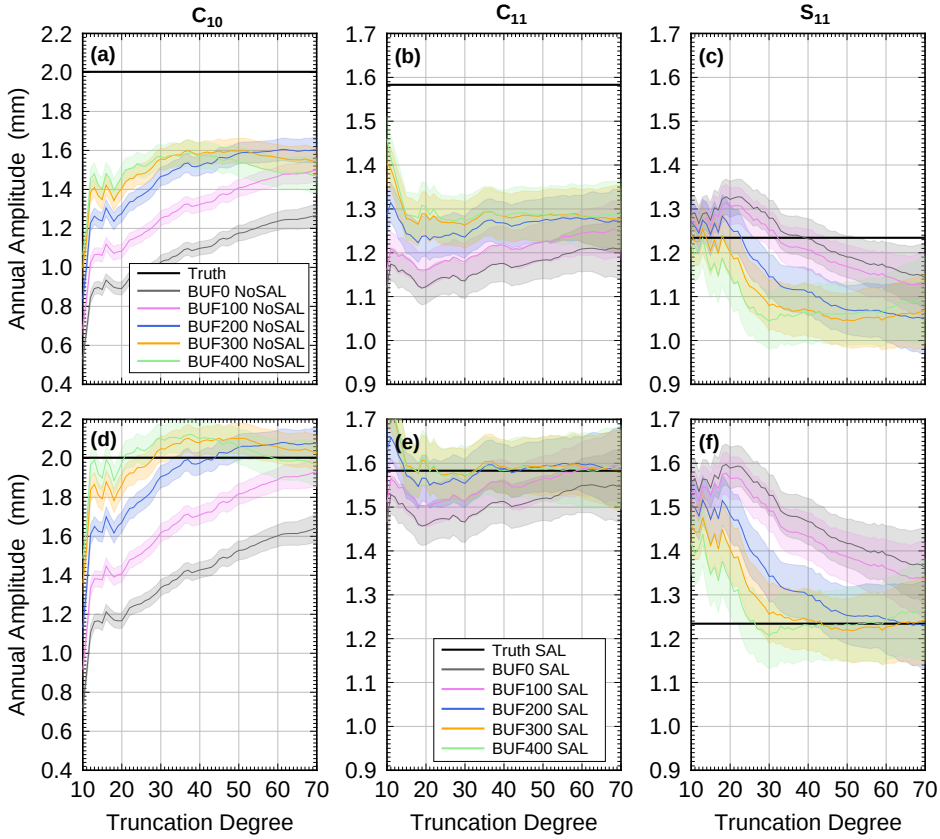

Figure 4.2: Results of simulated data processing: The mean annual amplitudes of the estimated GSM degree-1 time-series (in mm of geocenter motion) using different implementation parameters based on 100 sets of simulated GSM solutions. Their standard deviations are indicated by light colored bands. The true amplitudes are marked in all panels as black horizontal lines. In the upper panels (a, b, c), the amplitude estimates are based on the uniform exchanging water distribution (NoSAL). In the lower panels (d, e, f), we show results after distributing the exchanged water according to its gravitational fingerprints (SAL).

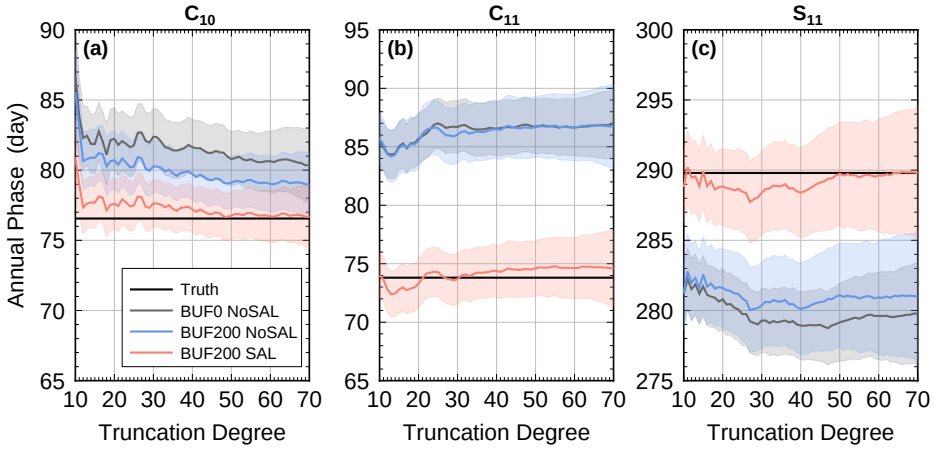

Figure 4.3: Results of simulated data processing: The mean annual phases of the estimated GSM degree-1 time-series inluding their standard deviation (indicated by light colored bands) using different implementation parameters based on 100 sets of simulated GSM solutions. The true phases are marked in all panels as black horizontal lines.

4.5.2. Linear Trend in Geocenter Motion

In Fig. 4.4, we show the effect of implementation details on estimates of a long-term linear trend. An accurate estimation of the trend in the C_{10} coefficient also requires the use of a buffer zone and the inclusion of SAL effects. In contrast, the impact of implementation details onto the estimation of C_{11} is minor. Finally, we see a better estimation of the S_{11} trend by using a buffer zone and taking into account SAL effects, but the uncertainties are relatively large, which implies the trend can still be over- or under-estimated by up to 25%.

From this test, it is tempting to conclude that the GRACE-OBP method is able to retrieve the correct linear trend, especially in the C_{10} and C_{11} coefficients, provided that buffer zone has been selected properly and SAL is taken into account. However, the synthetic model is not affected by the solid Earth contributions. Uncertainties in modelling those contributions might dominate in trend estimates when working with real data. We will discuss this issue further in Sect. 4.6.

4.5.3. C_{20} Variations

The GRACE-OBP method has been already used to determine J_2 variations (or equivalently C_{20} variations) in Chapter 3, where the results are validated against esti-

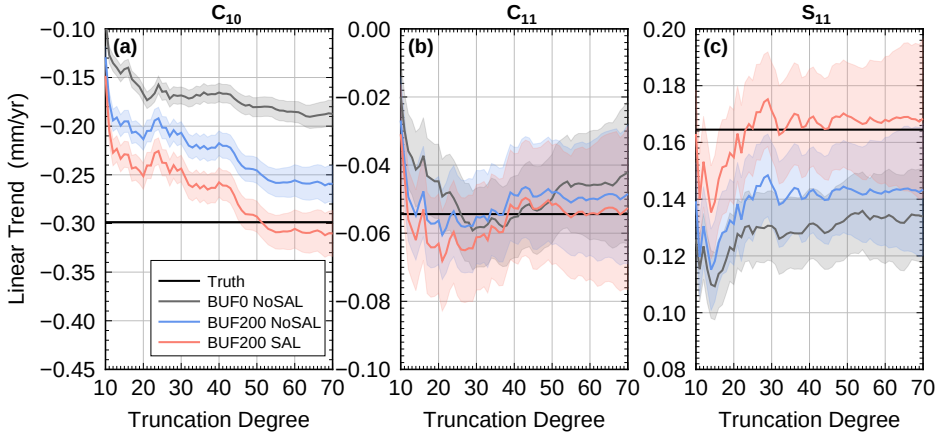

Figure 4.4: Same as Fig. 4.3, but for linear trend estimates.

mates from SLR over approximately the same interval as in our study. The optimal strategy found in that study consisted of using GRACE monthly solutions complete to spherical harmonic degree 60 and filtered by means of the DDK4 filter (Kusche et al., 2009), in combination with a buffer width of 150 km, and accounting for SAL effects. However, a specific SLR solution (Cheng et al., 2013a) may not represent the truth, and that strategy may offer a biased parameter choice. Here we make use of the synthetic model for an independent validation of the GRACE-OBP method as well as for choosing its optimal implementation. Results are shown in Fig. 4.5.

As far as the amplitude of the annual signal is concerned, the use of a buffer zone of 200 km has a relatively small effect of increasing the estimated value, which remains 50% smaller than the truth (Fig. 4.5a). Accounting for SAL effects (Fig. 4.5b) doubles the amplitude and allows us to recover the truth almost exactly (in combination with a 200 km buffer and a truncation degree between 30 and 50). It is worth noting that SAL effects are consistently computed for each choice of the buffer zone, which means those effects are limited to the ocean areas excluding the applied buffer zone. The phase of the annual signal, on the other hand, is fairly independent from the buffer size and SAL effects and varies within not more than one week for truncation degree between 30 and 50 (Fig. 4.5b).

The linear trend estimate turns out to be highly dependent on all three implementation details. Including a 200 km buffer zone and accounting for SAL effects have again a large positive impact especially onto the estimated C_{10} and C_{20} coefficients. At the same time, it is also important to choose a truncation at around degree 45 to obtain the accurate estimates. When using a truncation lower than

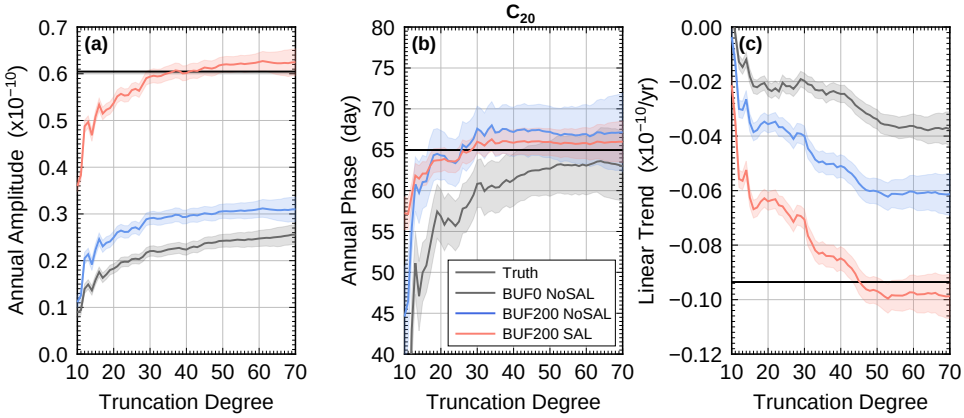

Figure 4.5: Similar to Fig. 4.3, but for annual amplitude, annual phase and linear trend of the C_{20} coefficient.

degree 40, the trend estimates can differ with the truth by over 20%.

4.5.4. Optimal Implementation Parameter Setup

In this section, we apply a formal criterion to identify the optimal parameter setup for estimating degree-1 and C_{20} coefficients simultaneously with the GRACE-OBP method. We define the quality indicator for annual variations (Q^{ann}) and linear trend (Q^{trnd}) separately as follows:

$$Q^{\text{ann}} = \sum_{\text{cf}=C_{10}}^{C_{20}} \frac{1}{n} \sum_{i=1}^{n} \{(T_{\text{cf},i}^{\text{amp}} sin(T_{cf,i}^{\text{pha}}) - T_{cf}^{(t)\text{amp}} sin(T_{\text{cf}}^{(t)\text{pha}})^2 + (T_{\text{cf},i}^{\text{amp}} cos(T_{\text{cf},i}^{\text{pha}}) - T_{\text{cf},i}^{(t)\text{amp}} cos(T_{\text{cf},i}^{(t)\text{pha}})^2\}, \tag{4.7}$$

and

$$Q^{\text{trnd}} = \sum_{\text{cf}=C_{10}}^{C_{20}} \frac{1}{n} \sum_{i=1}^{n} \{(T_{\text{cf},i}^{\text{trnd}} - T_{\text{cf}}^{(t)\text{trnd}})^2\}, \tag{4.8}$$

where T_{cf} represents the time-series of the coefficient indicated by index cf, and the index of cf runs over the four estimated coefficients, namely C_{10}, C_{11}, S_{11} and C_{20}. Note that these coefficients are scaled to describe mass changes in terms of

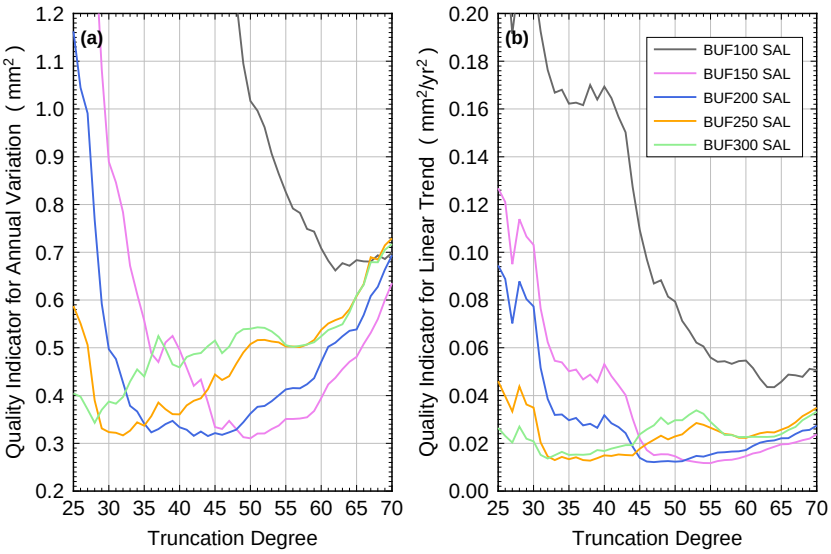

Figure 4.6: Results of simulated data processing: The quality indicator for different combinations of implementation parameters. We show the quality of estimated annual variations (a) and linear trends (b).

equivalent water height (Eq. (4.1) and (4.2)). Subscript i indicates that the result is based on the ith realization of noisy GSM coefficients; n is the number of simulated GSM solutions, which equals 100. Superscripts amp, pha and $trnd$ represent the annual amplitude, phase and trend of the corresponding time-series, respectively; superscript (t) refers to the synthetic truth. We are looking for the parameter settings that yield the smallest Q^{ann} and Q^{trnd} value.

In Fig. 4.6, we show the quality of selected parameter setups. The quality of the estimated annual variations and linear trends of the four coefficients is much worse if SAL effects are not taken into account. Therefore, that option is not addressed in the figure. Clearly, the best results are obtained from the buffer width from 150 to 250 km in combination with a proper truncation. Ultimately, we select the option "T45 BUF200 SAL", which uses a truncation at degree 45, buffer width of 200 km and accounting for SAL effects, as the recommended parameter setup for estimating both annual variations and linear trend.

4.5.5. The Impact of GSM Errors

It is clear that both random errors in GRACE data and errors in the monthly averages of atmosphere and OBP (GAC) contribute to the uncertainties in the obtained

Table 4.1: Results of simulated data processing: RMS errors (RMS values of the difference between obtained time-series and the synthetic truth) of the degree-1 and C_{20} solutions due to atmosphere and OBP errors and GRACE random errors. We also show the impact of RMS errors on the estimation of annual variations. RMS errors as well as errors in annual amplitude of degree-1 solutions are reported in terms of geocenter motion.

		C_{10} (mm)	C_{11} (mm)	S_{11} (mm)	C_{20} (10^{-11})
RMS error	GAC	0.04	0.02	0.02	0.01
	GRACE	0.49	0.50	0.56	0.13
Ann Var error	Amp	0.1	0.1	0.1	0.2
	Pha (day)	2	2	3	2

GSM coefficients. It is interesting to quantify the relative contributions of these two error sources to the error budget of the obtained estimates of degree-1 and C_{20} coefficients. Here, after setting the implementation parameters to the identified optimal setup, we consider: (i) GSM coefficients only subject to GAC errors, and (ii) those only subject to GRACE random errors. Both are compared with results based on the error-free GSM coefficients.

As shown in Tab. 4.1, the GAC errors induced uncertainty is less than 10% of that due to GRACE random errors for all four coefficients. Compared to the impact of GRACE random errors, the impact of GAC errors is negligible. Therefore, it is enough to just quantify the impact of GRACE random errors (with 100 realizations) on the estimates of annual variations (the impact of GAC errors cannot be shown realistically since we have only one realization for that type of error). These findings are likely applicable to real data as well, since the provided AOerr represent errors in AOD1B product used in the GRACE data processing (Dobslaw et al., 2016).

4.6. Results Based on Real GRACE Data

In this section, we present degree-1 and C_{20} solutions based on the GSM coefficients provided by CSR RL05 (complete to degree 96) covering a 12-year period (from August 2002 to June 2014). The pole tide (mainly affecting the C_{21} and S_{21} coefficients) has been corrected for according to Wahr et al. (2015). Unlike the synthetic input, real GSM coefficients are not free of time-variable signals from the interior of the Earth. Here, we only attempt to remove the prominent signals caused by GIA. Since the use of a GIA model does not affect annual variations, we postpone the GIA discussion until we show the linear trend estimates.

4.6.1. Geocenter Motion

Even though we have already identified the optimal parameter set-up, we find it more informative to produce degree-1 solutions for different combinations of implementation details as it was done in the numerical experiments. Since the results are now based on just one set of real GSM solutions, the uncertainty ranges are computed based on the least-squares residuals.

When looking at the estimated annual amplitudes (Fig. 4.7), we see that the effects of changing the buffer size and including SAL effects are extremely similar to the synthetic case (Fig. 4.2). Consequently, we believe that the recommended parameter setup based on the numerical experiments can also be applied to real data, even though the synthetic Earth employed in the numerical studies may not model the Earth system perfectly.

The impact of the implementation parameters on the annual phase (Fig. 4.8) is similar to the synthetic case (Fig. 4.3) only for C_{11}, while C_{10} and S_{11} show a larger dependence on the buffer size and a smaller dependence on taking SAL effects into account. Nonetheless, the qualitative agreement between the results obtained with synthetic and real data still supports the use of a buffer and accounting for SAL effects.

So far, we have discussed only degree-1 time-series without the contribution of atmospheric and oceanic processes (GSM-like coefficients). In Tab. 4.2, we show the results in terms of full geocenter motion, i.e. after restoring the degree-1 coefficients of the GAC products. In order to quantify the GAC-modeled atmosphere and ocean contribution, we additionally list the results for GSM-like coefficients as a reference. The amplitude and phase of C_{10} are changed after restoring the GAC product insignificantly: by less than 1% and by about half a month, respectively. In contrast, C_{11} and S_{11} are largely affected. The GAC products change their phase estimates by about a month and account for about 30% and 40% of the total amplitude of C_{11} and S_{11}, respectively. Tab. 4.2 also shows the solutions from the GRACE TELLUS website that are based on the methodology by Swenson et al. (2008) (`ftp://podaac.jpl.nasa.gov/allData/tellus/L2/degree_1/`, downloaded in December 2015, GAC product is restored), as well as other solutions from recent literature. Compared to the results based on (Swenson et al., 2008), our estimates have a considerably larger annual amplitude for the C_{10} and C_{11} coefficients, respectively by about 50% and 20%. Since the same GAC product is restored to both solutions, the increase can only be caused by a different setup of the implementation parameters. According to Fig. 7, 54% of the increase in C_{10} amplitude is due to the use of a 200-km ocean buffer, and the rest is due to the consideration of SAL effects. The increase in C_{11} amplitude, on the other hand, should only be attributed to SAL effects. The new estimates compare much better with the annual signals detected by other techniques (Tab. 4.2). Full degree-1 time-series based on alternative GRACE monthly solutions, such as JPL RL05 (Watkins, 2012) and GFZ RL05a (Dahle et al., 2013), provide estimates very close to ones based on

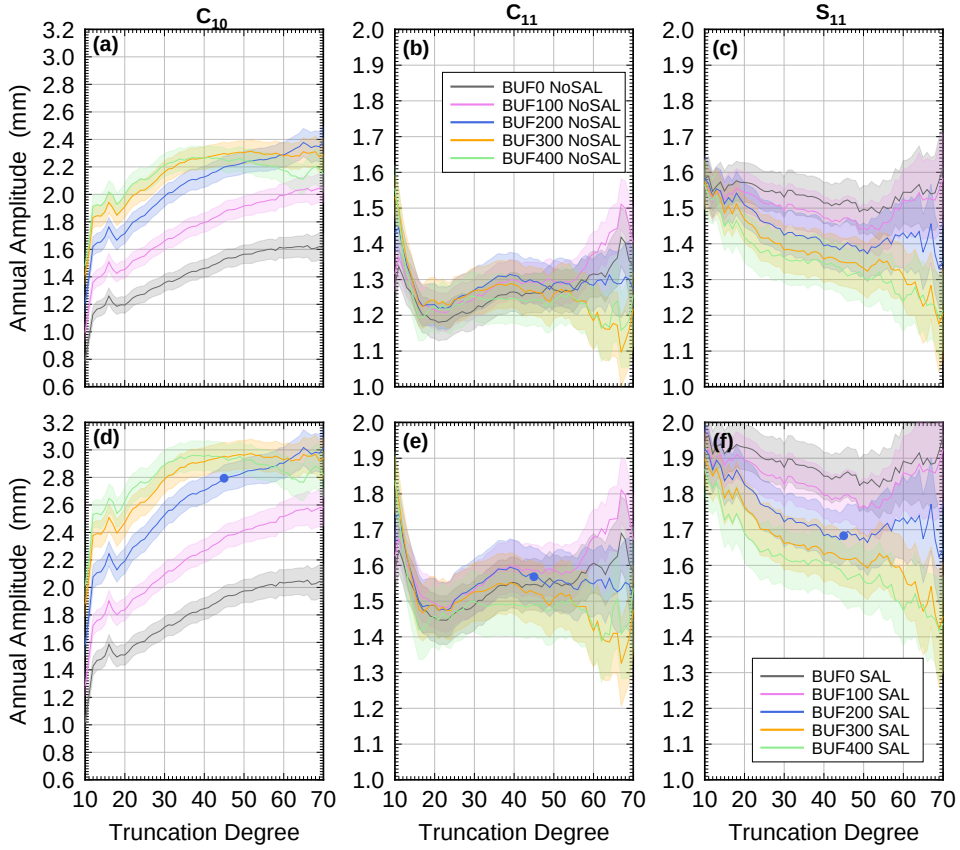

Figure 4.7: Results of real data processing: The annual amplitudes of the estimated GSM degree-1 time-series (in mm of geocenter motion) using different implementation parameters based on GRACE data (CSR RL05). The uncertainty ranges are estimated from least squares fitting error. The values obtained with the recommended data processing set-up are marked with blue dots in panel d, e and f.

Table 4.2: Results of simulated data processing: Estimated amplitudes and phases of the annual geocenter motion.The contribution of atmosphere and ocean (GAC) is restored. As a reference, the row with leading 'GSM' represents the optimal GSM-like geocenter motion based on CSR RL05.The top part of the table presents results of this study, while lower part show results from other studies. T45 means a truncation at degree-45, BUFxxx denotes the buffer width of xxx km; BUF0 indicates the absence of a buffer zone. SAL indicates that the SAL effects have been taken into consideration. The same nomenclature is also used in other tables in this study. Solutions labeled with 'GFZ' and 'JPL' are based on GSM coefficients from GFZ RL05a and JPL RL05. OMCT and ECCO indicate the OBP model adopted in the solution.

	C_{10}		C_{11}		S_{11}		
	Amp (mm)	Pha (day)	Amp (mm)	Pha (day)	Amp (mm)	Pha (day)	Time span (year)
GSM T45 BUF200 SAL OMCT	2.8 ± 0.1	85 ± 2	1.6 ± 0.1	85 ± 3	1.7 ± 0.1	302 ± 3	2002.6 - 2014.5
GSM T45 BUF200 SAL ECCO_Polar_zero	2.6 ± 0.1	79 ± 2	1.6 ± 0.1	75 ± 3	1.8 ± 0.1	309 ± 2	2002.6 - 2014.5
GSM T45 BUF200 SAL ECCO_Polar_OMCT	2.7 ± 0.1	82 ± 2	1.6 ± 0.1	82 ± 3	1.7 ± 0.1	306 ± 2	2002.6 - 2014.5
CSR T45 BUF200 SAL OMCT	2.9 ± 0.2	69 ± 4	2.3 ± 0.1	52 ± 3	2.8 ± 0.1	327 ± 2	2002.6 - 2014.5
CSR T45 BUF200 SAL ECCO_Polar_zero	2.5 ± 0.2	58 ± 4	2.0 ± 0.1	53 ± 3	3.0 ± 0.1	333 ± 2	2002.6 - 2014.5
CSR T45 BUF200 SAL ECCO_Polar_OMCT	2.7 ± 0.2	59 ± 4	2.0 ± 0.1	54 ± 3	3.0 ± 0.1	334 ± 2	2002.6 - 2014.5
GFZ T45 BUF200 SAL OMCT	3.0 ± 0.2	69 ± 4	2.3 ± 0.1	54 ± 3	2.8 ± 0.1	326 ± 2	2002.6 - 2014.5
JPL T45 BUF200 SAL OMCT	2.9 ± 0.2	72 ± 4	2.2 ± 0.1	55 ± 4	2.7 ± 0.1	328 ± 2	2002.6 - 2014.5
(Swenson et al., 2008)	1.9 ± 0.1	65 ± 4	1.9 ± 0.1	53 ± 3	2.5 ± 0.1	319 ± 2	2002.6 - 2014.5
SLR (Sośnica et al., 2013)	3.0 ± 0.3	-	2.75 ± 0.15	-	2.2 ± 0.1	-	2002.6 - 2014.5
SLR (Cheng et al., 2013b)	4.2 ± 0.3	33 ± 2	2.9 ± 0.4	49 ± 4	2.7 ± 0.1	324 ± 2	2002.6 - 2014.5
INV (Rietbroek et al., 2012b)	2.6	25	2.1	60	3.4	326	2003.0 - 2009.0
KAL-1 (Wu et al., 2015)	3.9 ± 0.1	21 ± 1	2.1 ± 0.1	45 ± 1	2.7 ± 0.1	321 ± 1	2002.3 - 2009.3
KAL-2 (Wu et al., 2015)	3.3 ± 0.1	22 ± 3	1.9 ± 0.1	54 ± 2	2.6 ± 0.1	322 ± 1	2002.3 - 2009.3
KAL-3 (Wu et al., 2015)	3.5 ± 0.1	19 ± 1	1.9 ± 0.1	52 ± 1	3.0 ± 0.1	337 ± 1	2002.3 - 2009.3

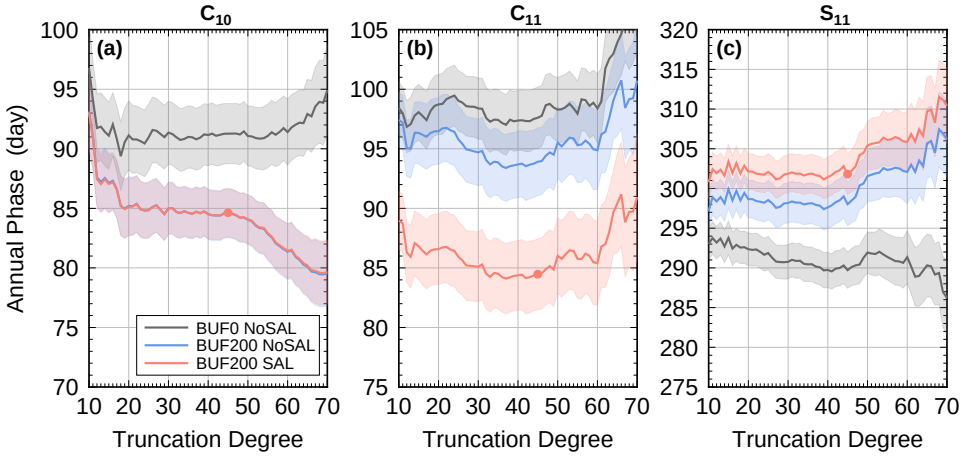

Figure 4.8: Results of real data processing: The annual phases of the estimated GSM degree-1 time-series using different implementation parameters. The uncertainty ranges are calculated based on least-squares fitting errors.

CSR RL05.

In Fig. 4.9, we plot the proposed degree-1 solution together with the solution by Swenson et al. (2008), as well as a selected SLR solution (Cheng et al., 2013b), linear trends being removed. The annual cycle is the most prominent feature in all solutions. Though our estimates of the amplitudes of the C_{10} and C_{11} coefficients are larger than the ones provided by (Swenson et al., 2008), the differences to SLR estimates (Cheng et al., 2013b) are still significant.

Since the GRACE-OBP methodology implies that mass transport takes place only at the Earth's surface, we subtracted GIA signals from the input GSM coefficients. In Tab. 4.3, we list linear trend estimates obtained with two GIA models and compare them with trend estimates from literature. GIA model ICE-5G_VM2 (A et al., 2012) is based on the ICE-5G ice history and a simplified version of mantle viscosity model VM2 (Peltier, 2004), and computed for a compressible Earth model. GIA model ICE-6G_VM5a is based on the ICE-6G ice history and the VM5a viscosity profile (Peltier et al., 2015). Differences between the surface mass trend estimates based on two GIA models suggests that uncertainties in GIA models play a important role in geocenter trend estimates. However, the optimal estimation of geocenter motion trend caused by surface mass transport, as well as of the full trend (which can be obtained by adding back the GIA-induced trend), are still under investigation and not discussed in this study.

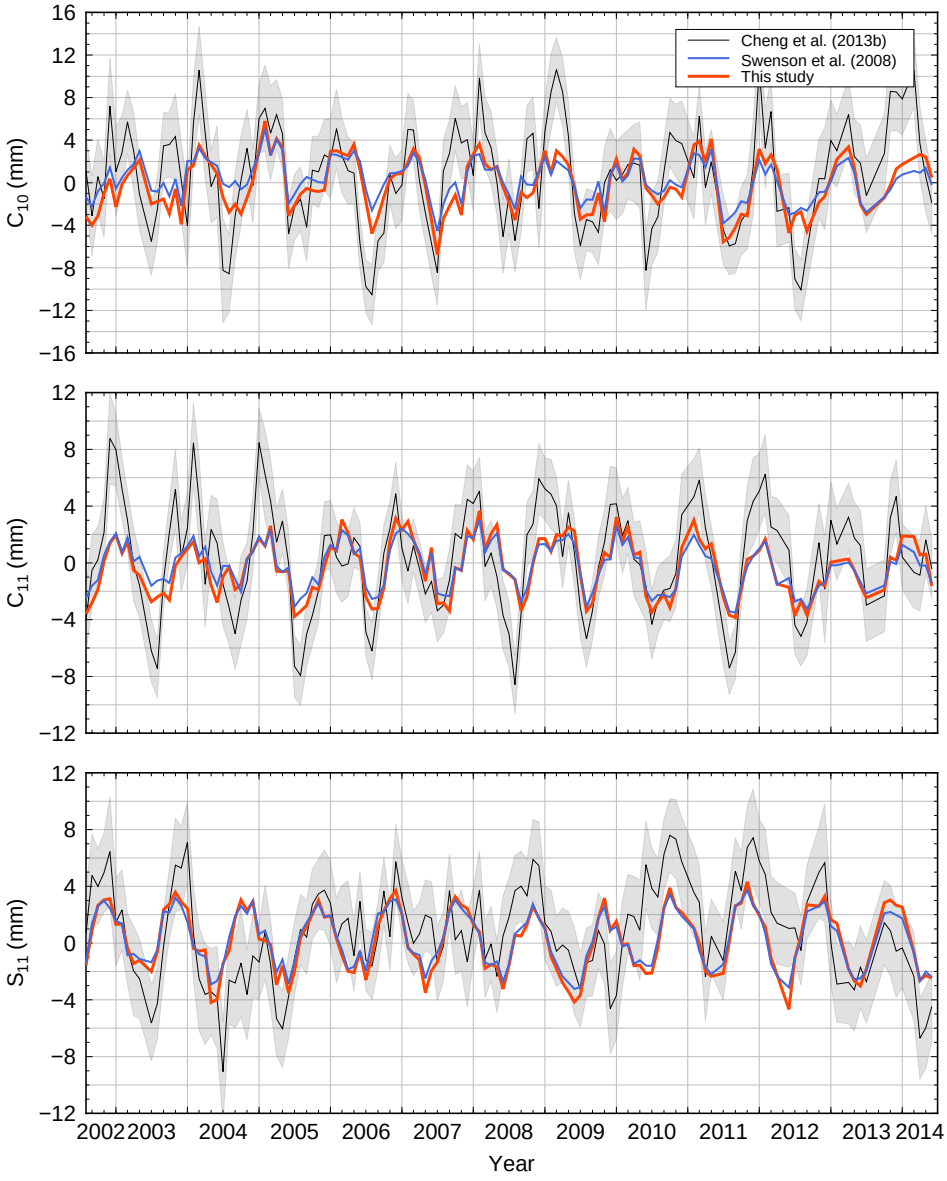

Figure 4.9: Results of real data processing: The degree-1 time-series based on the proposed implementation parameter setup after the restoration of the atmosphere and ocean signal using the GAC product, together with the solution based on Swenson et al. (2008) and an SLR solution (Cheng et al., 2013b). The uncertainties of the SLR solution are shown as gray bands.

Table 4.3: Results of real data processing: Geocenter motion trends due to surface mass transport estimated using different GIA models, based on solution CSR T45 BUF200 SAL OMCT. The contribution of atmosphere and ocean is restored. Results from literature are reported as well.

	C_{10}	C_{11}	S_{11}	Time span
	$(mm\,yr^{-1})$	$(mm\,yr^{-1})$	$(mm\,yr^{-1})$	(year)
ICE-5G_VM2	-0.21 ± 0.04	-0.03 ± 0.03	0.11 ± 0.02	2002.6 - 2014.5
ICE-6G_VM5a	-0.33 ± 0.04	-0.06 ± 0.03	0.07 ± 0.02	2002.6 - 2014.5
(Swenson et al., 2008)	-0.11 ± 0.03	-0.08 ± 0.02	-0.02 ± 0.02	2002.6 - 2014.5
Wu et al. (2010)	-0.16 ± 0.07	-0.10 ± 0.01	0.29 ± 0.05	2002.3 - 2009.0
Rietbroek et al. (2012a)	-0.37	-0.14	0.12	2003.0 - 2009.0

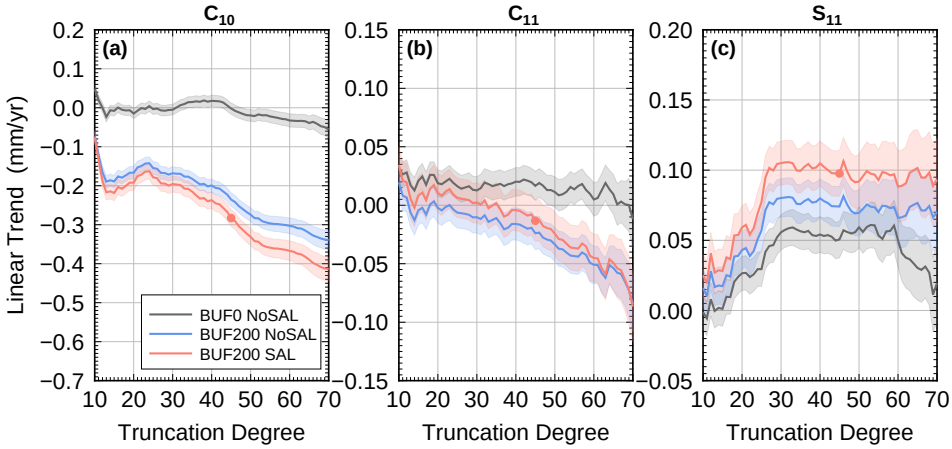

Figure 4.10: Same as Fig. 4.8 but for linear trend estimates.

In Fig. 4.10, we demonstrate that the linear trend estimates based on various combinations of implementation parameters also show a similar behavior, as compared to that observed in our numerical experiments. For example, the linear trend estimates in C_{10} are smaller for higher truncation degrees and more narrow buffer zones. Estimates in S_{11} increase for wider buffer zones while are relatively insensitive to truncation degrees larger than 30.

4.6.2. C_{20} Variations

Results for C_{20} variations based on real data are shown in Fig. 4.11.

As for the case of degree-1 coefficients, both the annual signal and the linear trend show a similar behaviour to the synthetic test, in terms of dependence on the truncation degree, as well as the impact of buffer width and SAL effects. Hence, we expect the best estimation of the annual amplitude to be obtained when using a 200-km wide buffer and accounting for SAL effects, where the latter is particularly important.

In Fig. 4.12 we show the detrended GSM-like C_{20} time series, supplemented by the SLR solution (GSM-like) by Cheng et al. (2013a) and the GRACE-OBP solution shown in Fig 3.1, which was optimised to match the SLR results. Note that the optimal GRACE-OBP solution from this study generally falls within the SLR uncertainty range, but is less volatile. However, the amplitude estimate over the whole time interval is considerably larger than the estimate from the SLR solution (Tab. 4.4).

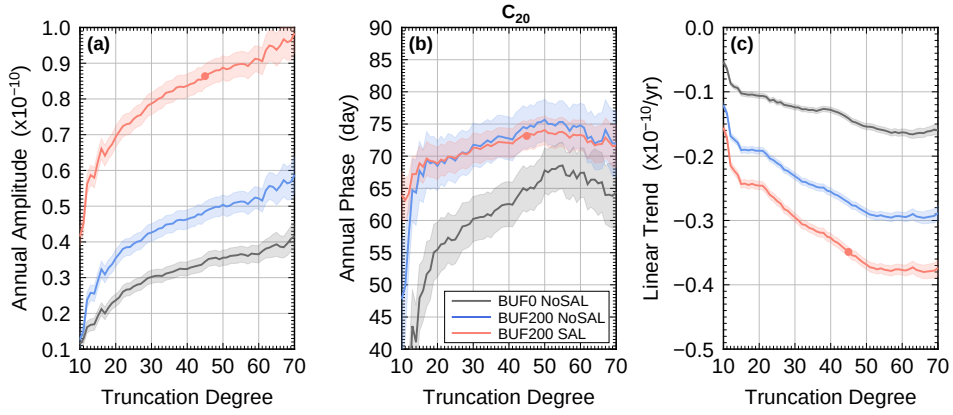

Figure 4.11: Same as Fig. 4.5, but derived from real GRACE data.

Comparisons show that the differences to the annual amplitude estimates of other SLR solutions (Lemoine et al., 2013; Sośnica et al., 2014) are even larger. Further investigation is needed to understand these discrepancies.

As far as the linear trend is concerned, the results shown in the right plot of Fig. 4.11 again support the use of the same implementation parameters as the synthetic test suggests. Statistics for selected solutions are shown in Tab. 4.5, where we have adopted the same GIA models as used for the degree-1 solutions. Note that to facilitate a comparison with other studies, we list $\dot{J}_2$ values. Also, since J_2 varies non-linearly, it is only meaningful to compare linear trends for approximately the same time span. Therefore, our results are only compared with several SLR solutions with approximately the same time interval. The full linear trend estimates from the GRACE-OBP approach supported with either GIA model are close to the estimate from the SLR solution by Sośnica et al. (2014), but about twice as large as those from the SLR solution by Cheng et al. (2013a). The full linear trend of the SLR solution by Lemoine et al. (2013) is relatively close to the GRACE-OBP solution based on the ICE-6G_VM5a model.

4.6.3. The Impact of Errors in the Oceanic Degree-1 and C_{20} Coefficients

Until now, we have analyzed the GRACE-OBP approach under the assumption that the oceanic degree-1 and C_{20} coefficients are error-free. In reality, the four oceanic coefficients will likely contain errors that could propagate into the final degree-1 and C_{20} solutions through the GRACE-OBP approach. Through analytical error

Table 4.4: Results of real data processing: Estimated annual amplitudes and phases of the C_{20} time-series. Amplitude and phase of the annual variations in all listed SLR solutions are estimated by ourselves. Results in the first two columns are free of atmosphere-ocean contributions (GSM-like). These contributions are restored in the results shown in the next two columns (Full).

	GSM-like		Full		
	Amp	Pha	Amp	Pha	Time span
	(10^{-11})	(10^{-11})	(10^{-11})	(10^{-11})	(year)
CSR T45 BUF200 SAL OMCT	8.6 ± 0.3	73 ± 2	16.1 ± 0.7	52 ± 3	2002.6 - 2014.5
CSR T45 BUF200 SAL ECCO_Polar_zero	8.0 ± 0.3	71 ± 2	12.8 ± 0.7	55 ± 3	2002.6 - 2014.5
CSR T45 BUF200 SAL ECCO_Polar_OMCT	8.2 ± 0.3	74 ± 2	13.8 ± 0.7	55 ± 3	2002.6 - 2014.5
GFZ T45 BUF200 SAL OMCT	8.5 ± 0.3	71 ± 2	16.1 ± 0.7	50 ± 3	2002.6 - 2014.5
JPL T45 BUF200 SAL OMCT	8.7 ± 0.3	74 ± 2	16.1 ± 0.7	52 ± 3	2002.6 - 2014.5
GRACE-OBP(Sun et al., 2016a)	6.8 ± 0.3	77 ± 2	-	-	2003.0 - 2013.4
SLR (Cheng et al., 2013b)	7.0 ± 0.4	81 ± 3	14.1 ± 0.7	53 ± 3	2002.6 - 2014.5
SLR (Lemoine et al., 2013)	6.0 ± 0.4	62 ± 3	14.0 ± 0.7	43 ± 3	2002.6 - 2014.5
SLR (Sośnica et al., 2014)	4.5 ± 0.5	88 ± 7	11.6 ± 0.8	49 ± 4	2002.6 - 2014.5

Table 4.5: Results of real data processing: Estimated linear trends from J_2 time-series based on CSR T45 BUF200 SAL OMCT solution and two different GIA models, as well as from the literature. SLR trends are estimated for the same time interval as considered in our study. The contribution of atmosphere and ocean has been restored in the GRACE surface mass estimates (Surface). The total GRACE-based trends are obtained as the sum of surface- and GIA-related trends.

	Surface	GIA	Total	Time span
	$(10^{-11} yr^{-1})$	$(10^{-11} yr^{-1})$	$(10^{-11} yr^{-1})$	(year)
ICE5G_VM2	7.7 ± 0.4	-3.2	4.5 ± 0.4	2002.6 - 2014.5
ICE6G_VM5a	7.3 ± 0.4	-3.5	3.8 ± 0.4	2002.6 - 2014.5
GRACE-OBP(Sun et al., 2016a)	7.4	-3.3	4.1 ± 0.2	2003.0 - 2013.4
SLR (Cheng et al., 2013b)	-	-	2.0 ± 0.3	2002.6 - 2014.5
SLR (Lemoine et al., 2013)	-	-	3.1 ± 0.4	2002.6 - 2014.5
SLR (Sośnica et al., 2014)	-	-	4.0 ± 0.4	2002.6 - 2014.5

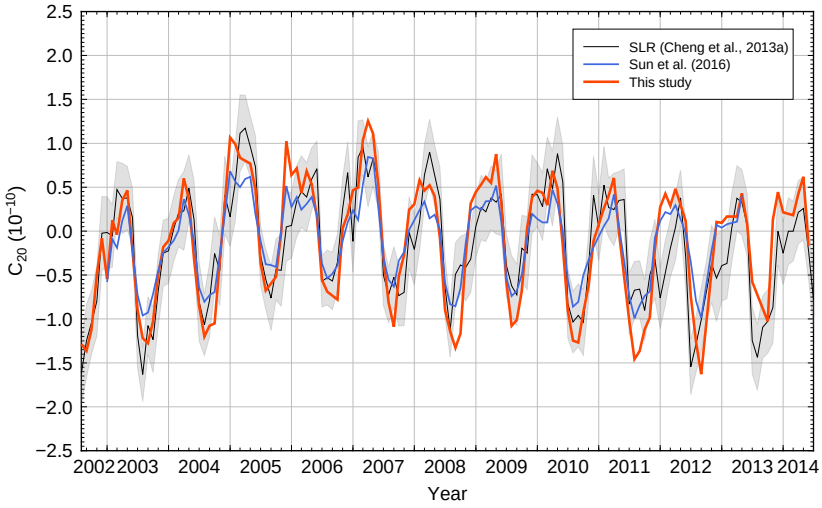

Figure 4.12: Results of real data processing: The C_{20} time-series based on the proposed implementation parameter setup together with the solution from Sun et al. (2016a) and an SLR solution (uncertainties are indicated by light gray band) (Cheng et al., 2013a). The contribution of atmosphere and ocean is not restored in the GRACE-OBP solutions, as the same contribution is removed from the SLR solution. A linear trend has been removed.

propagation based on Eq. (4.3), a 1-mm (equivalent water height) error in C_{10}^{ocean}, C_{11}^{ocean}, S_{11}^{ocean} and C_{20}^{ocean} propagates to about 1.8-, 1.4-, 1.6- and 1.9-mm error in the resulting C_{10}, C_{11}, S_{11} and C_{20} coefficients, respectively. It is difficult to synthesize realistic error realizations for low-degree oceanic coefficients as they may be contaminated by time-correlated errors. Therefore, we limit ourselves to comparing annual variations in degree-1 and C_{20} coefficients based on two alternative OBP models in order to show the potential impact of such errors.

That is, we repeat the computations presented above, having replaced the OMCT model with the ECCO model (Fukumori, 2002; Kim et al., 2007). The ECCO OBP field is from ECCO's Near-Real-Time Kalman filter estimate version kf080, which assimilates altimetry data as well as in-situ temperature profiles. The ECCO OBP fields are available in monthly averages, on $1^\circ \times 1^\circ$ grids covering oceans between $80^\circ S$ and $80^\circ N$ (http://grace.jpl.nasa.gov/data/get-data/ocean-bottom-pressure/). We fill the polar gaps in the ECCO OBP estimates in two ways: (i) with zeros (ECCO_Polar_zero) and (ii) with data points from OMCT OBP (ECCO_Polar_OMCT).

In Tab. 4.2 and Tab. 4.4, we show the amplitude and phase estimates of the annual variations for degree-1 and C_{20} coefficients based on different ECCO OBP models. The annual variations of all four coefficients are not significantly changed. For GSM-like degree-1 and C_{20} coefficients, the largest differences are seen when the

ECCO_Polar_zero model is used instead of OMCT. However, the annual amplitudes are only different within 10% and annual phases are differ by less than 10 days.

When considering full coefficients, the impact of using a different OBP model becomes larger. Again, the largest difference is seen between OMCT and ECCO_Polar_zero models. Note that using the ECCO_Polar_zero model is a sub-optimal choice, and the results based on such a model should not be compared directly with those based on OMCT model, which is global. Nevertheless, even in that case, the annual amplitudes of degree-1 coefficients are different within 15%. For annual phase estimate, the largest difference is 11 days. Annual amplitude of full C_{20} coefficient is about 20% smaller when the ECCO_Polar_zero is used. The annual phases of full C_{20} coefficients, on the other hand, agree within one sigma (3 days).

It is also important to realize that the optimal choice for the implementation parameter based on the numerical study ignores the errors in the oceanic degree-1 and C_{20} coefficients. Nevertheless, they are still valid in case of estimating annual variations, judging from the relatively small differences in those estimates when using different OBP models.

4.7. Discussion and Conclusions

Our simulation results suggest that the approach proposed by Swenson et al. (2008) is capable of accurately estimating geocenter and J_2 variations. However, the choice of implementation details is important. In particular, it is critical to take into account the spatial distribution of the exchanged water between land and oceans (SAL effects) and to make the proper partitioning into land and ocean. Extending the continent boundaries by means of a 200-km buffer zone produces the best results. Also, a truncation of the sets of input spherical harmonic coefficients influences the quality of the estimates. The optimal truncation degree is between 30 and 50. A lower truncation degree may lead to missing some mass redistribution at small spatial scales that still significantly contributes to geocenter motion and J_2 variations. A higher truncation degree increases the effect of errors at small spatial scales.

The optimal choice of the implementation details might be somewhat different for each of the four coefficients analysed, and for different quantities of interest: the amplitude/phase of annual variations or the linear trend. Nevertheless, we find it essential to identify a single optimal setup in order to ensure a consistency of the obtained estimates. The recommended setup consists of truncation at degree 45, a buffer width of 200 km, and accounting for SAL effects.

We have also shown that in real GRACE data processing, the dependence of the solution on the implementation details is similar to the synthetic case. Therefore, the optimal implementation setup discussed above is likely also suitable to deal with real data. The resulting time-series of geocenter motion and J_2 variations are expected to be significantly improved with respect to previous results based on the original methodology of Swenson et al. (2008). Notable differences are in the amplitude of the annual signal of GSM-like C_{10}, which is 50% larger than in (Swenson et al., 2008), and in the annual amplitude of full J_2, which is 15% larger than in (Cheng et al., 2013a).

When we restore the atmosphere-ocean contribution to arrive at the full coefficients, the annual amplitude of C_{10} is barely changed and the phase is shifted by only two weeks, which suggests that continental hydrological processes, changes in the cryosphere and total ocean mass variations are responsible for most of the seasonal variations in the Z-component of geocenter motion. In contrast, the annual amplitudes of C_{11} and S_{11} are increased by about 30% and 70%, respectively, which implies that atmosphere-ocean variations are largely driving seasonal variations in geocenter motion at the X- and Y-components. Also, J_2 variations are largely affected by the atmosphere-ocean contribution, which almost doubles the annual amplitude, while introducing a phase shift of three weeks.

Errors in both GRACE coefficients and the oceanic degree-1 and C_{20} coefficients contribute to the uncertainties in the obtained degree-1 and C_{20} time-series. However, GRACE errors only account for annual amplitude errors in geocenter motion at the 0.1-mm level, which is below 10% of the total signal. For C_{20} coefficients,

GRACE errors also contribute marginally (with less than 10%). The effect of this error on to the annual phase estimates is also minor (less than 3 days). In contrast, errors in oceanic degree-1 and C_{20} coefficients seem to play a somewhat larger role. By comparing estimates based on different OBP models, we conclude that the errors in oceanic degree-1 coefficients accounts for up to 15% of the annual amplitude estimates. While errors in oceanic C_{20} coefficients could cause a difference of about 20%. Again, annual phase estimates are not significantly affected (for all cases, the differences are well within two weeks).

Regarding trends in geocenter motion, we only calculate those driven by surface mass. GIA-induced trends are not reliably predicted by GIA models and are not restored.

As for the case of full $\dot{J}_2$, trend estimates are highly dependent on the adopted GIA model (Sun et al., 2016a). GIA has a direct effect in terms of solid earth contribution, but it also has an important secondary effect coming from the use of GRACE data to constrain surface mass redistribution at higher degrees (the GRACE-OBP method establishes a link between low- and high-degree gravity variations). The GIA effect on $\dot{J}_2$ estimates clearly appears from Tab. 4.5, where the difference between the $\dot{J}_2$ contribution of the two GIA models (direct effect) is about 10% ($0.3 \cdot 10^{-11}\, yr^{-1}$), whereas the difference in the derived surface contribution (indirect effect) is even larger ($0.4 \cdot 10^{-11}\, yr^{-1}$). Finally, the estimates of total $\dot{J}_2$ differ by as much as $0.7 \cdot 10^{-11}\, yr^{-1}$, when using two different GIA models.

For both geocenter and J_2 trends estimated with the GRACE-OBP method, a wider range of GIA models needs to be analysed in order to draw more definitive conclusions regarding the optimal data processing scheme and its accuracy.

In this study, the discussion has concentrated on annual variations and the linear trends, which are two prominent features of the geocenter motion and J_2 time-series. However, a consideration of them alone does not guarantee that the GRACE-OBP method provides the optimal estimates at other time-scales (or frequencies). To quantify the overall quality of the resulting time-series in a numerical study, it would be necessary to calculate the RMS difference between the synthetic truth and the obtained time-series. However, unlike the errors related to annual cycle and linear trend, the RMS error do not reduce in case of a relatively long time-series. As a result, one needs to pay more attention to mitigating the high-frequency noise in the resulting geocenter and J_2 variations. This will be subject of further studies.

5

Statistically Optimal Estimation of degree-1 and C_{20} Coefficients Based on GRACE Data and an Ocean Bottom Pressure Model

5.1. Introduction

Since its launch in 2002, the Gravity Recovery and Climate Experiment (GRACE) (Tapley et al., 2004) satellite mission allows data processing centers to produce monthly gravity field solutions (e.g. Bettadpur, 2012; Dahle et al., 2013; Watkins, 2012; Klinger and Mayer-Gürr, 2016; Farahani et al., 2017). After subtracting a mean gravity field, the obtained time variations in the Earth's gravity field reflect changes in its mass distribution. Apart from the gravity changes originated from the interior of the solid Earth, such as those due to the Glacial Isostatic Adjustment (GIA) and mega-thrust earthquakes, the observed signals are caused by mass variations within a very thin layer enveloping the solid Earth (oceans, continental water/ice/snow storage, etc.). Using GRACE data as input, one can uniquely estimate the surface mass variations with many applications in among others hydrolgy, glaciology, and oceanography.

Typically, a monthly GRACE gravity field solution is expressed by a set of Stokes coefficients (SHCs) complete to some maximum degree. One problem of these solutions is that they lack degree-1 coefficients (ΔC_{10}, ΔC_{11} and ΔS_{11}; the symbol Δ is dropped hereafter for simplicity), which are proportional to the geocenter motion defined as the displacement of center of mass of the whole Earth system (CM) with respect to the center of figure of the solid Earth (CF) (Ray, 1999). Omission of the degree-1 contribution leads to significant errors in surface mass estimates (Wu et al., 2012). Another problem of GRACE monthly solutions is that the C_{20} coefficient is subject to large uncertainties (Chen et al., 2016), presumably due to thermal-related systematic errors in the accelerometer data (Cheng and Ries, 2017). Therefore, for the purpose of inferring surface mass anomalies, a GRACE user is advised to complement GRACE solutions with independently estimated degree-1 coefficients and replace the native GRACE C_{20} coefficients with more accurate ones from SLR.

Most of studies published until now have been using the degree-1 coefficients as supplied by Swenson et al. (2008) (GRACE-OBP-Swenson), while the C_{20} coefficients are from SLR analysis (Cheng et al., 2013a). This approach, however, has some weak points. Firstly, the estimates of the degree-1 coefficients are not statistically optimal in the sense that errors in both GRACE data and the OBP model are not accounted for, as explained below. Secondly, the C_{20} coefficients produced from a different observation technique and with a different data processing procedure may not be consistent with GRACE solutions. As far as the degree-1 coefficients are concerned, their estimates provided with Swenson's approach are not statistically-optimal.

The GRACE-OBP-Swenson approach estimates degree-1 coefficients by combining GRACE data and oceanic degree-1 coefficients extracted from an Ocean Bottom Pressure (OBP) model. In its original implementation, this approach yields a much smaller annual amplitude of the C_{10} ($\sim$ 2 mm) than alternative techniques, such as SLR ($\sim$ 3 - $\sim$ 6 mm) (e.g. Cheng et al., 2013b; Sośnica et al., 2013; Ries, 2013) and

GPS-based inversion (~ 3 mm - ~ 4 mm) (e.g. Wu et al., 2006; Jansen et al., 2009; Rietbroek et al., 2012b). In Chapter 3 and 4, we developed an improved variant of the GRACE-OBP-Swenson approach (GRACE-OBP-Improved approach) by making a proper truncation of the input GRACE solutions, reducing GRACE signal leakage and taking into account self-attraction and loading (SAL) effects (Gordeev et al., 1977; Conrad and Hager, 1997). The resulting C_{10} annual amplitude was about 3 mm, i.e., in line with the GPS inversion method, as well as at least some of the SLR-based estimates published in the literature (e.g. Crétaux et al., 2002; Sośnica et al., 2013). In addition, C_{20} time-series estimated this way compared well with several SLR-based solutions (e.g. Cheng et al., 2013a; Lemoine et al., 2013).

However, one problem of both the GRACE-OBP-Improved method and the GRACE-OBP-Swenson method is that the degree-1 and C_{20} from an OBP models as well as GRACE data are treated deterministically, which implies that these data are free of error. As a consequence, any errors in OBP modeling and GRACE data propagate into degree-1 and C_{20} estimates in an uncontrolled way, i.e., the estimation procedure is statistically not optimal.

In this chapter, we propose to modify the GRACE-OBP approach in such a way that degree-1 and C_{20} coefficients are estimated by means of a statistically-optimal combination of GRACE data and an OBP model, which here is referred to as the "combination approach". Furthermore, a realistic estimation of uncertainties in the input data is part of the combination approach, which allows us to supply the estimated low-degree coefficients with a stochastic description of their errors.

The combination approach can also be considered as a variant of the joint inversion procedure (Rietbroek et al., 2009, 2012b), developed as an effort to improve global GPS inversions. In these studies, surface loading variations (up to a maximum degree of 30) were estimated from a combination of GPS, GRACE, and OBP data. As a result, the degree-1 information comes from GPS-derived degree-1 mass loading and the OBP data. However, the GPS tracking network is not homogeneously distributed, which may lead to a prominent network effect. Also, it is still challenging to isolate a load-induced contribution from the total GPS site movements (Dong et al., 2002). In addition, the deficiency in modeling/removing the draconitic error in GPS data processing (Griffiths and Ray, 2013) adds further uncertainty to GPS-sensed degree-1 information. Another problem of the above procedure is that the three datasets are not coupled. For example, total ocean mass is conserved, and water exchange with continents is ignored. In this study, the GPS data are not used. Furthermore, total ocean masses are coupled with surface mass changes over land.

It goes without saying that correcting GRACE solutions with accurate estimates of degree-1 and C_{20} coefficients improves the mass anomaly estimates. Still, it is important to quantify such improvements and to compare the obtained mass anomaly estimates with those based on the traditionally used degree-1 and C_{20} coefficients. Therefore, in this study we also propose a method to evaluate the quality of the

obtained degree-1 and C_{20} coefficients in terms of inferred surface mass anomalies.

The chapter is organized as follows. We describe the combination approach in details in Sect. 5.2. Then, we conduct numerical experiments to verify the correctness of the approach as well as to identify its optimal implementation parameters (Sect. 5.4). Afterwards, we apply the selected parameter setting to derive degree-1 and C_{20} time-series using real data (Sect. 5.5). We then demonstrate that using these coefficients improves the estimates of regional mass variations (Sect. 5.6). Finally, Sect. 5.7 concludes the chapter.

5.2. Methodology

5.2.1. Combination Approach

Various datasets can be combined in the statistically-optimal sense if their noise variance-covariance matrices are available (a general form of the optimal data combination is presented in Appendix A.1). The optimal data combination in the context of the GRACE-OBP-Improved approach is presented below.

Let the mass anomaly (in terms of equivalent water height) at a point k be denoted as h_k. The oceanic mass anomaly function can then be expressed as a linear combination of surface spherical harmonics:

$$h_k = \vartheta_k \sum_{l=1}^{\infty} \sum_{m=-l}^{l} C_{lm}^{(h)} Y_{lm,k}, \tag{5.1}$$

where ϑ_k represents the ocean function, which equals 1 if k is a point over ocean and equals 0 otherwise; $Y_{lm,k}$ is the 4π normalized surface spherical harmonic of degree l and order m at point k; $C_{lm}^{(h)}$ are the spherical harmonic coefficients describing surface mass re-distribution. These coefficients are called thereafter mass coefficients. Notice that the summation in Eq. (5.1) starts from degree 1, which implies a conservation of total mass. Also note that the summation is truncated at a certain degree in practice. Eq. (5.1) can be re-written in terms of matrix-to-vector multiplication as

$$\mathbf{h} = \mathbf{OYd}, \tag{5.2}$$

where $\mathbf{h}$ is the $K \times 1$ vector of mass anomalies h_k, with K the number of grid points; $\mathbf{Y}$ is the $K \times L$ matrix with entries equal to $Y_{lm,k}$; $\mathbf{d}$ is the $L \times 1$ vector containing coefficients $C_{lm}^{(h)}$ starting from degree 1, with L the number of mass coefficients, and $\mathbf{O}$ is a $K \times K$ diagonal matrix with elements representing the ocean function, that is,

$$\{\mathbf{O}\}_{(k,k)} = \begin{cases} 1 & \text{if } k \text{ is a point in ocean} \\ 0 & \text{if } k \text{ is a point on land.} \end{cases} \tag{5.3}$$

Assuming that mass redistribution takes place in a thin spherical layer, we can relate the mass coefficients to the dimensionless SHCs, according to Wahr et al. (1998)

$$\mathbf{d} = \mathbf{S}\mathbf{x}, \tag{5.4}$$

where $\mathbf{x}$ is the $L \times 1$ vector containing the set of dimensionless SHCs. $\mathbf{S}$ is the $L \times L$ diagonal matrix with entries

$$\{\mathbf{S}\}_{(lm,lm)} = \frac{(2l+1)}{3(1+k_l)} \frac{\rho_{\text{earth}}}{\rho_{\text{water}}} a, \tag{5.5}$$

where a is the Earth's average radius; ρ_{earth} is the average density of the Earth, ρ_{water} is the density of water and k_l is the load Love number of degree l. Note that $k_1 = 0.021$, which implies that it is defined in the CF reference frame (Blewitt, 2003).

Therefore, our functional model is:

$$\begin{cases} \mathbf{T}\mathbf{x} = \mathbf{x}_g \\ \mathbf{OYS}\mathbf{x} = \mathbf{h}, \end{cases} \tag{5.6}$$

where $\mathbf{x}_g$ is a $L_g \times 1$ vector containing the SHCs provided by GRACE, L_g equals $(L-4)$ since we assume that degree-1 and C_{20} coefficients are absent; $\mathbf{T}$ is a truncated unit matrix of size $L_g \times L$ matrix applied to truncate the $\mathbf{x}$ vector,

$$\mathbf{T} = \begin{bmatrix} 0 & 0 & 0 & 0 & 1 & 0 & \cdots & \cdots & 0 \\ 0 & 0 & 0 & 0 & 0 & \ddots & \ddots & \ddots & \vdots \\ \vdots & \vdots & \vdots & \vdots & \vdots & \ddots & \ddots & \ddots & \vdots \\ \vdots & \vdots & \vdots & \vdots & \vdots & \ddots & \ddots & \ddots & 0 \\ 0 & 0 & 0 & 0 & 0 & \cdots & \cdots & 0 & 1 \end{bmatrix}. \tag{5.7}$$

Then, the result of the combination approach is given as

$$\mathbf{x}_c = (\mathbf{T}^T\mathbf{C}^{-1}\mathbf{T} + \mathbf{S}\mathbf{Y}^T\mathbf{O}\mathbf{C}_o^{-1}\mathbf{O}\mathbf{Y}\mathbf{S})^{-1}(\mathbf{T}^T\mathbf{C}^{-1}\mathbf{x}_g + \mathbf{S}\mathbf{Y}^T\mathbf{O}\mathbf{C}_o^{-1}\mathbf{h}), \tag{5.8}$$

where $\mathbf{x}_c$ $(L \times 1)$ denotes the set of re-estimated SHCs obtained after combining the two datasets, with the first four elements being the degree-1 and C_{20} coefficients; $\mathbf{C}$ $(L_g \times L_g)$ is the full noise variance-covariance matrix of the SHCs from GRACE and $\mathbf{C}_o$ $(K \times K)$ is the noise variance-covariance matrix of the oceanic mass anomalies.

5.2.2. Input Data in General Terms

GRACE Data and Their Noise Covariance Matrices

The input GRACE SHCs ($\mathbf{x}_g$) are the so-called GSM coefficients. Such coefficients are reduced for tidal contributions (with the use of a particular ocean tide model). Non-tidal atmospheric and oceanic contributions are also reduced from GRACE observations in the level-1 data processing using the Atmosphere and Ocean De-aliasing level-1B (AOD1B) products (Flechtner and Dobslaw, 2013). Monthly averages of the removed non-tidal effects are provided in the form of SHCs in the so-called GAC files. GAD files are the same as GAC, but restricted to ocean areas. However, the oceanic contributions are from an OBP model, which conserves the ocean water mass. Water exchange between ocean and land is thus ignored. Also, the OBP model does not take into account SAL effects. Consequently, the total ocean mass change signal as well as the fingerprints due to SAL effects remain in the GSM coefficients.

As for the noise covariance matrices of GRACE data, CSR RL05 solutions are used throughout the study.

Oceanic Data and Their Noise Covariance Matrices

Oceanic mass anomalies are provided by an OBP model, which is also used to produce GRACE GSM coefficients. In order to be compatible with the input GRACE data, tidal and non-tidal oceanic contributions have to be removed from the oceanic data. As a result, when working with GRACE GSM coefficients, oceanic mass anomalies predicted by the OBP model are set equal to zero. As mentioned, we need to additionally estimate the signals caused by ocean-land mass exchange and fingerprints. Here, we estimate the total ocean mass variations by integrating GRACE-derived mass anomalies over the oceans. Then we account for SAL effects and determine the fingerprints in ocean waters (Mitrovica et al., 2001) by solving the sea level equation (Farrell and Clark, 1976; Tamisiea et al., 2010). It is worth noting that using GRACE to estimate the total ocean mass variation requires a complete GRACE solution including degree-1 and C_{20} coefficients. Therefore, total ocean mass variation is determined through an iterative procedure. The four targeting coefficients are set equal to zero as a starting point and later updated with estimates of these coefficients. The total ocean mass variation as well as the estimated coefficients converge quickly with only 3 or 4 iterations (thereafter, the difference between the subsequent solutions is smaller than 0.1%, see also Fig. 5.1).

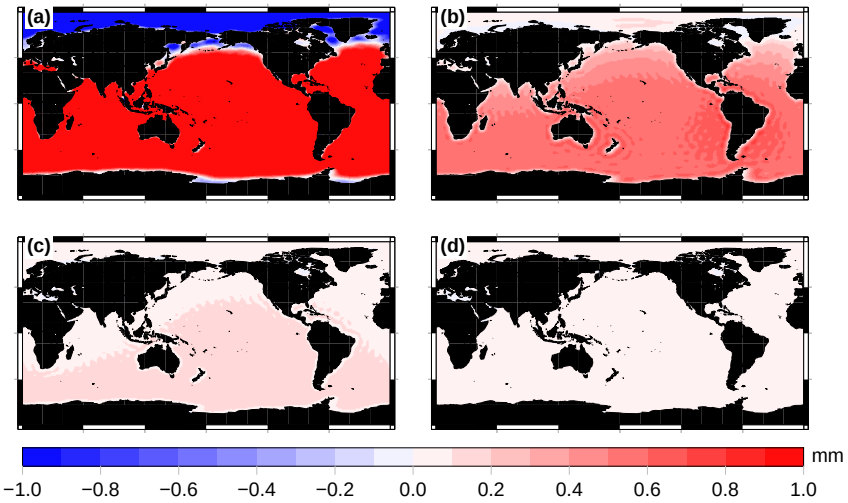

Figure 5.1: Oceanic mass anomalies updates at different iterations. In panel a, b, c and d we show the updates for iteration 1 (RMS: 2 mm; Maximum value: 6 mm), iteration 2 (RMS: 0.4 mm; Maximum value: 0.8 mm), iteration 3 (RMS:0.08 mm, Maximum value: 0.2 mm) and iteration 4 (RMS: 0.01 mm, Maximum value: 0.03 mm), respectively.

Unlike for GRACE data, the error covariances of the OBP estimates are not provided directly. In the following, we will estimate the uncertainty σ_k at each oceanic data point in order to construct, at least, a diagonal noise covariance matrix for the OBP estimates.

Since the oceanic mass anomaly is a combination of the OBP model output (the OBP model error has to be considered even though the residual signal is zero) and the fingerprints, the RMS error σ_k at a given ocean point can be easily computed under the assumption that the error from these two sources are not cross-correlated:

$$\sigma_k^2 = \sigma_{\text{obp},k}^2 + \sigma_{\text{fts},k}^2, \tag{5.9}$$

where $\sigma_{obp,k}$ and $\sigma_{fts,k}$ are the RMS errors of OBP and fingerprints, respectively. The computation of them is described in Sect. 5.4.2.

The matrix $\mathbf{C}_o$ is defined as a diagonal matrix. Ignoring the error correlations may result in the overestimation of the OBP model accuracy and, therefore, in a too high weight assigned to the OBP predictions. In order to overcome this problem, we propose to scale the diagonal matrix $\mathbf{C}_o$ uniformly by a factor α.

$$\{\mathbf{C}_o\}_{(k,k)} = \alpha\sigma_k^2, \tag{5.10}$$

The optimal choice of alpha will be discussed later in Sect. 5.4.2. Therefore, we can introduce a diagonal weight matrix

$$\mathbf{P} = \mathbf{O}\mathbf{C}_o^{-1}, \tag{5.11}$$

with elements equal to

$$\{\mathbf{P}\}_{(k,k)} = \begin{cases} \frac{1}{\alpha\sigma_k^2} & \text{if } k \text{ is a point in ocean} \\ 0 & \text{if } k \text{ is a point on land.} \end{cases} \tag{5.12}$$

Finally, Eq. (5.8) can be re-written as

$$\mathbf{x}_c = (\mathbf{T}^T\mathbf{C}^{-1}\mathbf{T} + \mathbf{S}\mathbf{Y}^T\mathbf{P}\mathbf{Y}\mathbf{S})^{-1}(\mathbf{T}^T\mathbf{C}^{-1}\mathbf{x}_g + \mathbf{S}\mathbf{Y}^T\mathbf{P}\mathbf{h}). \tag{5.13}$$

5

5.2.3. Relation with the GRACE-OBP Method

The basic idea behind the combination approach and the GRACE-OBP approach are very similar. Here, we show how the two methods are inter-related.

Let us define $\mathbf{x}_e$ as a 4×1 vector with entries equal to the degree-1 and C_{20} coefficients and $\mathbf{x}_g$ as a $(L-4) \times 1$ vector containing coefficients provided by GRACE (C_{20} coefficient is excluded). Assume that both $\mathbf{x}_e$ and $\mathbf{x}_g$ are free of errors. Then, the whole set of error-free SHCs $\mathbf{x}$ can be represented as:

$$\mathbf{x} = \mathbf{T}_e^T\mathbf{x}_e + \mathbf{T}^T\mathbf{x}_g, \tag{5.14}$$

where $\mathbf{T}_e$ is a $4 \times L$ matrix:

$$\mathbf{T}_e = \begin{bmatrix} 1 & 0 & 0 & 0 & 0 & \cdots & 0 \\ 0 & 1 & 0 & 0 & 0 & \cdots & 0 \\ 0 & 0 & 1 & 0 & 0 & \cdots & 0 \\ 0 & 0 & 0 & 1 & 0 & \cdots & 0 \end{bmatrix}. \tag{5.15}$$

The second line in Eq. (5.6) can be written as

$$\mathbf{h} = \mathbf{O}\mathbf{Y}\mathbf{S}(\mathbf{T}_e^T\mathbf{x}_e + \mathbf{T}^T\mathbf{x}_g) = \mathbf{O}\mathbf{Y}\mathbf{S}\mathbf{T}_e^T\mathbf{x}_e + \mathbf{h}_g, \tag{5.16}$$

Thereby, $\mathbf{h}_g$ $(K \times 1)$ represents oceanic mass anomalies without the contribution from the degree-1 and C_{20} coefficients. We subtract $\mathbf{h}_g$ from both sides of Eq. (5.16),

which allows us to isolate the contribution of the degree-1 and C_{20} coefficients. That is

$$\mathbf{h} - \mathbf{h}_g = \mathbf{OYST}_e^T \mathbf{x}_e. \tag{5.17}$$

Note that $\mathbf{T}_e^T \mathbf{T}_e$ yields an idempotent matrix, i.e., $\mathbf{T}_e^T \mathbf{T}_e = \mathbf{T}_e^T \mathbf{T}_e \mathbf{T}_e^T \mathbf{T}_e$; $\mathbf{S}$ and $\mathbf{T}_e^T \mathbf{T}_e$ commute because they are diagonal matrices, i.e., $\mathbf{ST}_e^T \mathbf{T} = \mathbf{T}_e^T \mathbf{TS}$. As a result, Eq. (5.17) can be written as:

$$\begin{aligned} \mathbf{h} - \mathbf{h}_g &= \mathbf{OYST}_e^T \mathbf{T}_e \mathbf{x} \\ &= \mathbf{OYST}_e^T \mathbf{T}_e \mathbf{T}_e^T \mathbf{T}_e \mathbf{x} \\ &= \mathbf{OYT}_e^T \mathbf{T}_e \mathbf{ST}_e^T \mathbf{T}_e \mathbf{x} \\ &= \mathbf{OY}' \mathbf{S}' \mathbf{x}_e. \end{aligned} \tag{5.18}$$

where $\mathbf{Y}'$ is a $K \times 4$ matrix and $\mathbf{S}'$ is 4×4 matrix; they are the same as $\mathbf{Y}$ and $\mathbf{S}$, but only for the degree-1 and C_{20} coefficients. Eq. (5.18) can be considered as a linear functional model connecting an unknown vector $\mathbf{S}'\mathbf{x}_e$ and data vector $\mathbf{h} - \mathbf{h}_g$. Then, $\mathbf{x}_e$ can be solved for by plain linear regression. The obtained equation

$$\mathbf{S}' \mathbf{Y}'^T \mathbf{OY}' \mathbf{S}' \mathbf{x}_e = \mathbf{S}' \mathbf{Y}'^T \mathbf{Oh} - \mathbf{S}' \mathbf{Y}'^T \mathbf{Oh}_g, \tag{5.19}$$

or

$$\mathbf{Y}'^T \mathbf{OY}' \mathbf{S}' \mathbf{x}_e = \mathbf{Y}'^T \mathbf{Oh} - \mathbf{Y}'^T \mathbf{Oh}_g, \tag{5.20}$$

is the same as Eq. (12) in Swenson et al. (2008) if written out explicitly (see Appendix A.2). The resulting solution is optimal provided that the noise in $\mathbf{h} - \mathbf{h}_g$ is white. Therefore, if the GRACE data are noise-free (so that $\mathbf{h}_g$ contains deterministic values and one does not have to estimate $\mathbf{x}_g$) and the noise in OBP data is white, the combination approach reduces to the GRACE-OBP approach.

5.3. Implementation Parameters

In Chapter 4, we have already shown that estimates of degree-1 and C_{20} time-series based on the GRACE-OBP approach are controlled by at least three implementation parameters: (i) maximum degree of the input GSM coefficients, (ii) width of the buffer zone (a periphery surrounding the continents due to the application of a

shrunk ocean function) and (iii) whether to consider SAL effects when distributing water over oceans or not. We also addressed the optimal choice of implementation parameters by means of numerical simulations. They showed that the set of input GSM coefficients should be truncated between degree 30 and 50, in order to include mass re-distribution at large spatial scales while excluding high-degree coefficients contaminated by large errors. The buffer zone should be around 200 km to mitigate the impact of continental signal leakage. Also, the ocean water has to be distributed realistically by taking into account SAL effects. We expect that the optimal truncation degree and the buffer zone width found in Chapter 4 will not change significantly in the combination approach. Therefore, we limit ourselves to the most promising combinations of implementation parameters. We test truncation degrees between 10 and 60, and buffer zones widths of 100, 200 and 300 km; SAL effects are always taken into account.

5.4. Numerical Experiments

Numerical experiments are carried out to verify the correctness and evaluate the performance of our methodology.

5.4.1. Simulation of GRACE GSM Coefficients

The procedure to generate GRACE GSM coefficients is very similar to that described in Chapter 4. It is based on the updated ESA Earth System Model (ESM), which covers the period from 1995 to 2016 and is complete to spherical harmonic degree 180 (Dobslaw et al., 2015). It employs state-of-the-art geophysical models to simulate gravity changes due to mass re-distribution within the Earth system. It is worth noting that we have added SAL effects to the original ESM model. We sum up the contributions of the atmosphere, ocean, continental water, and ice-sheet components to mimic GRACE-sensed gravity changes due to surface mass re-distribution. The error-free GSM coefficients are then generated by removing the monthly average of the dealiasing product, called DEAL coefficients, which represent a simplified model of mass transport in the atmosphere and ocean; they play the same role as the AOD1B product. The DEAL coefficients are provided together with the ESM. Two types of errors present in real GRACE GSM are added to the simulated error-free GSM coefficients to obtain realistically perturbed ones. First, random errors are simulated using the CSR RL05 monthly noise covariance matrices complete to degree 60. To make the results more representative, we generate ten error realizations per month. Second, we additionally introduce one realization of errors in the DEAL product, which is provided together with the ESM as the so-called AOerr files. The errors documented in the AOerr files are first defined as the differences between the updated ESM (the one used in this study) and the original ESM model, and then upscaled to match the uncertainty estimated by pairwise model comparisons based on a small ensemble (four) of atmospheric and oceanic models.

As a result, ten sets of noisy GSM coefficients per month are at our disposal. The sets are contaminated by different random errors and the same AOerr errors. For more details regarding the data simulation procedure, the reader is referred to Chapter 4.

5.4.2. Determination of Oceanic Noise Variances

The combination approach requires stochastic information about errors in the oceanic mass anomalies, which is not directly available. In this study, we estimate the RMS error σ_k at each data point of a 1×1 degree ocean grid. According to Eq. (5.9), one needs to know the RMS error $\sigma_{obp,k}$ (for the OBP mass anomaly) and the RMS error $\sigma_{fts,k}$ (for the fingerprint mass anomaly). To obtain $\sigma_{obp,k}$, we use the OBP error estimates provided by the ESM. Since only one error realization per monthly OBP is given, we assume that the OBP noise is stationary in the time domain and calculate the RMS error per grid node using all monthly error estimates (Fig. 5.2a). For $\sigma_{fts,k}$, we calculate fingerprints from ten realizations of simulated noisy GSM coefficients. Assuming that the fingerprint noise is also stationary in the time domain, we compute the RMS error by averaging errors over months and noise realizations (Fig. 5.2b). Finally, σ_k (Fig. 5.2c) is computed through Eq. (5.9).

As explained in Sect. 5.2.2, a scaling factor (α) has to be introduced to account for the lack of information about OBP error covariances. To estimate the scaling factor, we use two criteria. First, the scaled error covariance matrix $\mathbf{C}_o$ should result in minimal Actual RMS Errors (ARE) when comparing the resultant degree-1 and C_{20} estimates with the synthetic truth. Second, the obtained Formal RMS Errors (FRE) for degree-1 and C_{20} solutions should be of similar magnitude as the ARE. To make the calculation of ARE and FRE easier to understand, we visualise them in Fig. 5.3.

We calculate the ARE ($e^{\mathrm{cf},n}_{\mathrm{ARE}}$) and the FRE ($e^{\mathrm{cf},n}_{\mathrm{FRE}}$) for a particular coefficient (indicated by superscript cf, which runs over the four estimated mass SHCs, namely C_{10}, C_{11}, S_{11} and C_{20}) based on the n^{th} GSM realization. The best scaling factor, however, is different from coefficient to coefficient and from realization to realization. To obtain a uniform choice, we further calculate the combined ARE ($e^{\mathrm{cmb}}_{\mathrm{ARE}}$) and the combined FRE ($e^{\mathrm{cmb}}_{\mathrm{FRE}}$) (shown in Fig. 5.4 as a function of scaling factor):

$$
\begin{aligned}
e^{\mathrm{cmb}}_{\mathrm{ARE}} &= \sqrt{\sum_{\mathrm{cf}=C_{10}}^{C_{20}} (AVR < e^{\mathrm{cf},n}_{\mathrm{ARE}}, (n = 1,2,\ldots,N) >)^2}, \\
e^{\mathrm{cmb}}_{\mathrm{FRE}} &= \sqrt{\sum_{\mathrm{cf}=C_{10}}^{C_{20}} (AVR < e^{\mathrm{cf},n}_{\mathrm{FRE}}, (n = 1,2,\ldots,N) >)^2},
\end{aligned}
\tag{5.21}
$$

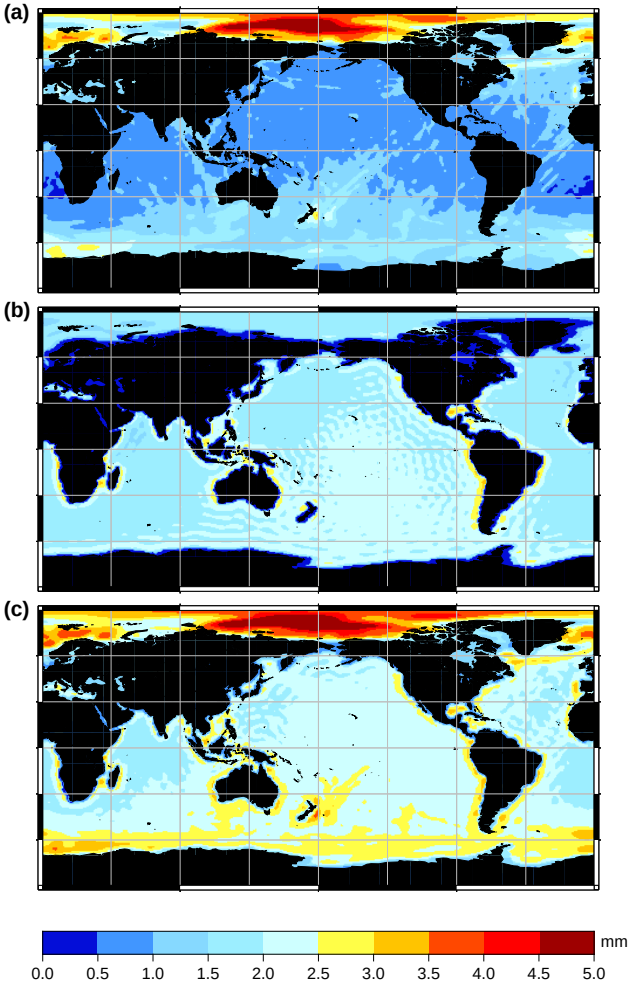

Figure 5.2: Uncertainty of oceanic mass anomalies. (a) The RMS error of OBP predictions. (b) The RMS error of fingerprints. (c) Total RMS error obtained with Eq. (5.9).

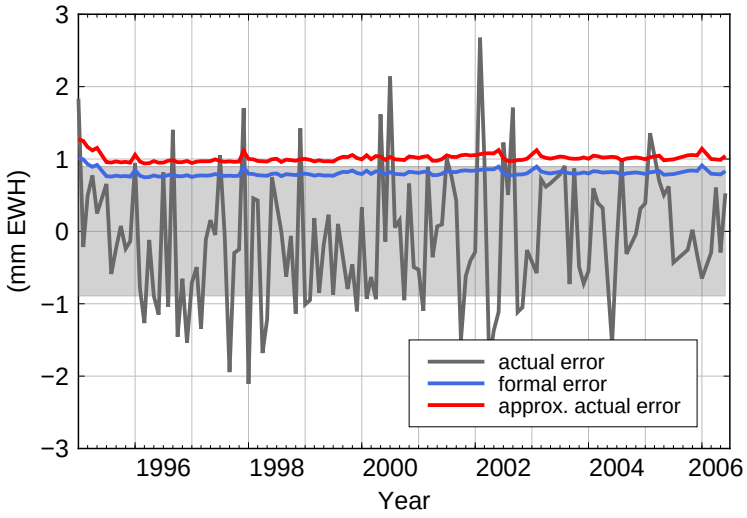

Figure 5.3: Actual error, actual RMS error (ARE) and approximated actual RMS error (approx. ARE) for one realization of synthetic C_{10} coefficients. The actual errors are obtained as the differences between the resulting C_{10} time-series and the synthetic truth. ARE is then obtained as the RMS difference, which is shown as a gray band (the upper and lower bound of the gray band is then ± ARE).

where N is the number of sets of simulated GSM coefficients ($N = 10$). Further increasing N does not change the results significantly. $AVR <>$ is the operator of averaging RMS errors over all error realizations. Note that according to the Parseval's identity, the sum of squared spherical harmonic coefficients describing the mass transport function is equal (up to a constant scaling factor, i.e., $4\pi a$) to the squared L2-norm of the mass transport function itself.

As α increases, the combined ARE decreases until convergence (within 1% for $\alpha > 45$), whereas the combined FRE increases linearly. The decrease of the combined ARE means that the obtained solution gets closer to the statistically-optimal one, which is an indication that the assumed errors in the OBP estimates become more reasonable as α increases. A proper choice for the scaling factor is therefore at the intersection of the two curves, which is around 55 (corresponds to the upscaling of the RMS error with a factor of about 7.5). It is worth noting that the optimal scaling factor does not change significantly with different implementation parameter setups.

In real data processing, information of ARE is not available. Therefore, we propose to estimate the actual error using the approach of Ditmar et al. (2017), which allows us to approximate the actual error in a time-series without the knowledge of the true signal. More information can be found in Appendix B.1.

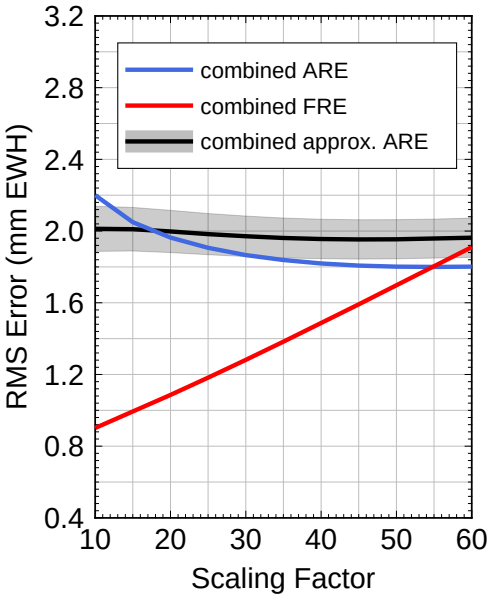

Figure 5.4: Combined ARE, combined FRE and combined approximated ARE as functions of the scaling factor. The gray band along the combined approximated ARE curve shows its STD from ten GSM realizations. Note that the parameter setup is: truncation degree: 50, buffer zone width: 200 km.

The conducted numerical study allows us to validate the procedure in the context of low-degree coefficients. In Fig. 5.3, we also show an example of time-series of the estimated RMS of the actual errors. We calculate the combined approximated ARE for the four coefficients ($e^{\text{cmb}}_{\text{approx. ARE}}$) following a similar equation as Eq. (5.21):

$$e^{\text{cmb}}_{\text{approx. ARE}} = \sqrt{\sum_{\text{cf}=C_{10}}^{C_{20}} (AVR < e^{\text{cf},n}_{\text{approx. ARE}}, (n = 1,2,\ldots,N) >)^2}. \tag{5.22}$$

Clearly, $e^{\text{cmb}}_{\text{approx. ARE}}$ is the average over ten error realizations. This is not the case when dealing with real data, where only one error realization (true error) is available. Fortunately, the $e^{\text{cf},n}_{\text{approx. Err}}$ does not change significantly from realization to realization (see the gray band in Fig. 5.4).

For all error realizations, the scaling factor determined from the approximated actual error and the formal error is fairly close to the optimal scaling factor, which is equal to 55 in the considered case. Therefore, it is recommended to use the same procedure when processing real data. The obtained formal error will change linearly if the scaling factor determined differs from the optimal one.

5.4.3. Quality Indicator

The resulting degree-1 and C_{20} time-series based on each parameter combination are compared with the synthetic truth (the scaling factor α is fixed to 55). Our goal is to select the setup that leads to the minimal RMS error of the resulting time-series. To that end, we compute the RMS of the differences between the resulting time-series ($T(C_{lm}^{(h)})$) and the synthetic truth ($T(C_{lm}^{t(h)})$) in terms of equivalent water heights. In Fig. 5.5, we show the RMS errors for all the tested parameter combinations as functions of the truncation degree. Best estimates for degree-1 and C_{20} time-series are obtained with a 200-km buffer zone and a truncation degree between 30 and 50. For C_{20}, it becomes worse around degree 40 for reasons that are still under investigation. We also show the RMS errors for solutions based on the GRACE-OBP-Improved method (200-km buffer width, SAL effects are taken into account) for comparison. Additionally, we show the results obtained with the original implementation parameters of Swenson et al. (2008). The combination approach clearly outperforms the two latter approaches by producing solutions with lower RMS errors.

However, our goal is to determine the unified optimal parameter setup that would lead to the best estimation of all the considered coefficients. To this end, we use the sum of error variances of the four coefficient time-series as the overall quality indicator (QI):

$$QI = \frac{1}{N}\sum_{n=1}^{N}(VAR < T(C_{10}^{(h)})^n - T(C_{10}^{t(h)}) > + VAR < T(C_{11}^{(h)})^n - T(C_{11}^{t(h)}) > + \\ VAR < T(S_{11}^{(h)})^n - T(S_{11}^{t(h)}) > + VAR < T(C_{20}^{(h)})^n - T(C_{20}^{t(h)}) >), \tag{5.23}$$

where $VAR <>$ is the operator for calculating the variance of a time-series; n indicates the dataset number ($n = 1,2,\ldots,N$), and N is the total number of datasets ($N = 10$). Note that all the coefficients are defined in terms of equivalent water height. Our intention is to choose the parameter setting that leads to the lowest QI value. Fig. 5.6 shows that a truncation degree larger than 35 and a buffer width of 200 km are the preferred setup.

While the QI values give an indication of the overall quality of the resultant degree-1 time-series, it is the annual cycle (the largest periodic signal) that is particularly interesting. In Fig. 5.7 and 5.8, we show the mean annual amplitude and phase estimates of degree-1 and C_{20} time-series and their standard deviations. For annual amplitudes (Fig. 5.7), the estimates are getting closer to the synthetic truth as the truncation degree increases. However, when using the narrow buffer (100 km), one cannot recover the true annual amplitude with any truncation degree for C_{10}, S_{11} and C_{20}. With a wider buffer (200 or 300 km), we can recover the annual amplitude within 10% for all four coefficients when using truncation degrees higher than 35. For annual phase estimates, we see less dependence on the implementa-

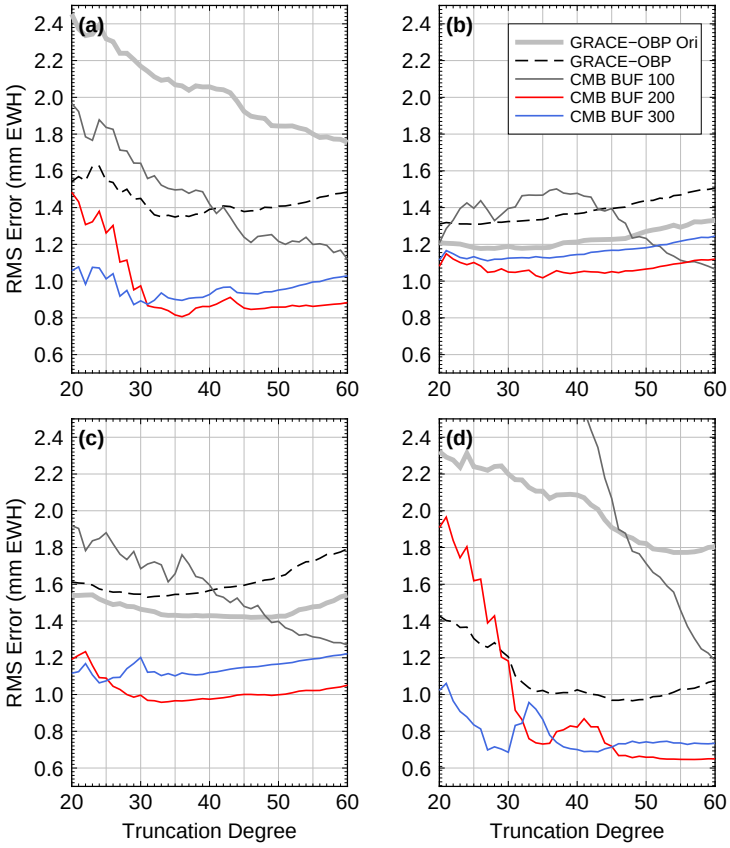

Figure 5.5: The RMS errors (average over ten simulated GSM solutions) for resulting degree-1 and C_{20} coefficient time-series (in mm of equivalent water height). Results for C_{10}, C_{11}, S_{11} and C_{20} are presented in panel (a), (b), (c) and (d), respectively. The thick gray lines show the results of the GRACE-OBP-Swenson approach. The dashed gray lines indicate solutions based the GRACE-OBP-Improved approach considering SAL effects and using a 200-km buffer zone.

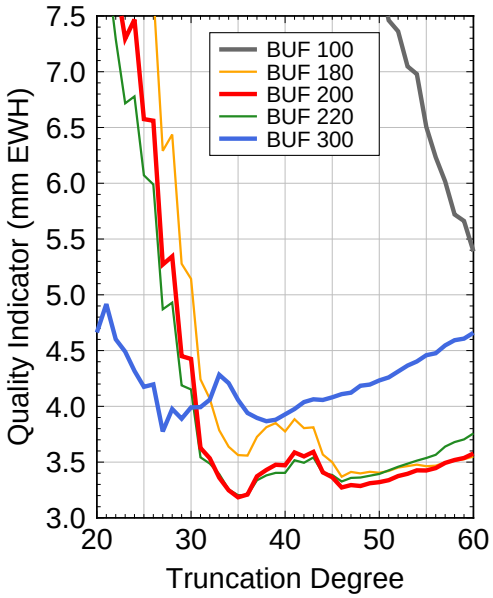

Figure 5.6: The same as Fig. 5.5, but the unified quality indicator is shown instead of RMS errors per coefficient.

tion parameters. In most cases (except for the C_{10} estimates based on a 100-km buffer zone) one can recover the true annual phase within 5 days. In addition to the QI mentioned above, we compute the QI for annual variations based on Chapter 4 (Eq. 4.7). Consideration of this criterion confirms that, larger truncation degrees are beneficial for estimating annual variations (Fig. 5.9).

Ultimately, we recommend to use a truncation degree of 50 and buffer width of 200 km. In Chapter 4, the same buffer width was selected but the truncation degree was 45.

The selected parameter setup ensures good estimates of both overall quality and annual variations in all four coefficients.

5.5. Results Based on Real Data

We produce degree-1 and C_{20} time-series using real GRACE data as input. The CSR RL05 GRACE monthly solutions (complete to degree 60) for a 12-year period from August 2002 to June 2014 and their corresponding noise variance-covariance matrices are used. We correct the input GSM coefficients for the pole tide according to Wahr et al. (2015). The GIA effects are corrected for by removing the GIA model

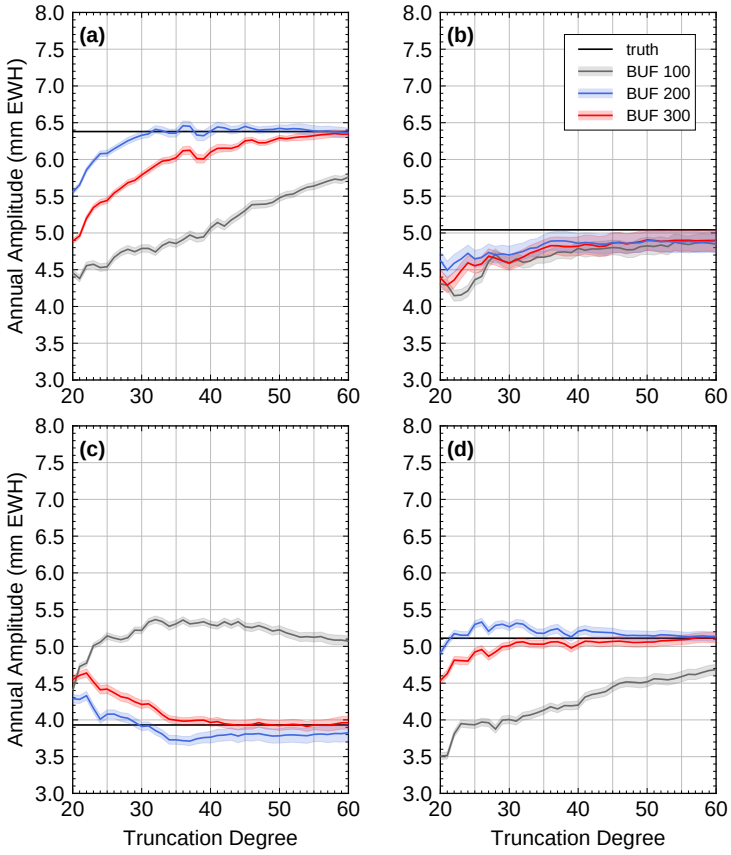

Figure 5.7: The mean annual amplitudes of the GSM degree-1 and C_{20} time-series (mm EWH) estimated using different implementation parameters, based on ten sets of simulated GSM solutions. The standard deviations of amplitude estimates (based on ten sets of GSM solutions) are indicated by light colored bands. The true amplitudes are marked in all panels as black horizontal lines. Results for C_{10}, C_{11}, S_{11} and C_{20} are shown in panel (a), (b), (c), and (d), respectively.

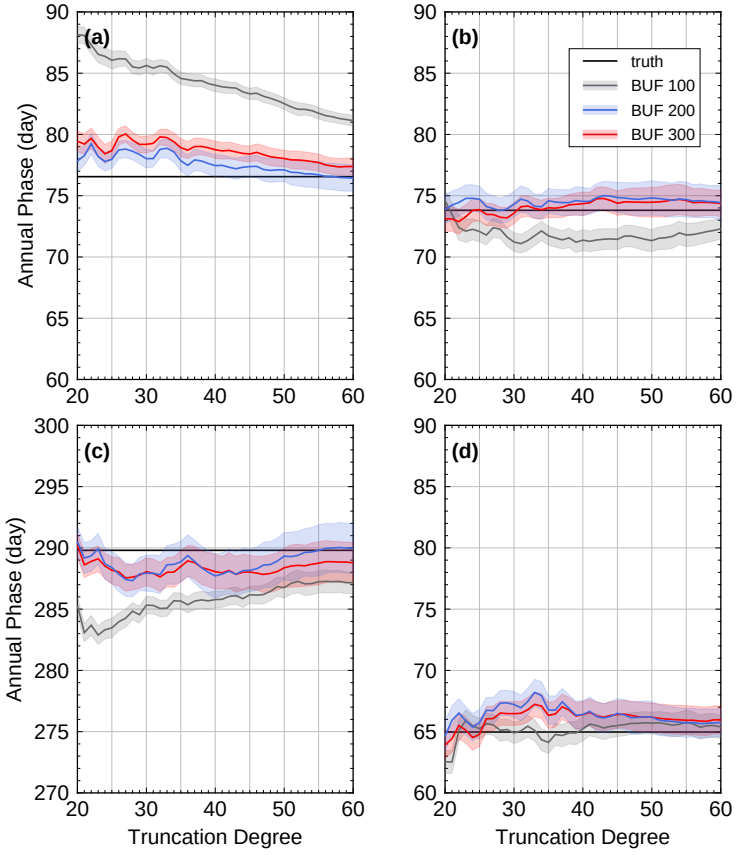

Figure 5.8: The same as Fig. 5.7, but for the annual phases.

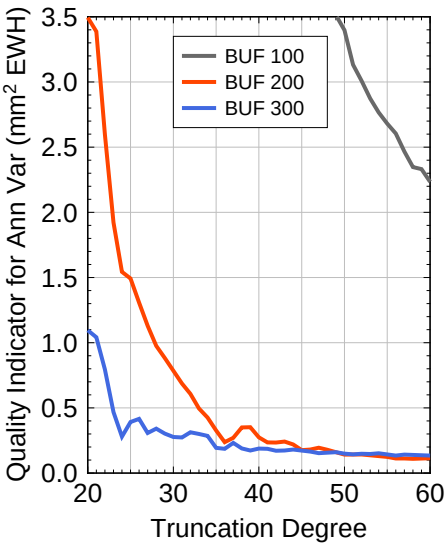

Figure 5.9: The same as Fig. 5.6, but the quality indicator for annual variations is shown instead of quality indicator for RMS error.

computed by A et al. (2012). Degree-1 coefficients in the CF reference frame are kindly provided by the authors through personal communication. These modeled degree-1 trends are not used during the calculation, but can be useful at the last stage to restore the GIA contributions to the resulting degree-1 solutions. Other time-variable solid Earth signals are ignored as in previous studies (Swenson et al., 2008).

The noise covariance matrix of the oceanic data is the same as determined in the numerical experiments (Section 5.4), but scaled with a different scaling factor. In order to determine the proper scaling factor, a number of candidates (in the range from 50 to 150) are tested. For each scaling factor, we estimated the time-series of the four low-degree coefficients and the associated combined formal error. According to Fig. 5.10, the optimal scaling factor is 120. The choice of the scaling factor has minor effects on the estimated coefficients but strongly affects the formal error estimation.

The final time-series are shown in Fig. 5.11a, where the degree-1 time-series are compared against the solutions from the GRACE-OBP-Swenson approach (Swenson et al., 2008), and the C_{20} time-series is compared to a SLR solution (Cheng et al., 2013a). Our C_{10} and C_{11} time-series have larger annual amplitudes while the S_{11} time-series is almost indistinguishable from the Swenson's solution. Our C_{20} time-series is free of large anomalies with a period of 161 days and has other considerable differences from the SLR one, especially after 2011. Notice that our C_{20} time-series

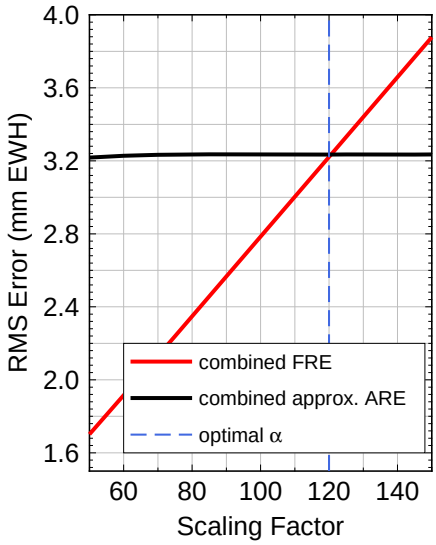

Figure 5.10: Combined FRE and combined approximated ARE as functions of the scaling factor. Note that the parameter setup is: truncation degree: 50, buffer zone width: 200 km.

shows a more pronounced annual cycle, which is reasonable in view of a seasonal mass exchange between oceans and continents.

We compare also the low-degree coefficients estimated with different geodetic techniques in terms of annual variations (Tab. 5.1), we see that annual variations predicted with the combination approach and the GRACE-OBP-Improved approach are in line with those based on independent methodologies. An exception is a discrepancy in the annual phase estimates of C_{10}. Solutions based on GRACE and OBP data, including those based on the combination approach, the GRACE-OBP-Improved approach, and the GRACE-OBP approach, are more than a month behind those based on other techniques. We show in the next section (Sect. 5.6) that the GRACE-OBP-based solutions are likely more accurate.

One of the advantages of the combination approach is that it provides the noise variances and covariances of the estimated coefficients (Fig. 5.11b). We show that the formal errors of degree-1 and C_{20} coefficients are different from month to month and generally larger than those documented in the product based on GRACE-OBP-Swenson (ftp://podaac.jpl.nasa.gov/allData/tellus/L2/degree_1/deg1_coef.txt). The correlations between the errors in these coefficients are rather small except those between C_{10} and C_{20} (Fig. 5.11c). This is expected because the polar areas play the major role in the separation of these coefficients (the corresponding surface spherical harmonics reach there local maxima in absolute value). However, there is a lack of oceanic data in the southern polar region caused by the presence of

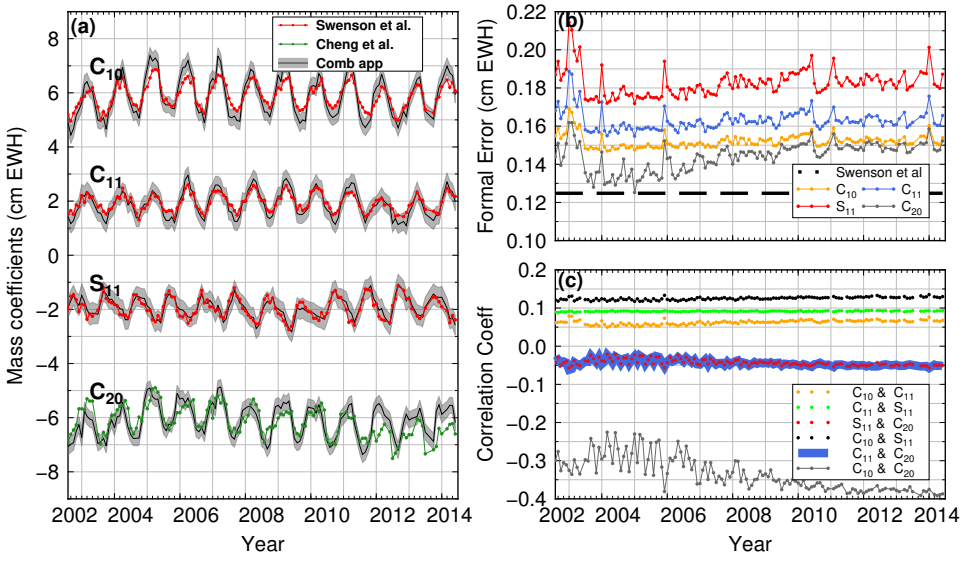

Figure 5.11: Final solutions for degree-1 and C_{20} time-series (a), their formal error estimates (b), and correlation coefficients (c) based on the combination approach. In panel a, linear trends are removed. Results are offset for clarity. The colored bands show the 2-σ uncertainties. The black dashed line shown in panel b (denoted as "Swenson et al") is taken from the official product based on (Swenson et al., 2008) (see text).

Table 5.1: Estimated amplitudes and phases of the annual variations of degree-1 and C_{20} coefficients, based on real data. The contribution of atmosphere and ocean (GAC) is restored. Please note that the annual amplitude A and phase ϕ are defined by $A\cos(2\pi(t-t_0)-\phi)$, where t_0 refers to January 1 of a particular year. The solutions 'Combination approach *' and 'Combination approach **' are estimated over reduced time intervals to be more comparable with those from (Wu et al., 2015) and (Rietbroek et al., 2012b).

	C_{10}		C_{11}		S_{11}		C_{20}		
	Amp (mm)	Pha (day)	Amp (mm)	Pha (day)	Amp (mm)	Pha (day)	Amp (10^{-11})	Pha (10^{-11})	Time span
Combination approach	3.2 ± 0.2	66 ± 3	2.4 ± 0.1	61 ± 3	2.6 ± 0.1	333 ± 2	16.2 ± 0.7	48 ± 3	2002 Aug - 2014 Jun
Combination approach *	3.1 ± 0.2	64 ± 3	2.4 ± 0.1	58 ± 3	2.6 ± 0.1	333 ± 2	15.7 ± 0.7	47 ± 3	2002 Aug - 2009 Apr
Combination approach **	3.0 ± 0.2	64 ± 3	2.5 ± 0.1	57 ± 3	2.6 ± 0.1	334 ± 2	15.4 ± 0.7	46 ± 3	2003 Jan - 2008 Dec
GRACE-OBP-Improved	2.9 ± 0.2	68 ± 3	2.3 ± 0.1	52 ± 3	2.9 ± 0.1	327 ± 2	16.1 ± 0.7	47 ± 3	2002 Aug - 2014 Jun
GRACE-OBP-Swenson	1.9 ± 0.1	65 ± 4	1.9 ± 0.1	53 ± 3	2.5 ± 0.1	319 ± 2			2002 Aug - 2014 Jun
INV (Rietbroek et al., 2012b) 1	3.0	18	2.1	56	3.4	327			2003 Jan - 2008 Dec
INV (Rietbroek et al., 2012b) 2	2.2	31	2.0	63	3.4	326			2003 Jan - 2008 Dec
INV (Rietbroek et al., 2016)	3.5 ± 0.1	66 ± 3	2.2 ± 0.1	58 ± 2	2.7 ± 0.1	325 ± 2			2002 Aug - 2014 Jun
(Wu et al., 2015) 1	3.9 ± 0.1	21 ± 1	2.1 ± 0.1	45 ± 1	2.7 ± 0.1	321 ± 1			2002 Apr - 2009 Apr
(Wu et al., 2015) 2	3.3 ± 0.1	22 ± 3	1.9 ± 0.1	54 ± 2	2.6 ± 0.1	322 ± 1			2002 Apr - 2009 Apr
(Wu et al., 2015) 3	3.5 ± 0.1	19 ± 1	1.9 ± 0.1	52 ± 1	3.0 ± 0.1	337 ± 1			2002 Apr - 2009 Apr
SLR (Cheng et al., 2013b)	4.2 ± 0.3	33 ± 2	2.9 ± 0.4	49 ± 4	2.7 ± 0.1	339 ± 2			2002 Aug - 2014 Jun
SLR (Cheng et al., 2013a)							14.1 ± 0.7	53 ± 3	2002 Aug - 2014 Jun

Antarctica. On the other hand, the zonal degree-1 and -2 spherical harmonics in the northern polar region are of the same sign. This means that a positive error in the C_{10} coefficient can be largely compensated by a negative error in the C_{20} coefficient and vice versa. Thus, these errors must show a strong anti-correlation.

5.6. Which Degree-1 and C_{20} Solution should be Used for Estimating Mass Variations?

Independent estimates of degree-1 and C_{20} coefficients are typically used to correct GRACE solutions in order to obtain more accurate estimates of surface mass anomalies. However, owing to the lack of an accurate reference regionally or globally, it is difficult to quantify the added value of this correction. GRACE users often adopt a specific solution without justification for their choice. In this section, we offer a simple way to evaluate the quality of degree-1 and C_{20} coefficients. GRACE GSM solutions are used to estimate mass variations within particular regions where the mass variations are known to be minor, namely East Antarctica and the Sahara Desert (e.g. Helsen et al., 2008; Liu et al., 2010). These regions are used as validation areas. We estimate mass anomaly time-series there, using the GRACE solutions corrected with different estimates of degree-1 and C_{20} time-series. The best degree-1 and C_{20} time-series should result in the smallest mass variations over the selected validation areas. Note that the mass anomalies over validation areas at different geographic locations may not be sensitive to all the coefficients. It is thus important to select several well-separated regions.

We have prepared 7 versions of GRACE solutions by using different combinations of degree-1 and C_{20} coefficients:

(i) **Ori GRC**: Original GRACE CSR RL05 solutions as they are. That is, zero degree-1 coefficients and the native GRACE C_{20} are adopted.

(ii) **SLRDeg1 + SLRC20**: GRACE solutions complemented with SLR-based degree-1 (Cheng et al., 2013b) and C_{20} coefficients (Cheng et al., 2013a).

(iii) **INVDeg1 + SLRC20**: GRACE solutions corrected with degree-1 coefficients based on the joint inversion approach (Rietbroek et al., 2016) (https://doi.pangaea.de/10.1594/PANGAEA.855539) and SLR C_{20} coefficients.

(iv) **SWEDeg1 + SLRC20**: GRACE solutions complemented with degree-1 coefficients based on the GRACE-OBP-Swenson approach (Swenson et al., 2008); C_{20} coefficients are based on SLR data . This is the traditionally used approach.

(v) **CMBDeg1 + CMBC20**: GRACE solutions corrected with the degree-1 and C_{20} coefficients provided by the combination approach.

(vi) **CMBDeg1 + SLRC20**: GRACE solutions corrected with the degree-1 coeffi-

cients provided by the combination approach and SLR C_{20} coefficients.

(vii) **GODeg1 + GOC20**: GRACE solutions corrected with the degree-1 coefficients and C_{20} provided by the GRACE-OBP-Improved approach (Sun et al., 2016b).

It should be noted that we have also used a filtered GRACE solution based on DDK-4 (Kusche et al., 2009). Besides, multiple sub-regions are selected as validation areas in each of two places. However, the results are very similar and thus we show the results based on one of the areas. The linear trends in the resultant mass transport time-series are subject to large uncertainties and are not comparable. The linear trends in SLR-based degree-1 coefficients reflect merely drifting errors with respect to the origin of the International Terrestrial Reference Frame (ITRF). Degree-1 solutions from other considered approaches involve the use of a GIA model. However, the adopted GIA models are different and all contain large uncertainties. Therefore, trends and seasonal variations in the resulting mass transport time-series must be assessed independently. Here, we will focus on the seasonal variations (Sect. 5.6.1 and 5.6.2). The quality of the trend estimates in our degree-1 and C_{20} solutions are not assessed in the following experiments. Nevertheless, we show the resulting trend estimates in the mass transport time-series over both validation areas (Sect. 5.6.3). These trend estimates are obtained based on the assumption that the GIA model provided by A et al. (2012) is error-free. It is worth noting that under such an assumption, the combination approach, which is a generalised GRACE-OBP-Improved approach, should be able to recover the true linear trends in the degree-1 and C_{20} time-series Chapter 4.

5.6.1. Mass Variations in East Antarctica

There are no physical processes that cause large mass variations in the interior of East Antarctica (Helsen et al., 2008). Therefore, the GRACE solution augmented with the optimal degree-1 and C_{20} estimates should result in the minimal mass variations. However, one should bear in mind that mass anomalies in this region are sensitive to only the zonal coefficients, i.e. C_{10} and C_{20}.

In the background of Fig. 5.12a, we show the RMS mass anomaly based on the solution from the combination approach in the considered time interval (2002 - 2014). One of the tested regions (or validation areas) in this area is indicated in the panel with a red polygon. All variants of GRACE solutions are employed to estimate the total mass variations within the validation area, and the resulting RMS estimates of the de-trended mass variation time-series (as a function of the truncation degree) are shown in Fig. 5.12b.

It can be seen that the RMS value of the mass variation time-series based on the original GRACE solution (**Ori GRC**) is about 0.9 cm. It reduces by more than 50% when we use **INVDeg1 + SLRC20**, and is further reduced if we apply the **SWEDeg1 + SLRC20** or **CMBDeg1 + CMBC20**. Results based on the later solution is improved

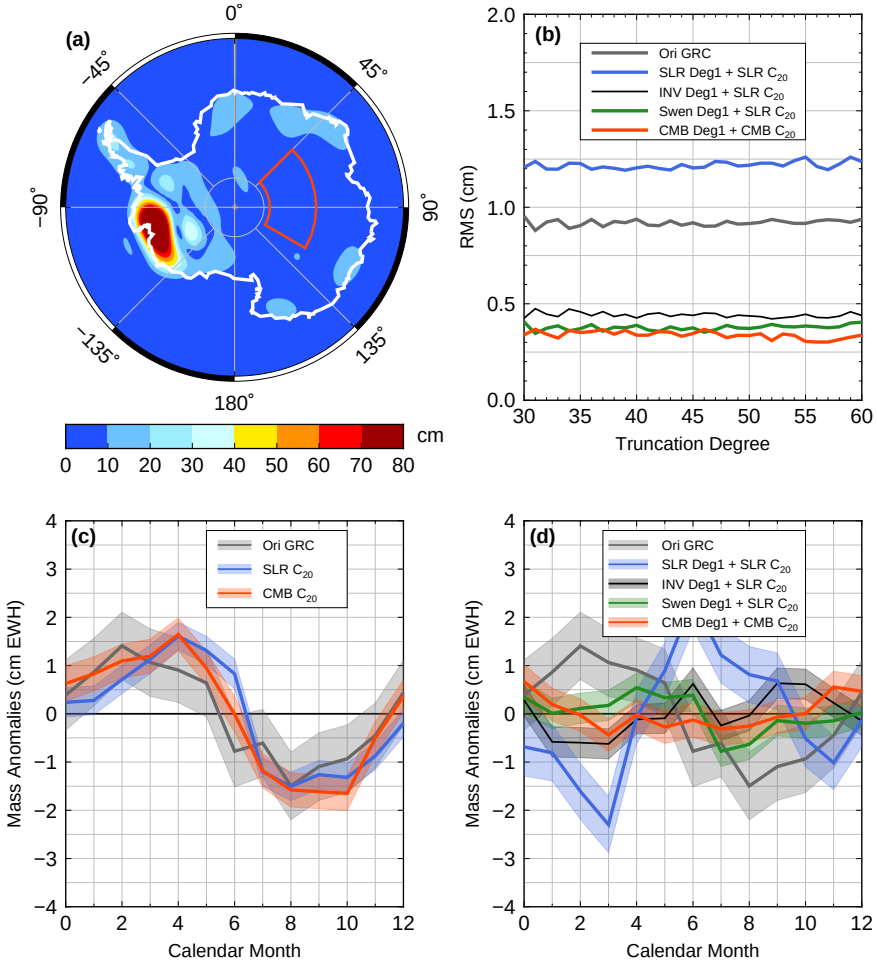

Figure 5.12: Mass variations in the validation area at East Antarctica. In panel a, we show the signal RMS in terms of equivalent water heights. The study area is indicated with a red polygon ($45^\circ E/120^\circ E/76^\circ S/84^\circ S$). Panel b shows RMS values of mass anomaly time-series as a function of truncation degree. Panel c and d show the mean mass anomaly per calendar month. The shadowed color bands indicates the spread of the monthly mass anomalies. Note that the calendar month 0 represents December of the previous year. In panel c, we show the results based on the GRACE solutions after replacing the C_{20} coefficients with those from independent approaches. In panel d, we show results when the GRACE solutions are further complemented with degree-1 coefficients based on different approaches.

Table 5.2: RMS of mass anomaly (integrated over validation areas) obtained by averaging the corresponding time-series. In this table, we intend to show explicitly the numbers based on four solutions, namely **Ori GRC**, **CMBDeg + CMBC20**, **CMBDeg1 + SLRC20** and **GODeg1 + GOC20** for a truncation degree of 50. See Sect. 5.6 for the meaning of abbreviations in the first column.

GRACE solutions	East Antarctic (cm)	Sahara Desert (cm)
Ori GRC	0.92	0.78
CMBDeg1 + CMBC20	0.33	0.35
CMBDeg1 + SLRC20	0.34	0.39
GODeg1 + GOC20	0.29	0.31

by about (10 20%) compared to that based on the traditional approach. In contrast, using **SLRDeg1 + SLRC20** worsen the results by about 20%. For clarity, results based on **CMBDeg1 + SLRC20** as well as **GODeg1 + GOC20** are not shown in the figure as they are very close to the **CMBDeg1 + CMBC20**, but the corresponding resultant RMS values of the time-series is documented in Tab. 5.2. We will discuss the results later in section 5.7.

Note that the truncation degree of the GRACE solution (between 30 and 60) obviously plays a minor role in the RMS estimates, which implies that the validation area is large enough to ensure a cancellation of random errors in high-degree coefficients.

Subsequently, we calculate the mean mass anomaly per calendar month and show the effect of replacing C_{20} and adding degree-1 coefficients in panels c and d, respectively. In the **Ori GRC** case, a clear seasonal pattern is revealed. Replacing the original C_{20} coefficients with those from SLR data and the combination approach show some differences but does not significantly change the seasonal pattern (Fig. 5.12c). Such a seasonal pattern can thus be attributed to either the absence of the degree-1 coefficients or errors in higher-degree coefficients. However, the total mass variations of the validation area are obtained by integrating all data points within the area. Mass anomalies due to high-degree errors are random and would unlikely show a seasonal pattern. Also, as previously showed (Fig. 5.12b), increasing the truncation degree does not significantly change the RMS estimates of the mass transport time-series. This is an indication that the errors in high-degree coefficients indeed largely cancel each other. Further more, different validation areas in East Antarctica are employed, but the revealed seasonal pattern is quite consistent. This contradicts to the nature of high-degree errors as their impact changes quickly from location to location. Therefore, we believe that the observed season pattern is likely due to the lack of the degree-1 coefficients. Indeed, once the GRACE solutions are complemented with proper estimates of degree-1 coefficients (based on the joint inversion approach, GRACE-OBP-Swenson approach, or the combination approach), the seasonal pattern significantly reduces or disappears (Fig. 5.12d). Remarkably, after using degree-1 solutions from SLR, the resulting seasonal pattern

is in anti-phase, as compared to the one produced without degree-1 coefficients.

5.6.2. Mass Variations in the Sahara Desert

We further conduct a similar analysis for validation areas in the Sahara Desert, another place with minimal mass variations. Validation areas in this region should allow us to check the quality of the tesseral coefficients, and in particular of C_{11} coefficient among the four estimated coefficients, as the surface spherical harmonic of degree 1 and order 0 reaches maximum in that area, exceeding the other three surface spherical harmonic under consideration.

In Fig. 5.13, we show the considered validation area (indicated with a red polygon in panel a). The resulting RMS value of the mass variation time-series based on various version of GRACE solutions are shown in panel b. This time, we notice that **SWEDeg1 + SLRC20** is able to reduce the RMS value by about 50%. **INVDeg1 + SLRC20** and **CMBDeg1 + CMBC20** manage to further reduce the RMS estimates by about 0.1 cm. On the other hand, **SLRDeg1 + SLRC20** worsen the results significantly.

A clear seasonal pattern reveals itself in the mass variation time-series based on the **Ori GRC** (Fig 5.13c). Switching C_{20} coefficient between different variants barely changes the resultant seasonal pattern. This is expected because the zonal degree 2 surface spherical harmonic at the latitude of 22.5° is only 30% of the values at the poles. Adding the degree-1 coefficients based on the GRACE-OBP-Swenson, joint inversion or the combination approach to the GRACE solutions reduces the annual amplitude of the seasonal pattern (Fig. 5.13d). When using the SLR-based degree-1 coefficients, we end up having an even more prominent seasonal pattern, which again, is in anti-phase with the original one.

5.6.3. Trend Estimates in Mass Transport Time-series

In Tab. 5.3, we show the linear trend estimates extracted from different mass transport time-series for both validation areas. Notice that the GIA contributions are cleaned from all variants of the GRACE solutions, including both low- (degree-1 and C_{20}) and high-degree coefficients. Therefore, the obtained trend estimates should reflect the present-day mass transport rates. The large discrepancy between these trend estimates suggests the large uncertainty in GIA models (e.g. Klemann and Martinec, 2011; A et al., 2012).

5.7. Conclusions and Discussion

We have developed a combination approach for a statistically-optimal estimation of degree-1 and C_{20} coefficients. We have also shown that the combination approach

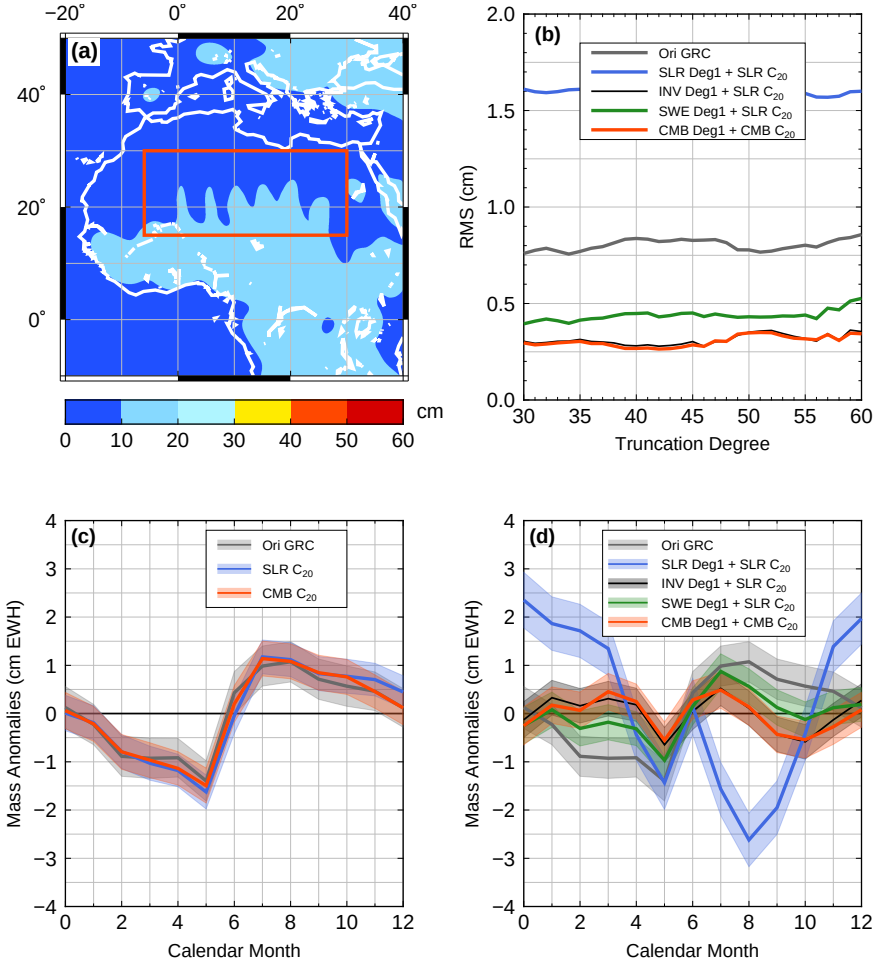

Figure 5.13: Same as Fig. 5.12, but showing mass transport in the validation area at the Sahara Desert ($6°W/30°E/15°N/30°N$).

Table 5.3: Estimates of linear trends in the resulting mass transport time-series (Aug 2002 - Jun 2014). See Sect. 5.6 for the explanation of the names in the first column. Note that the degree-1 solution denoted by **INVDeg1**. These degree-1 coefficients are associated with surface load only and the modeled GIA signals are not restored. In the last two rows, we also show the results after restore GIA signals to the GRACE solutions.

GRACE solutions	East Antarctic (cm/yr)	Sahara Desert (cm/yr)
Ori GRC	-0.58 ± 0.06	0.11 ± 0.04
SWEDeg1 + SLRC20	0.00 ± 0.03	-0.10 ± 0.03
INVDeg1 + SLRC20	0.10 ± 0.03	-0.08 ± 0.03
GODeg1 + GOC20	-0.39 ± 0.03	0.05 ± 0.03
CMBDeg1 + CMBC20	-0.45 ± 0.03	0.11 ± 0.03
GODeg1 + GOC20 GIA restored	0.14 ± 0.03	0.04 ± 0.03
CMBDeg1 + CMBC20 GIA restored	0.08 ± 0.03	0.10 ± 0.03

is a generalization of the GRACE-OBP approach proposed by Swenson et al. (2008) and improved by Sun et al. (2016b). If GRACE data are free of noise, whereas noise in OBP data is white, then the combination approach reduces to the GRACE-OBP-Improved approach.

Based on the numerical experiments, we find that the overall quality of the resultant degree-1 and C_{20} time-series can be largely improved (RMS errors are reduced by about 30%) by taking into account the stochastic information of noise in the input datasets. Degree-1 and C_{20} coefficients based on real data are then computed. The obtained annual variations are similar to those of other approaches. However, we do notice that the annual amplitude of the SLR C_{10} time-series is about 1 mm larger than our estimates as well as many others. The annual phase of our C_{10} coefficients is more than a month later than the SLR- and GPS-derived solutions (Rietbroek et al., 2012b; Wu et al., 2015; Cheng et al., 2013b) but close to the solution based on GRACE and altimetry data (Rietbroek et al., 2016). Error estimates and the correlation coefficients are also important product of the proposed approach. Remarkably, they are provided not as constant numbers, but as time-series.

To validate the resulting degree-1 and C_{20} coefficients, we selected two validation areas with minimal mass variations (central East Antarctica and Sahara Desert). Those areas are used to compare estimates of surface mass anomalies obtained from GRACE solutions corrected with 7 different combinations of degree-1 and C_{20} coefficients in estimating surface mass anomalies. It should be noted that the mass anomalies in the selected validation areas are relatively insensitive to the S_{11} coefficients. Fortunately, seasonal signals in the S_{11} time-series are the most consistent (among the three degree-1 coefficients) between the results from different techniques (Tab. 5.1). This is likely because the S_{11} coefficient (or the Y component of the geocenter motion), is well controlled by spatial variations of mass and gravity

field at non-polar areas centered at 90° and 270° longitudes, and those areas are relatively well represented in the networks of both SLR and GPS stations.

Even though the annual amplitude of the C_{10} time-series based on Swenson et al. (2008) is reported to be small, it results in reasonable surface mass anomaly estimates. In contrast, the SLR-based degree-1 coefficients (Cheng et al., 2013b) are not sufficiently accurate for estimating surface mass anomalies. Probably, the annual amplitude is overestimated and the annual phase is wrongly estimated. This finding is consistent with the fact that SLR-based estimates are relatively inaccurate in the estimation of the C_{10} and C_{11} coefficients due to a poor quality of tropospheric corrections, too few ground stations in polar areas, and the absence of stations over oceans.

Contradictory to the numerical results, the degree-1 and C_{20} solutions from the GRACE-OBP-Improved approach (**GODeg1 + GOC20**) performs slightly better (about 10%) than that based on the proposed approach in terms of the resulting RMS values of the mass transport time-series. The reasons are still under investigation.

By switching from the C_{20} solutions based on the combination approach to those obtained with the SLR technique (while applying the same degree-1 solution based on the combination approach), we find a marginal difference (about 10%) in the resultant RMS value of the mass transport time-series. This is an indication that our C_{20} time-series and the SLR-based one are of similar quality.

As far as the future developments are concerned, the combination approach will benefit from improvements in the input datasets. Future OBP models will likely be more accurate. More realistic covariance matrices for OBP noise will further enhance the advantage of this approach. In order to also address the linear trends in degree-1 and C_{20} coefficients, a better way of dealing with the solid Earth signals is warranted. Until now, those signals are accounted for with a GIA model, which is assumed to be free of errors. However, large uncertainties in GIA modelling and the fact that tectonic signals are ignored (e.g., due to mega-thrust earthquakes) could substantially affect the trend estimates in the low-degree coefficients.

Finally, our products are publicly available at http://www.citg.tudelft.nl/deg1c20).

6

Conclusions and Recommendations

Here, we highlight the most important findings and products of this thesis and draw conclusions for each research objective. Finally we outline a number of recommendations for future studies.

6.1. Conclusions

6.1.1. Observed Changes in the Earth's Dynamic Oblateness from GRACE Data and Geophysical Models

As a starting point of our research, we have implemented the methodology proposed by Swenson et al. (2008), who produce geocenter motion estimates based primarily on GRACE data and OBP models. The resulting estimates are prevalently used in the GRACE community to complement the monthly GRACE gravity field solutions with degree-1 spherical harmonic coefficients in order to ensure a more accurate estimation of mass transport. We have extended the original Swenson's methodology to co-estimate the C_{20} coefficients simultaneously. We also demonstrated that GRACE data at higher spherical harmonic degrees combined with OBP estimates are capable of estimating seasonal changes in C_{20} to a level comparable with SLR solutions. This is a significant improvement considering that the C_{20} coefficients in original GRACE solutions are corrupted by large aliases due to the temperature related systematic errors in satellite accelerometers.

We showed that two implementation parameters are the main factors controlling the annual amplitude of seasonal signals and trend in the C_{20} time-series. The first one is represented by the inclusion or exclusion of ocean data points in coastal areas, which are contaminated by continental signal leakage. A simple approach of reducing the size of the ocean function to exclude a few hundreds of kilometers of coastal waters is capable of producing a solution that is in close agreement with SLR results. The other consisted in how to deal with the exchanged water between ocean and land. Distributing them over the oceans as a uniform layer like described in Swenson et al. (2008) results in sub-optimal C_{20} estimates. Instead, the passive response of the ocean water due to self-attraction and loading (SAL) effects has to be taken into account as it also significantly affects the annual amplitude and long-term trend of the C_{20} time-series.

The availability of independent SLR solutions has allowed us to benchmark the proposed methodology. However, the SLR-derived C_{20} time-series are not free of systematic errors and noise. The implementation parameters (a 150 km buffer width and taking into account SAL effects) tuned to achieve a time series that best fit the SLR solution may be not represent the best possible choice.

6.1.2. Optimizing Estimates of Annual Variations and Trends in Geocenter Motion and Earth's Dynamic Oblateness

We have conducted an end-to-end simulation study to test the performance of the GRACE-OBP approach. The updated ESA Earth System Model (ESM) (Dobslaw et al., 2015) is employed to simulate "true" signals similar to those contained in the GRACE-based GSM solutions. Realistic GRACE random errors were simulated based on real GRACE full error covariance matrices are added to the "true" signals. Errors in the OBP estimates provided by the ESM are exploited. Such errors are estimated from a small ensemble of four different atmospheric and oceanic models. Our simulation results suggested that the GRACE-OBP approach is capable of accurately estimating variations in geocenter and the Earth's dynamic oblateness.

The choice of the implementation parameters including buffer width and SAL effects are proved to be important for both degree-1 and C_{20} coefficients. As far as signal leakage in coastal areas in concerned, the best results are obtained when ocean data points within 200 km from the coastline are discarded. Moreover, SAL effects need to be taken into account. Finally, high-frequency noise in the GRACE solutions can best be dealt with by truncation of the sets of input spherical harmonic coefficients. The optimal truncation degree is between 30 and 50 (differences caused by using truncation degrees within this range is within 2σ), which is high enough to infer redistributing masses that are significant for estimates of the continental degree-1 and C_{20} variations, and yet low enough to avoid the large errors in high-degree spherical harmonic coefficients.

The optimal choice of the implementation details is somehow different for each of the four coefficients (C_{10}, C_{11}, S_{11} and C_{20}) analyzed and for different quantities of interest such as the amplitude/phase of annual variations, the long-term trend and the time-series itself. Nevertheless, we found it essential to identify a single setup in order to ensure a consistency of the obtained estimates. The recommended setup consists of truncation of monthly GRACE solutions at degree 45, a buffer width of 200 km, and inclusion of SAL effects.

The second part of this study dealt with real data processing, where we demonstrated that the resulting degree-1 and C_{20} solutions have similar dependence on the implementation parameters as in the synthetic data case. This knowledge allowed us to use the optimal implementation parameter setting from the simulation study. Notably, the annual amplitude of the GSM-like C_{10} time-series is about 50% larger than that reported in Swenson et al. (2008). Such a dramatic amplification makes the annual amplitude in the C_{10} time-series comparable with those derived based on other geodetic techniques, such as SLR and global GPS inversion.

Errors in both GRACE coefficients and the oceanic degree-1 and C_{20} coefficients from the OBP model contribute to the uncertainties in the obtained degree-1 and C_{20} time-series. GRACE errors account for annual amplitude errors in geocenter motion of less than 10% of the total signal (at the 0.1 mm level). A similar statement

applies also to C_{20} variations. GRACE error also has minor effects (less than 3 days) on the annual phase estimates of both degree-1 and C_{20} variations. On the other hand, errors in oceanic degree-1 and C_{20} coefficients seem to play a somewhat larger role. By comparing estimates based on different OBP models, we concluded that the errors in oceanic degree-1 coefficients account for up to 15% errors in the annual amplitude estimates of degree-1 variations. Moreover, errors in oceanic C_{20} coefficients could cause a difference of about 20% in the annual amplitude estimates of C_{20} variations. Annual phase estimates, on the other hand, are not significantly affected (less than 2 weeks).

The fundamental assumption of the GRACE-OBP approach is that both GRACE and OBP data are error-free and treated as deterministic values. Therefore, the errors in these two data sets are erroneously considered as signals in degree-1 and C_{20} coefficients. In the next study, we take into account the errors in both datasets and estimate the degree-1 and C_{20} coefficients in a statistically optimal sense.

6.1.3. Statistically Optimal Estimation of Geocenter Motion and Changes in the Earth's Dynamic Oblateness

In this part of our research, we estimated degree-1 and C_{20} coefficients supplied with error estimates from a statistically optimal data combination of GRACE data and modeled OBP estimates. We proved that such a combination approach is essentially a general form of the GRACE-OBP approach. The combination approach reduces to the GRACE-OBP approach if the GRACE data are free of noise and the OBP data only contain white noise.

The combination approach is verified with a simulation study. In numerical experiments, the overall quality of the resultant degree-1 and C_{20} time-series can be largely improved (by about 30%) by taking into account the stochastic information of noise in the input data sets. In the case of real data processing, the annual variations of the degree-1 and C_{20} coefficients are similar to those from the GRACE-OBP approach and those from other approaches (e.g. joint inversion approach by Rietbroek et al. (2009, 2012b)). On the other hand, the annual amplitude of the C_{10} time-series is by about 1 mm (30%) smaller than SLR estimates. Also, the annual phase of our C_{10} time-series is by more than a month delayed, as compared to the SLR- and GPS-derived solutions. Error variances and covariances of the resulting coefficients are also important product of this research. The formal errors of the spherical harmonic coefficients are different per coefficient and vary with time. The correlations between the coefficients are generally small except for a strong anti-correlation (at the level of -0.3) between the C_{10} and C_{20} coefficients. This is due to the lack of OBP estimates over the southern polar area where the corresponding surface spherical harmonic functions are of the opposite sign.

To perform an independent validation of the obtained time-series. Areas with minor mass transport were selected: central part of East Antarctica and Sahara

Desert. We augmented monthly GRACE solutions with different estimates of degree-1 and C_{20} coefficients. Accurate estimates of those coefficients should result in minimal mass variations over the selected validation areas. It is worth noting that the mass transport time-series in the selected two validation areas are relatively insensitive to variations of the S_{11} coefficients. However, seasonal signals in the S_{11} time-series are the most consistent (among the three degree-1 coefficients) between the results from different techniques, suggesting a relatively small uncertainty in this coefficient.

Even though the annual amplitude of the C_{10} time-series based on Swenson et al. (2008) is likely underestimated, it results in comparable surface mass anomaly estimates compared to those from the combination approach. In contrast, the SLR-based degree-1 coefficients (Cheng et al., 2013b) are not sufficiently accurate in estimating surface mass anomalies. We conclude that the SLR solutions are less accurate: the annual amplitude is overestimated there and the annual phase is offset by more than a month.

By using the C_{20} solutions based on the combination approach instead of those obtained with the SLR technique (while applying the same degree-1 solution based on the combination approach), we find a marginal difference (about 10%) in the resultant RMS value of the mass transport time-series. This is an indication that our C_{20} and the SLR-based time-series are of a similar quality.

6.2. Recommendations

According to (Wu et al., 2017), the degree-1 coefficients to be combined with monthly GRACE gravity field solutions when inferring surface mass variations requires geocenter motion accuracy goals of 0.2 mm for annual amplitude and 0.02 mm yr^{-1} for velocity. For example, this would cause a uncertainty in mass transport estimates over Antarctica of about 20 gigaton for annual amplitude and 2 gigaton yr^{-1} for velocity (Wu et al., 2012). Comparing the latest inversion results, the differences between their annual amplitude estimates are at approximately 0.5 mm, 0.3 mm and 1 mm level for X-, Y- and Z-components, respectively. The uncertainties in trend estimates for all components are still not able to be reliably quantified due to the dependence on a GIA model. Therefore, we recommend the following studies to improve further the estimation of degree-1 and C_{20} coefficients.

6.2.1. Determination of Long-term Linear Trend

GRACE observes gravity changes that are associated with mass transport both at the surface and in the interior of the solid Earth. However, the methodology we have adopted in this thesis requires the removal of the time-varying solid Earth signals. This has been done by subtracting the predictions by a specific GIA model.

By doing this, we assume 1) other solid Earth signals, such as those due to mega-thrust earthquakes, are negligible contributors to the very low degree coefficients, and 2) the adopted GIA model is free of errors. However, the first assumption is not necessarily true and the second one is certainly not true.

Solid Earth signals exerted due to mega-thrust earthquakes are detectable in GRACE data. Although their effects are now shown to be secondary compared to those of GIA, the presence of them in GRACE data may affect the linear trend estimates in low-degree coefficient time-series. Therefore, it is suggested to quantify the effects of the solid Earth signals due to mega-thrust earthquakes with available models (Han et al., 2006).

Due to the limited availability of observational constraints, GIA models are characterized by large uncertainties. A wider range of GIA models need to be investigated because it is unlikely that GIA models allow for producing robust degree-1 and C_{20} trend estimates. By doing that, we are able to test the sensitivity of the final solutions with respect to the choice of GIA models. However, this does not help estimating the trends more accurately as it is not possible to identify the best GIA model. Therefore, a better way would be to co-estimate GIA signals in order to avoid the use of a GIA model.

6.2.2. Definition of the Ocean Function

The methodologies we have developed and applied require an ocean function to partition the Earth's surface into the land and ocean areas. We found that in order to obtain accurate oceanic mass anomalies from GRACE data, it is crucial to reject coastal areas that are polluted by signal leakage from land due to the limited resolution of the GRACE data. Currently, we simply reduce the size of the ocean areas so that ocean points within a few hundred kilometers from land are removed. We call the zone between land and the newly defined ocean area a buffer zone. So far, the buffer zone has a uniform buffer width. Although the ocean function defined this way is effective to recover the true signal in the degree-1 and C_{20} coefficients, it may be further improved by using a buffer width varying spatially with the signal leakage. That is, the buffer width is larger if strong signal leakage appears and smaller if the signal leakage is minor. Compared to a uniform buffer width, the ocean function defined this way may allow one to include as many as possible uncontaminated oceanic data points, and improve this way the final results.

Besides the ocean areas, there are land regions with minor (i.e., known) mass anomalies. These regions, such as the Sahara desert and east Antarctica may also be included to provide further constraint on the solutions.

6.2.3. Statistically Correct Way of Combining Independently Estimated C_{20} Coefficient with Existing GRACE Monthly Gravity Field Solution

It is well-known that the C_{20} coefficients of the monthly GRACE gravity field solutions are corrupted by temperature related systematic error of the GRACE accelerometer (Cheng and Ries, 2017). Therefore, it is necessary to update the original C_{20} values with more accurate ones in order to obtain more accurate surface mass transport estimates. Currently, it is a common practice to replace the original values with those from other geodetic techniques, such as SLR (Cheng et al., 2013a). Such a procedure, though prevalently used, is statistically wrong. Due to the correlations between C_{20} and other coefficients, changing C_{20} should also lead to a change of other coefficients.

Since the full noise variance-covariance matrices of GRACE monthly solutions are now available and the C_{20} as well as its noise variance can be obtained from the method introduced in Chapter 5, we propose to combine them through the partitioned model of least-squares (Teunissen, 2000). In this way, one could not only update the original C_{20} coefficients with better estimates, but also update all other coefficients simultaneously according to the correlation structure provided by the GRACE full noise variance-covariance matrices. Finally, updated full noise variance-covariance matrices would also be obtained.

A

Appendix

A.1. General Form of Data Combination

$$\mathbf{d}_c = \Big(\sum_{n=1}^{N} \mathbf{A}_n^T \mathbf{C}_n^{-1} \mathbf{A}_n \Big)^{-1} \cdot \sum_{n=1}^{N} \mathbf{A}_n^T \mathbf{C}_n^{-1} \mathbf{d}_n, \tag{A.1}$$

where N is the number of available data sets, $\mathbf{A}_n$ are design matrices and $\mathbf{C}_n$ are the noise variance-covariance matrices describing errors in the exploited data sets d_n.

A.2. Explicit Form of Equation (20)

In Eq. (5.20), $\mathbf{Y}^{'}$ is a $K \times 4$ matrix that can be written explicitly as

$$\mathbf{Y}^{'} = \begin{bmatrix} P_{10}(\cos\theta_1) & P_{11}(\cos\theta_1)\cos\phi_1 & P_{11}(\cos\theta_1)\sin\phi_1 & P_{20}(\cos\theta_1) \\ P_{10}(\cos\theta_2) & P_{11}(\cos\theta_2)\cos\phi_2 & P_{11}(\cos\theta_2)\sin\phi_2 & P_{20}(\cos\theta_2) \\ \vdots & \vdots & \vdots & \vdots \\ P_{10}(\cos\theta_K) & P_{11}(\cos\theta_K)\cos\phi_K & P_{11}(\cos\theta_K)\sin\phi_K & P_{20}(\cos\theta_3) \end{bmatrix}, \tag{A.2}$$

where θ and ϕ are the colatitude and longitude at point k, respectively.

Therefore, $\mathbf{Y}^{'T}\mathbf{O}\mathbf{Y}^{'}$ becomes a 4×4 matrix

$$\mathbf{Y}'^{T}\mathbf{O}\mathbf{Y}' = \begin{bmatrix} I_{10C}^{10C} & I_{11C}^{10C} & I_{11S}^{10C} & I_{20C}^{10C} \\ I_{10C}^{11C} & I_{11C}^{11C} & I_{11S}^{11C} & I_{20C}^{11C} \\ I_{10C}^{11S} & I_{11C}^{11S} & I_{11S}^{11S} & I_{20C}^{11S} \\ I_{10C}^{20C} & I_{11C}^{20C} & I_{11S}^{20C} & I_{20C}^{20C} \end{bmatrix}, \tag{A.3}$$

where, the following notation is used

$$\begin{aligned} I_{11C}^{10C} &= \int d\Omega P_{10}(\cos\theta)\vartheta(\theta,\phi)P_{11}(\cos\theta)\cos\phi \\ I_{11S}^{11C} &= \int d\Omega P_{11}(\cos\theta)\cos\phi\vartheta(\theta,\phi)P_{11}(\cos\theta)\sin\phi \\ &\text{Other elements are similarly defined.} \end{aligned} \tag{A.4}$$

Clearly, $\mathbf{Y}'^{T}\mathbf{O}\mathbf{h}$ is composed of the oceanic degree-1 and C_{20} coefficients C_{10}^{ocean}, C_{11}^{ocean}, S_{11}^{ocean} and C_{20}^{ocean}.

Finally, we have

$$\mathbf{Y}'^{T}\mathbf{O}\mathbf{h}_g = \begin{bmatrix} \int d\Omega P_{10}(\cos\theta)\vartheta(\theta,\phi)\mathbf{h}_g \\ \int d\Omega P_{11}(\cos\theta)\cos\phi\vartheta(\theta,\phi)\mathbf{h}_g \\ \int d\Omega P_{11}(\cos\theta)\sin\phi\vartheta(\theta,\phi)\mathbf{h}_g \\ \int d\Omega P_{20}(\cos\theta)\vartheta(\theta,\phi)\mathbf{h}_g \end{bmatrix} = \begin{bmatrix} -G_{10C} \\ -G_{11C} \\ -G_{11S} \\ -G_{20C} \end{bmatrix} \tag{A.5}$$

B

Appendix

B.1. Basic Ideas of the Approach by *Ditmar et al. (2017)* for the Quantification of Random Noise in a Data Time-series

That approach is based on the assumptions that (i) true signal in the data time-series is close (but not necessarily equal) to a combination of an annual periodic signal and a linear trend; (ii) noise in the time-series is uncorrelated and (optionally) non-stationary; (iii) time-series of noise variances is known up to a constant multiplier (scaling factor). Then, the data time-series is approximated by a regularized one on the basis of a properly designed regularization functional ($\Omega[H]$):

$$\Omega[H] = \sum_{k=1}^{K-1} (h_{k+1}(t) - h_k(t))^2 dt, \tag{B.1}$$

where K is the total number of years considered and $h_k(t)$ is by definition the mass anomaly in the k-th year; $h_{k+1}(0) = h_k(1)$ due to the continuity of $H(t)$.

The optimal regularization parameter is estimated with the Variance Component Estimation (VCE) technique (Koch and Kusche, 2002), which includes the proper scaling of the provided noise variances. Then, the time-series of scaled noise variances is the measure of actual random noise in the considered data.

References

A, G., Wahr, J., and Zhong, S. (2012). Computations of the viscoelastic response of a 3-D compressible Earth to surface loading: an application to Glacial Isostatic Adjustment in Antarctica and Canada. *Geophysical Journal International*, 192(2):557–572.

Altamimi, Z., Boucher, C., and Willis, P. (2005). Terrestrial reference frame requirements within GGOS perspective. *Journal of Geodynamics*, 40(4):363–374.

Altamimi, Z. and Collilieux, X. (2010). Quality Assessment of the IDS Contribution to ITRF2008. *Advances in Space Research*, 45(12):1500–1509.

Altamimi, Z., Collilieux, X., and Métivier, L. (2011). ITRF2008: an improved solution of the international terrestrial reference frame. *Journal of Geodesy*, 85(8):457–473.

Altamimi, Z., Rebischung, P., Métivier, L., and Collilieux, X. (2016). ITRF2014: A new release of the International Terrestrial Reference Frame modeling nonlinear station motions. *Journal of Geophysical Research: Solid Earth*, 121(8):2016JB013098.

Benjamin, D., Wahr, J., Ray, R. D., Egbert, G. D., and Desai, S. D. (2006). Constraints on mantle anelasticity from geodetic observations, and implications for the J2 anomaly. *Geophysical Journal International*, 165(1):3–16.

Bergmann-Wolf, I., Zhang, L., and Dobslaw, H. (2014). Global Eustatic Sea-Level Variations for the Approximation of Geocenter Motion from Grace. *Journal of Geodetic Science*, 4(1).

Bettadpur, S. (2012). UTCSR Level-2 Processing Standards Document. Technical Version 4, Univ. Texas, Austin.

Blewitt, G. (2003). Self-consistency in reference frames, geocenter definition, and surface loading of the solid Earth. *Journal of Geophysical Research: Solid Earth*, 108(B2):2103.

Blewitt, G., Heflin, M. B., Webb, F. H., Lindqwister, U. J., and Malla, R. P. (1992). Global coordinates with centimeter accuracy in the International Terrestrial Reference Frame using GPS. *Geophysical Research Letters*, 19(9):853–856.

Blewitt, G., Lavallée, D., Clarke, P., and Nurutdinov, K. (2001). A new global mode of Earth deformation: seasonal cycle detected. *Science (New York, N.Y.)*, 294(5550):2342–2345. 00167 PMID: 11743198.

Bouillé, F., Cazenave, A., Lemoine, J. M., and Crétaux, J. F. (2000). Geocentre motion from the DORIS space system and laser data to the Lageos satellites: comparison with surface loading data. *Geophysical Journal International*, 143(1):71–82. 00000.

Bourda, G. (2008). Length-of-day and space-geodetic determination of the Earth's variable gravity field. *Journal of Geodesy*, 82(4-5):295–305.

Cazenave, A. and Nerem, R. S. (2002). Redistributing Earth's Mass. *Science*, 297(5582):783–784.

Chambers, D. P. and Schröter, J. (2011). Measuring ocean mass variability from satellite gravimetry. *Journal of Geodynamics*, 52(5):333–343.

Chambers, D. P., Wahr, J., and Nerem, R. S. (2004). Preliminary observations of global ocean mass variations with GRACE. *Geophysical Research Letters*, 31(13):L13310.

Chao, B. F. (2006). Earth's oblateness and its temporal variations. *Comptes Rendus Geoscience*, 338(14–15):1123–1129.

Chao, B. F., Au, A. Y., Boy, J.-P., and Cox, C. M. (2003). Time-variable gravity signal of an anomalous redistribution of water mass in the extratropic Pacific during 1998–2002. *Geochemistry, Geophysics, Geosystems*, 4(11):1096.

Chao, B. F. and Eanes, R. (1995). Global gravitational changes due to atmospheric mass redistribution as observed by the Lageos nodal residual. *Geophysical Journal International*, 122(3):755–764.

Chen (2000). A new assessment of long-wavelength gravitational variations. *Journal of Geophysical Research*, 105:16271–16278.

Chen, J. L., Rodell, M., Wilson, C. R., and Famiglietti, J. S. (2005). Low degree spherical harmonic influences on Gravity Recovery and Climate Experiment (GRACE) water storage estimates. *Geophysical Research Letters*, 32(14):L14405.

Chen, J. L. and Wilson, C. R. (2003). Low degree gravitational changes from earth rotation and geophysical models. *Geophysical Research Letters*, 30(24):2257.

Chen, J. L. and Wilson, C. R. (2008). Low degree gravity changes from GRACE, Earth rotation, geophysical models, and satellite laser ranging. *Journal of Geophysical Research: Solid Earth*, 113(B6):B06402.

Chen, J. L., Wilson, C. R., Eanes, R. J., and Nerem, R. S. (1999). Geophysical interpretation of observed geocenter variations. *Journal of Geophysical Research: Solid Earth*, 104(B2):2683–2690. 00103.

Chen, J. L., Wilson, C. R., and Ries, J. C. (2016). Broadband assessment of degree-2 gravitational changes from GRACE and other estimates, 2002–2015. *Journal of Geophysical Research: Solid Earth*, 121(3):2112–2128.

Chen, J. L., Wilson, C. R., Tapley, B. D., and Ries, J. C. (2004). Low degree gravitational changes from GRACE: Validation and interpretation. *Geophysical Research Letters*, 31(22):L22607.

Cheng, M. and Ries, J. (2012). Monthly estimates of C20 from 5 SLR satellites based on GRACE RL05 models. In *GRACE Technical Note 07*. Center for Space Research, University of Texas at Austin.

Cheng, M. and Ries, J. (2017). The unexpected signal in GRACE estimates of C_{20}. *Journal of Geodesy*, pages 1–18.

Cheng, M. and Tapley, B. D. (1999). Seasonal variations in low degree zonal harmonics of the Earth's gravity field from satellite laser ranging observations. *Journal of Geophysical Research: Solid Earth*, 104(B2):2667–2681. 00059.

Cheng, M. and Tapley, B. D. (2004). Variations in the Earth's oblateness during the past 28 years. *Journal of Geophysical Research: Solid Earth*, 109(B9):B09402.

Cheng, M., Tapley, B. D., and Ries, J. C. (2013a). Deceleration in the Earth's oblateness. *Journal of Geophysical Research: Solid Earth*, 118(2):740–747. 00011.

Cheng, M. K., Eanes, R. J., Shum, C. K., Schutz, B. E., and Tapley, B. D. (1989). Temporal variations in low degree zonal harmonics from Starlette orbit analysis. *Geophysical Research Letters*, 16(5):393–396. 00122.

Cheng, M. K., Ries, J. C., and Tapley, B. D. (2013b). Geocenter Variations from Analysis of SLR Data. In Altamimi, Z. and Collilieux, X., editors, *Reference Frames for Applications in Geosciences*, number 138 in International Association of Geodesy Symposia, pages 19–25. Springer Berlin Heidelberg. 00016.

Cheng, M. K., Shum, C. K., and Tapley, B. D. (1997). Determination of long-term changes in the Earth's gravity field from satellite laser ranging observations. *Journal of Geophysical Research: Solid Earth*, 102(B10):22377–22390. 00087.

Clarke, P. J., Lavallée, D. A., Blewitt, G., van Dam, T. M., and Wahr, J. M. (2005). Effect of gravitational consistency and mass conservation on seasonal surface mass loading models. *Geophysical Research Letters*, 32(8):L08306.

Collilieux, X., Altamimi, Z., Ray, J., van Dam, T., and Wu, X. (2009). Effect of the satellite laser ranging network distribution on geocenter motion estimation. *Journal of Geophysical Research: Solid Earth*, 114(B4):B04402.

Conrad, C. P. and Hager, B. H. (1997). Spatial variations in the rate of sea level rise caused by the present-day melting of glaciers and ice sheets. *Geophysical Research Letters*, 24(12):1503–1506.

Cox, C. M. and Chao, B. F. (2002). Detection of a Large-Scale Mass Redistribution in the Terrestrial System Since 1998. *Science*, 297(5582):831–833.

Crétaux, J.-F., Soudarin, L., Davidson, F. J. M., Gennero, M.-C., Bergé-Nguyen, M., and Cazenave, A. (2002). Seasonal and interannual geocenter motion from SLR and DORIS measurements: Comparison with surface loading data. *Journal of Geophysical Research: Solid Earth*, 107(B12):ETG 16–1–ETG 16–9. 00062.

Dahle, C., Flechtner, F., Gruber, C., König, D., König, R., Michalak, G., Neumayer, K.-H., and GFZ, D. G. (2013). *GFZ GRACE level-2 processing standards document for level-2 product release 0005*. Deutsches GeoForschungsZentrum GFZ.

Dee, D. P., Uppala, S. M., Simmons, A. J., Berrisford, P., Poli, P., Kobayashi, S., Andrae, U., Balmaseda, M. A., Balsamo, G., Bauer, P., Bechtold, P., Beljaars, A. C. M., van de Berg, L., Bidlot, J., Bormann, N., Delsol, C., Dragani, R., Fuentes, M., Geer, A. J., Haimberger, L., Healy, S. B., Hersbach, H., Hólm, E. V., Isaksen, L., Kållberg, P., Köhler, M., Matricardi, M., McNally, A. P., Monge-Sanz, B. M., Morcrette, J.-J., Park, B.-K., Peubey, C., de Rosnay, P., Tavolato, C., Thépaut, J.-N., and Vitart, F. (2011). The ERA-Interim reanalysis: configuration and performance of the data assimilation system. *Quarterly Journal of the Royal Meteorological Society*, 137(656):553–597.

Dickey, J. O., Marcus, S. L., de Viron, O., and Fukumori, I. (2002). Recent Earth oblateness variations: unraveling climate and postglacial rebound effects. *Science (New York, N.Y.)*, 298(5600):1975–1977.

Dill, R. (2008). Hydrological model LSDM for operational Earth rotation and gravity eld variations.

Ditmar, P., Encarnação, J. T. d., and Farahani, H. H. (2011). Understanding data noise in gravity field recovery on the basis of inter-satellite ranging measurements acquired by the satellite gravimetry mission GRACE. *Journal of Geodesy*, 86(6):441–465.

Ditmar, P., Natthachet, T., Jiangjun, R., and Roland, K. (2017). Mass anomaly time-series based on satellite gravimetry data: regularization and noise quantification. *submitted to Geophysical Journal International*.

Dobslaw, H., Bergmann-Wolf, I., Dill, R., Forootan, E., Klemann, V., Kusche, J., and Sasgen, I. (2015). The updated ESA Earth System Model for future gravity mission simulation studies. *Journal of Geodesy*, 89(5):505–513.

Dobslaw, H., Bergmann-Wolf, I., Forootan, E., Dahle, C., Mayer-Gürr, T., Kusche, J., and Flechtner, F. (2016). Modeling of present-day atmosphere and ocean non-tidal de-aliasing errors for future gravity mission simulations. *Journal of Geodesy*, 90(5):423–436.

Dong, D., Dickey, J. O., Chao, Y., and Cheng, M. K. (1997). Geocenter variations caused by atmosphere, ocean and surface ground water. *Geophysical Research Letters*, 24(15):1867–1870.

Dong, D., Fang, P., Bock, Y., Cheng, M. K., and Miyazaki, S. (2002). Anatomy of apparent seasonal variations from GPS-derived site position time series. *Journal of Geophysical Research: Solid Earth*, 107(B4). 00300.

Dong, D., Qu, W., Fang, P., and Peng, D. (2014). Non-linearity of geocentre motion and its impact on the origin of the terrestrial reference frame. *Geophysical Journal International*, 198(2):1071–1080.

Dong, D., Yunck, T., and Heflin, M. (2003). Origin of the International Terrestrial Reference Frame. *Journal of Geophysical Research: Solid Earth*, 108(B4). 00088.

Ettema, J., van den Broeke, M. R., van Meijgaard, E., van de Berg, W. J., Bamber, J. L., Box, J. E., and Bales, R. C. (2009). Higher surface mass balance of the Greenland ice sheet revealed by high-resolution climate modeling. *Geophysical Research Letters*, 36(12):L12501.

Farahani, H. H., Ditmar, P., Inácio, P., Didova, O., Gunter, B., Klees, R., Guo, X., Guo, J., Sun, Y., Liu, X., Zhao, Q., and Riva, R. (2017). A high resolution model of linear trend in mass variations from DMT-2: Added value of accounting for coloured noise in GRACE data. *Journal of Geodynamics*, 103:12–25.

Farrell, W. E. (1972). Deformation of the Earth by surface loads. *Reviews of Geophysics*, 10(3):761–797.

Farrell, W. E. and Clark, J. A. (1976). On Postglacial Sea Level. *Geophysical Journal of the Royal Astronomical Society*, 46(3):647–667.

Flechtner, F. and Dobslaw, H. (2013). AOD1b Product Description Document for Product Release. 05. *GFZ German Research Centre for Geosciences*.

Fritsche, M., Dietrich, R., Rülke, A., Rothacher, M., and Steigenberger, P. (2010). Low-degree earth deformation from reprocessed GPS observations. *GPS Solutions*, 14(2):165–175.

Fukumori, I. (2002). A Partitioned Kalman Filter and Smoother. *Monthly Weather Review*, 130(5):1370–1383.

Gobinddass, M. L., Willis, P., de Viron, O., Sibthorpe, A., Zelensky, N. P., Ries, J. C., Ferland, R., Bar-Sever, Y., Diament, M., and Lemoine, F. G. (2009a). Improving DORIS geocenter time series using an empirical rescaling of solar radiation pressure models. *Advances in Space Research*, 44(11):1279–1287.

Gobinddass, M. L., Willis, P., Viron, O. d., Sibthorpe, A., Zelensky, N. P., Ries, J. C., Ferland, R., Bar-Sever, Y., and Diament, M. (2009b). Systematic biases in DORIS-derived geocenter time series related to solar radiation pressure mis-modeling. *Journal of Geodesy*, 83(9):849–858.

Gordeev, R. G., Kagan, B. A., and Polyakov, E. V. (1977). The Effects of Loading and Self-Attraction on Global Ocean Tides: The Model and the Results of a Numerical Experiment. *Journal of Physical Oceanography*, 7(2):161–170.

Griffiths, J. and Ray, J. R. (2013). Sub-daily alias and draconitic errors in the IGS orbits. *GPS Solutions*, 17(3):413–422. 00005.

Gross, R. (2003). Combinations of Earth orientation measurements: SPACE2002, COMB2002, and POLE2002. Technical report, Jet Propulsion Laboratory.

Gross, R., Beutler, G., and Plag, H.-P. (2009). Integrated scientific and societal user requirements and functional specifications for the GGOS. In Plag, H.-P. and Pearlman, M., editors, *Global Geodetic Observing System*, pages 209–224. Springer Berlin Heidelberg. DOI: 10.1007/978-3-642-02687-4_7.

Gross, R. S. (1996). Combinations of Earth orientation measurements: SPACE94, COMB94, and POLE94. *Journal of Geophysical Research: Solid Earth*, 101(B4):8729–8740.

Gross, R. S., Blewitt, G., Clarke, P. J., and Lavallée, D. (2004). Degree-2 harmonics of the Earth's mass load estimated from GPS and Earth rotation data. *Geophysical Research Letters*, 31(7):L07601.

Gruber, T., Bamber, J. L., Bierkens, M. F. P., Dobslaw, H., Murböck, M., Thomas, M., van Beek, L. P. H., van Dam, T., Vermeersen, L. L. A., and Visser, P. N. A. M. (2011). Simulation of the time-variable gravity field by means of coupled geophysical models. *Earth System Science Data*, 3(1):19–35.

Gunter, B. C., Didova, O., Riva, R. E. M., Ligtenberg, S. R. M., Lenaerts, J. T. M., King, M. A., van den Broeke, M. R., and Urban, T. (2014). Empirical estimation of present-day Antarctic glacial isostatic adjustment and ice mass change. *The Cryosphere*, 8(2):743–760.

Gutierrez, R. and Wilson, C. R. (1987). Seasonal air and water mass redistribution effects on LAGEOS and Starlette. *Geophysical Research Letters*, 14(9):929–932.

Han, S.-C., Shum, C. K., Bevis, M., Ji, C., and Kuo, C.-Y. (2006). Crustal Dilatation Observed by GRACE After the 2004 Sumatra-Andaman Earthquake. *Science*, 313(5787):658–662.

Helsen, M. M., Broeke, M. R. v. d., Wal, R. S. W. v. d., Berg, W. J. v. d., Meijgaard, E. v., Davis, C. H., Li, Y., and Goodwin, I. (2008). Elevation Changes in Antarctica Mainly Determined by Accumulation Variability. *Science*, 320(5883):1626–1629.

Hughes, C. W., Tamisiea, M. E., Bingham, R. J., and Williams, J. (2012). Weighing the ocean: Using a single mooring to measure changes in the mass of the ocean. *Geophysical Research Letters*, 39(17):L17602.

Ivins, E. R. and James, T. S. (2005). Antarctic glacial isostatic adjustment: a new assessment. *Antarctic Science*, 17(04):541–553.

Jansen, M. J. F., Gunter, B. C., and Kusche, J. (2009). The impact of GRACE, GPS and OBP data on estimates of global mass redistribution. *Geophysical Journal International*, 177(1):1–13. 00010.

Kim, S.-B., Lee, T., and Fukumori, I. (2007). Mechanisms Controlling the Interannual Variation of Mixed Layer Temperature Averaged over the Niño-3 Region. *Journal of Climate*, 20(15):3822–3843.

Klees, R., Revtova, E. A., Gunter, B. C., Ditmar, P., Oudman, E., Winsemius, H. C., and Savenije, H. H. G. (2008). The design of an optimal filter for monthly GRACE gravity models. *Geophysical Journal International*, 175(2):417–432.

Klemann, V. and Martinec, Z. (2011). Contribution of glacial-isostatic adjustment to the geocenter motion. *Tectonophysics*, 511(3–4):99–108.

Klinger, B. and Mayer-Gürr, T. (2016). The role of accelerometer data calibration within GRACE gravity field recovery: Results from ITSG-Grace2016. *Advances in Space Research*, 58(9):1597–1609.

Koch, K.-R. and Kusche, J. (2002). Regularization of geopotential determination from satellite data by variance components. *Journal of Geodesy*, 76(5):259–268.

Kusche, J., Schmidt, R., Petrovic, S., and Rietbroek, R. (2009). Decorrelated GRACE time-variable gravity solutions by GFZ, and their validation using a hydrological model. *Journal of Geodesy*, 83(10):903–913.

Kusche, J. and Schrama, E. J. O. (2005). Surface mass redistribution inversion from global GPS deformation and Gravity Recovery and Climate Experiment (GRACE) gravity data. *Journal of Geophysical Research: Solid Earth*, 110(B9). 00054.

Lambeck, K. (2005). *The Earth's variable rotation: geophysical causes and consequences*. Cambridge University Press.

Lambeck, K., Rouby, H., Purcell, A., Sun, Y., and Sambridge, M. (2014). Sea level and global ice volumes from the Last Glacial Maximum to the Holocene. *Proceedings of the National Academy of Sciences*, 111(43):15296–15303.

Lavallée, D. A., Moore, P., Clarke, P. J., Petrie, E. J., van Dam, T., and King, M. A. (2010). J2: An evaluation of new estimates from GPS, GRACE, and load models compared to SLR. *Geophysical Research Letters*, 37(22). 00007.

Lavallée, D. A., van Dam, T., Blewitt, G., and Clarke, P. J. (2006). Geocenter motions from GPS: A unified observation model. *Journal of Geophysical Research: Solid Earth*, 111(B5). 00051.

Lemoine, J.-M., Bruinsma, S., Gégout, P., Biancale, R., and Bourgogne, S. (2013). Release 3 of the GRACE gravity solutions from CNES/GRGS. volume 15, pages EGU2013–11123.

Liu, X., Ditmar, P., Siemes, C., Slobbe, D. C., Revtova, E., Klees, R., Riva, R., and Zhao, Q. (2010). DEOS Mass Transport model (DMT-1) based on GRACE satellite data: methodology and validation. *Geophysical Journal International*, 181(2):769–788.

Meindl, M., Beutler, G., Thaller, D., Dach, R., and Jäggi, A. (2013). Geocenter coordinates estimated from GNSS data as viewed by perturbation theory. *Advances in Space Research*, 51(7):1047–1064. 00007.

Meisel, B., Angermann, D., Krügel, M., Drewes, H., Gerstl, M., Kelm, R., Müller, H., Seemüller, W., and Tesmer, V. (2005). Refined approaches for terrestrial reference frame computations. *Advances in Space Research*, 36(3):350–357.

Meyrath, T., Rebischung, P., and van Dam, T. (2017). GRACE era variability in the Earth's oblateness: a comparison of estimates from six different sources. *Geophysical Journal International*, 208(2):1126–1138.

Meyrath, T., van Dam, T., Weigelt, M., and Cheng, M. (2013). An assessment of degree-2 Stokes coefficients from Earth rotation data. *Geophysical Journal International*, 195(1):249–259.

Milne, A., G. and Mitrovica, X., J. (1998). Postglacial sea-level change on a rotating Earth. *Geophysical Journal International*, 133(1):1–19.

Milne, G. A., Davis, J. L., Mitrovica, J. X., Scherneck, H.-G., Johansson, J. M., Vermeer, M., and Koivula, H. (2001). Space-Geodetic Constraints on Glacial Isostatic Adjustment in Fennoscandia. *Science*, 291(5512):2381–2385.

Mitrovica, J. X. and Forte, A. M. (1997). Radial profile of mantle viscosity: Results from the joint inversion of convection and postglacial rebound observables. *Journal of Geophysical Research: Solid Earth*, 102(B2):2751–2769.

Mitrovica, J. X., Tamisiea, M. E., Davis, J. L., and Milne, G. A. (2001). Recent mass balance of polar ice sheets inferred from patterns of global sea-level change. *Nature*, 409(6823):1026–1029.

Nerem, R. S. and Wahr, J. (2011). Recent changes in the Earth's oblateness driven by Greenland and Antarctic ice mass loss. *Geophysical Research Letters*, 38(13):L13501.

Peltier, W. (2004). Global glacial isostasy and the surface of the ice-age Earth: the ICE-5g (VM2) model and GRACE. *Annual Review of Earth and Planetary Sciences*, 32(1):111–149.

Peltier, W. R., Argus, D. F., and Drummond, R. (2015). Space geodesy constrains ice age terminal deglaciation: The global ICE-6g_c (VM5a) model. *Journal of Geophysical Research: Solid Earth*, 120(1):2014JB011176.

Petit, G. and Luzum, B. (2010). IERS conventions (2010). Technical Note 36, Verlag des Bundesamts für Kartographie und Geodäsie, Frankfurt am Main.

Ray, J. (1999). IERS Analysis Campaign to Investigate Motions of the Geocenter. Technical Note 25, Central Bureau of IERS Observatioire de Paris, Paris.

Ray, J., Altamimi, Z., Collilieux, X., and Dam, T. v. (2008). Anomalous harmonics in the spectra of GPS position estimates. *GPS Solutions*, 12(1):55–64.

Ray, R. D. and Ponte, R. M. (2003). Barometric tides from ECMWF operational analyses. *Ann. Geophys.*, 21(8):1897–1910.

Rebischung, P., Altamimi, Z., and Springer, T. (2014). A collinearity diagnosis of the GNSS geocenter determination. *Journal of Geodesy*, 88(1):65–85. 00001.

Riddell, A. R., King, M. A., Watson, C. S., Sun, Y., Riva, R. E. M., and Rietbroek, R. (2017). Uncertainty in geocenter estimates in the context of ITRF2014. *Journal of Geophysical Research: Solid Earth*, 122(5):2016JB013698.

Ries, J. C. (2013). Annual Geocenter Motion from Space Geodesy and Models. *AGU Fall Meeting Abstracts*, -1:06.

Rietbroek, R., Brunnabend, S.-E., Dahle, C., Kusche, J., Flechtner, F., Schröter, J., and Timmermann, R. (2009). Changes in total ocean mass derived from GRACE, GPS, and ocean modeling with weekly resolution. *Journal of Geophysical Research: Oceans*, 114(C11). 00020.

Rietbroek, R., Brunnabend, S. E., Kusche, J., and Schröter, J. (2012a). Resolving sea level contributions by identifying fingerprints in time-variable gravity and altimetry. *Journal of Geodynamics*, 59–60:72–81. 00013.

Rietbroek, R., Brunnabend, S.-E., Kusche, J., Schröter, J., and Dahle, C. (2016). Revisiting the contemporary sea-level budget on global and regional scales. *Proceedings of the National Academy of Sciences*, 113(6):1504–1509.

Rietbroek, R., Fritsche, M., Brunnabend, S. E., Daras, I., Kusche, J., Schröter, J., Flechtner, F., and Dietrich, R. (2012b). Global surface mass from a new combination of GRACE, modelled OBP and reprocessed GPS data. *Journal of Geodynamics*, 59-60:64–71. 00023.

Riva, R. E. M., Gunter, B. C., Urban, T. J., Vermeersen, B. L. A., Lindenbergh, R. C., Helsen, M. M., Bamber, J. L., van de Wal, R. S. W., van den Broeke, M. R., and Schutz, B. E. (2009). Glacial Isostatic Adjustment over Antarctica from combined ICESat and GRACE satellite data. *Earth and Planetary Science Letters*, 288(3–4):516–523.

Rülke, A., Dietrich, R., Fritsche, M., Rothacher, M., and Steigenberger, P. (2008). Realization of the Terrestrial Reference System by a reprocessed global GPS network. *Journal of Geophysical Research: Solid Earth*, 113(B8):B08403.

Seo, K.-W., Chen, J., Wilson, C. R., and Lee, C.-K. (2015). Decadal and quadratic variations of Earth's oblateness and polar ice mass balance from 1979 to 2010. *Geophysical Journal International*, 203(1):475–481.

Siegismund, F., Romanova, V., Köhl, A., and Stammer, D. (2011). Ocean bottom pressure variations estimated from gravity, nonsteric sea surface height and hydrodynamic model simulations. *Journal of Geophysical Research: Oceans*, 116(C7):C07021.

Sośnica, K., Jäggi, A., Thaller, D., Beutler, G., and Dach, R. (2014). Contribution of Starlette, Stella, and AJISAI to the SLR-derived global reference frame. *Journal of Geodesy*, 88(8):789–804.

Sośnica, K., Thaller, D., Dach, R., Jäggi, A., and Beutler, G. (2013). Impact of loading displacements on SLR-derived parameters and on the consistency between GNSS and SLR results. *Journal of Geodesy*, 87(8):751–769.

Spada, G., Barletta, V. R., Klemann, V., Riva, R. E. M., Martinec, Z., Gasperini, P., Lund, B., Wolf, D., Vermeersen, L. L. A., and King, M. A. (2011). A benchmark study for glacial isostatic adjustment codes. *Geophysical Journal International*, 185(1):106–132.

Storch, J.-S. v., Eden, C., Fast, I., Haak, H., Hernández-Deckers, D., Maier-Reimer, E., Marotzke, J., and Stammer, D. (2012). An Estimate of the Lorenz Energy Cycle for the World Ocean Based on the STORM/NCEP Simulation. *Journal of Physical Oceanography*, 42(12):2185–2205.

Sun, Y., Ditmar, P., and Riva, R. (2016a). Observed changes in the Earth's dynamic oblateness from GRACE data and geophysical models. *Journal of Geodesy*, 90(1):81–89.

Sun, Y., Ditmar, P., and Riva, R. (2017). Statistically optimal estimation of degree-1 and C20 coefficients based on GRACE data and an ocean bottom pressure model. *Geophysical Journal International*.

Sun, Y., Riva, R., and Ditmar, P. (2016b). Optimizing estimates of annual variations and trends in geocenter motion and J2 from a combination of GRACE data and geophysical models. *Journal of Geophysical Research: Solid Earth*, 121(11):8352–8370.

Sutterley, T. C., Velicogna, I., Csatho, B., Broeke, M. v. d., Soroush Rezvan-Behbahani, and Babonis, G. (2014). Evaluating Greenland glacial isostatic adjustment corrections using GRACE, altimetry and surface mass balance data. *Environmental Research Letters*, 9(1):014004.

Swenson, S., Chambers, D., and Wahr, J. (2008). Estimating geocenter variations from a combination of GRACE and ocean model output. *Journal of Geophysical Research: Solid Earth*, 113(B8):B08410.

Swenson, S. and Wahr, J. (2006). Post-processing removal of correlated errors in GRACE data. *Geophysical Research Letters*, 33(8):L08402.

Tamisiea, M. E., Hill, E. M., Ponte, R. M., Davis, J. L., Velicogna, I., and Vinogradova, N. T. (2010). Impact of self-attraction and loading on the annual cycle in sea level. *Journal of Geophysical Research: Oceans*, 115(C7):C07004.

Tapley, B. D., Bettadpur, S., Watkins, M., and Reigber, C. (2004). The gravity recovery and climate experiment: Mission overview and early results. *Geophysical Research Letters*, 31(9):L09607.

Teunissen, P. (2000). Adjustment theory. *An Introduction, Series on Mathematical Geodesy and Positioning*, 193.

Thomas, M. (2002). *Ocean induced variations of Earth's rotation results from a simultaneous model of global circulation and tides*. PhD thesis, Univ. of Hamburg, Germany.

Tregoning, P. and van Dam, T. (2005). Effects of atmospheric pressure loading and seven-parameter transformations on estimates of geocenter motion and station heights from space geodetic observations. *Journal of Geophysical Research: Solid Earth*, 110(B3):B03408.

Wagner, C., McAdoo, D., Klokočník, J., and Kostelecký, J. (2006). Degradation of Geopotential Recovery from Short Repeat-Cycle Orbits: Application to GRACE Monthly Fields. *Journal of Geodesy*, 80(2):94–103.

Wahr, J., Molenaar, M., and Bryan, F. (1998). Time variability of the Earth's gravity field: Hydrological and oceanic effects and their possible detection using GRACE. *Journal of Geophysical Research: Solid Earth*, 103(B12):30205–30229.

Wahr, J., Nerem, R. S., and Bettadpur, S. V. (2015). The pole tide and its effect on GRACE time-variable gravity measurements: Implications for estimates of surface mass variations. *Journal of Geophysical Research: Solid Earth*, 120(6):2015JB011986.

Wahr, J., Wingham, D., and Bentley, C. (2000). A method of combining ICESat and GRACE satellite data to constrain Antarctic mass balance. *Journal of Geophysical Research: Solid Earth*, 105(B7):16279–16294.

Watkins, M. (2012). JPL Level-2 Processing Standards Document. Technical Version 4, Jet Propulsion Laboratory.

Watkins, M. M. and Eanes, R. J. (1997). Observations of tidally coherent diurnal and semidiurnal variations in the geocenter. *Geophysical Research Letters*, 24(17):2231–2234.

Willis, P., Bar-Sever, Y. E., and Tavernier, G. (2005). DORIS as a potential part of a Global Geodetic Observing System. *Journal of Geodynamics*, 40(4–5):494–501.

Willis, P., Berthias, J.-P., and Bar-Server, Y. E. (2006). Systematic errors in the Z-geocenter derived using satellite tracking data: a case study from SPOT-4 DORIS data in 1998. *Journal of Geodesy*, 79(10-11):567–572.

Wouters, B., Riva, R. E. M., Lavallée, D. A., and Bamber, J. L. (2011). Seasonal variations in sea level induced by continental water mass: First results from GRACE. *Geophysical Research Letters*, 38(3):L03303.

Wu, X., Abbondanza, C., Altamimi, Z., Chin, T. M., Collilieux, X., Gross, R. S., Heflin, M. B., Jiang, Y., and Parker, J. W. (2015). KALREF—A Kalman filter and time series approach to the International Terrestrial Reference Frame realization. *Journal of Geophysical Research: Solid Earth*, 120(5):2014JB011622.

Wu, X., Argus, D. F., Heflin, M. B., Ivins, E. R., and Webb, F. H. (2002). Site distribution and aliasing effects in the inversion for load coefficients and geocenter motion from GPS data. *Geophysical Research Letters*, 29(24):63–1–63–4. 00036.

Wu, X., Collilieux, X., Altamimi, Z., Vermeersen, L. L. A., Gross, R. S., Fukumori, I., and TU Delft: Aerospace Engineering: Space Engineering (2011). Accuracy of the International Terrestrial Reference Frame origin and Earth expansion. 00023.

Wu, X., Heflin, M. B., Ivins, E. R., Argus, D. F., and Webb, F. H. (2003). Large-scale global surface mass variations inferred from GPS measurements of load-induced deformation. *Geophysical Research Letters*, 30(14). 00043.

Wu, X., Heflin, M. B., Ivins, E. R., and Fukumori, I. (2006). Seasonal and interannual global surface mass variations from multisatellite geodetic data. *Journal of Geophysical Research: Solid Earth*, 111(B9). 00050.

Wu, X., Heflin, M. B., Schotman, H., Vermeersen, B. L. A., Dong, D., Gross, R. S., Ivins, E. R., Moore, A. W., and Owen, S. E. (2010). Simultaneous estimation of global present-day water transport and glacial isostatic adjustment. *Nature Geoscience*, 3(9):642–646.

Wu, X., Kusche, J., and Landerer, F. W. (2017). A new unified approach to determine geocentre motion using space geodetic and GRACE gravity data. *Geophysical Journal International*, 209(3):1398–1402.

Wu, X., Ray, J., and van Dam, T. (2012). Geocenter motion and its geodetic and geophysical implications. *Journal of Geodynamics*, 58:44–61. 00024.

Yoder, C. F., Williams, J. G., Dickey, J. O., Schutz, B. E., Eanes, R. J., and Tapley, B. D. (1983). Secular variation of Earth's gravitational harmonic J2 coefficient from Lageos and nontidal acceleration of Earth rotation. *Nature*, 303(5920):757–762.

Acknowledgements

After five years of working on a specific topic, it is possible to write a book, but not possible to come up with a full list of all the people who had helped.

I am grateful to Chinese Scholar Council for granting me such a generous scholarship. My former supervisors, professor Xiaotao Chang and Jinyun Guo, are acknowledged for being my guarantors. Without this fantastic program, the last several years of amazing experiences would have never been exist. I thank Cees Timmers for his interview in Beijing, and I am appreciate all the help from Franca Post for her assistant when I just arrived at Delf.

I wish to thank my promoter professor Roland Klees for accepting me as a PhD candidate in his group. I am also grateful for his efficient work, prompt response, valuable and constructive suggestions. Otherwise, this work will not be finished in time.

I would like to express my very great appreciation to my daily supervisors, Riccardo Riva and Pavel Ditmar. They guided me through every step in the whole training period. And I consider myself the luckiest student to have two wonderful supervisors with complementary characters. Riccardo is sharp, encouraging and thoughtful. He formulated this project, arranged the interview and offering me with sufficient freedom. He is the reason that I am here in the first place. I see him more like a dear friend than a boss. However, he did pay the bills for my computers and conference travels. Pavel is the more accurate and rational one in our team. He would edit every word and check every little detail of our papers before submission. Seriously, I have more than ten versions of each paper. I am assured that our paper will be accepted if Pavel says so. Both of them have contributed significantly to the every result described in this thesis. Also we had numerous fruitful discussions aside our regular weekly meetings.

This thesis was also accomplished with the help and support of my colleagues, fellow lab-mates. I thank Jiangjun Ran, Xiang Guo, Natthachet Tangdamrongsub for many interesting daily discussions about almost everything. We will definitely be more connected in the near future. I enjoy every sea-level coffee with Marcel Kleinherenbrink, Thomas Frederikse, Karen Simon and Francesca Panzetta. I love so much the San Francisco trip with them. I wish we can drinking bears and cycling through the Golden Gate bridge sometime again! Pedro Inácio and Cornelis Slobbe are acknowledged for their great help and patience on solving clusters related issues. My gratitude also goes to Yihao Wu, Hassan Farahani, Taco Broerse, Olga

Didova for many helpful discussions. My Special thanks are extended to our secretaries, Lidwien de Jong, Debbie Rietdijk, Suzanne de Hoog, Irma Zomerdijk and rebeca domingo for their help. I have spent three weeks on the absolute gravimetry campaign with Rene Reudink. I thank Rene for telling me so many interesting history of the Netherlands and I really miss the beautiful scenery of small dutch countries.

Several colleagues who may not directly contributed to this work, but helped me in many other ways. Without their companion, I will no walk through all the difficult times. Here, I would like to express my appreciation to Jinhu Wang and Yerong Wu, Junchao Shi and Yanqing Hou. Jinhu, Yerong and I came to Delft at about the same time and worked in the same lab for three years. Then, me, yerong and Junchao shared a smaller room. Now we are all finishing/finished our project here and facing more challenges in life.

I would like to offer my special thanks to all my lab-mates: Jinliang Li, Xiaojun Luo, Yu Chen and Ling Chang Kaixuan Zhou, Han Dun, Mengshi Yang, Yueqian Shen, Jiapeng Yin. I enjoy playing games and lunch talking with you guys and hope to see you grow big and strong in academia. I am also grateful to my friends from other departments: Tao Lv, Guangming Chen, Xiangrong Wang, Peng Lu ...

There are also dozens of people who have shared the same roof with me. They know nothing about my topic, but they take care of me when ever they can. I had so much fun time with them and life would be much harder if they are not there for me. I wish to thank all my dear house-mates: Lijian Qi, Tao Zou, Xing Chang, Zilong Wei, Yan Zhou, Likun Ma, Lin Liu, Xiaoyan Wei, Zaibin Lin, Changgong Zhang, Jia Xu, Jialun Liu, Shijie Li and Zong Wei Li ... We talk, laugh, gossip, travel, watching movie, playing games ... I enjoyed every moment with you guys. I wish you all have a very bright future!

I wish to thank my parents, parents-in-law and brother-in-law. They helped me so much emotionally that I could not express in words. My parents are my very first and the most important mentors and I will be grateful to them for the rest of my life for their unconditional love. 感谢父母无私的爱与几十年的养育之恩. 在我有了自己的孩子之后才体会到父母的辛劳与付出. 谁言寸草心,报得三春晖.

Finally, I would like to thank my wife, Hongyue. We are so lucky that we are each other's first love. We meet each other in early 2011, married last August and now we have a cute little boy. All of this may be nothing for other couples but means a lot to us, because I came to the Netherlands alone in 2012 and we are maintaining a long-distance relationship for over five years since then. I owe her so much. Especially, she has to take care our baby when I have to stay here finishing this PhD thesis. Hongyue, I love you so much and happy to grow old with you. My son, Qingyuan, you are the most beautiful "accident" in my life. I miss your heart-melting smile everyday and cannot wait to be with you again. I love you always forever.

List of Publications

Journal publications related to this dissertation

1. **Y. Sun**, P. Ditmar, R. Riva (2017). *Statistically optimal estimation of degree-1 and C_{20} coefficients based on GRACE data and ocean bottom pressure model. Geophysical Journal International, 210(2):561-569.*

2. **Y. Sun**, R. Riva, P. Ditmar (2016). *Optimizing estimates of annual variations and trends in geocenter motion and J_2 from a combination of GRACE data and geophysical models. Journal of Geophysical Research: Solid Earth, 112(11):8352-8370.*

3. **Y. Sun**, P. Ditmar, R. Riva (2016). *Observed changes in the Earth's dynamic oblateness from GRACE data and geophysical models. Journal of Geodesy, 90(1):81-89.*

Other journal publications

1. X. Liu, L. Guo, **Y. Sun**, J. Guo, B. Guo, N. Mu. *Equivalent water height change over Qinghai-Tibet Plateau determined from GRACE with independent component analysis. Submitted to Journal of Hydrology.*

2. A. Riddell, M. King, C. Watson, **Y. Sun**, R. Riva, R. Rietbroek (2017). *Uncertainty in the ITRF2014 origin and comparison with surface mass transport models. Journal of Geophysical Research, 122(5):4020-4032.*

3. H. Farahani, P. Ditmar, P. Inácio, O. Didova, B. Gunter, R. Klees, X. Guo, J. Guo, **Y. Sun**, X. Liu, Q. Zhao, R. Riva (2017) *A high resolution model of linear trend in mass variations from DMT-2: Added value of accounting for coloured noise in GRACE data. Journal of Geodynamics, 103:12-25.*

4. N. Tangdamrongsub, S. Steele-Dunne, B. Gunter, P. Ditmar, E. Sutanudjaja, **Y. Sun**, T. Xia, Z. Wang (2017). *Improving estimates of water resources in a semi-arid region by assimilating GRACE data into the PCR-GLOBWB hydrological model. Hydrology and Earth System Sciences, 21(4):2053-2074.*

5. J. Wang, J. Guo, X. Liu, Q. Kong, Y. Shen, **Y. Sun** (2017). *Orthometric height connection across sea with ship-borne gravimetry and GNSS measurement along the ship route. Acta Geodaetica et Geophysica, 52(3):357-373.*

6. Q. Kong, J. Guo, **Y. Sun**, C. Zhao, C. Cheng (2017). *Centimeter-level precise orbit determination for the HY-2A satellite using DORIS and SLR tracking data. Acta Geophysica, 65(1):1-12.*

7. M. Kleinherenbrink, R. Riva, **Y. Sun** (2016). *Sub-basin scale sea level budgets from satellite altimetry, Argo floats and satellite gravimetry in the North Atlantic. Ocean Science, 12(6):1179-1203.*

8. **Y. Sun**, X. Chang, J. Guo, B. Ke (2013). *The Analysis of Lunar Gravity Field Characters from SGM100i. Geomatics and Information Science of Wuhan University, 38(1):64-68.*

9. J. Guo, Q. Kong, J. Qin, **Y. Sun** (2013) *On precise orbit determination of HY-2 with space geodetic techniques. Acta Geophysica, 61(3):752-772.*

10. Q. Kong, J. Guo, J. Qin, **Y. Sun** (2013). *Simulation of Centimeter-Level Precise Orbit Determination for HY-2 Satellite Using DORIS and SLR. Geomatics and Information Science of Wuhan University, 38(6)694-699.*

11. **Y. Sun**, X. Chang, J. Guo, Q. Kong (2012). *Contribution of SELENE for Lunar Gravity Field Recovery from quality analysis of SGM100i. Science of Surveying and Mapping, 37(2):176-178.*

12. J. Guo, **Y. Sun**, X. Chang, F. Yang (2011). *Lunar deflections of the vertical and their distribution. Natual Science, 3(5):339-343.*

Contributions to Conferences

1. *European Geosciences Union (EGU) General Assembly. April 23-28, 2017 Vienna, Austria.*

2. *American Geophysical Union (AGU) Fall Meeting. Estimating geocenter motion and changes in Earth's dynamic oblateness from a statistically optimal combination of GRACE data and an OBP model. December 12-16, 2016 San Francisco, America.*

3. *American Geophysical Union (AGU) Fall Meeting. Estimating geocenter motion and changes in Earth's dynamic oblateness. December 14-18, 2015 San Francisco, America.*

4. *GRACE Science Team meeting (GSTM). J_2 variation estimation from GRACE, OBP and GIA. September 29 - October 1, 2014 Potsdam, Germany.*

5. *International Association of Geodesy (IAG). An evaluation of geocenter motion estimates from GRACE products. September 1-6, 2013, Potsdam, Germany.*

About the Author

Yu Sun was born in Dezhou, Shandong, China, on 22 September 1986. He obtained a Bachelor of Engineering from Shandong University of Science and Technology with a degree in Surveying and Mapping Engineering in 2009. After completing his undergraduate degree, he accepted a joint master degree program between Shandong University of Science and Technology and the Satellite Applications Center for Surveying and Mapping. During his graduate studies, he determined and analysed Lunar gravity field using data from Lunar Prospector. He earned his master degree in 2012. After that, he applied a four-year scholarship from the Chinese Scholarship Council (CSC) and became a PhD candidate in Delft University of Technology, the Netherlands. He worked with Riccardo Riva and Pavel Ditmar on geocenter motion determination in the physical and space geodesy ground (PSG) leading by Prof. Roland Klees. Since September 2016, he accepted the job as a research scientist in the same group.